DOUBLE Ph.D. DEGREE

DOTTORE DI RICERCA IN FISICA (University of Cagliari)
and
DOCTOR OF PHILOSOPHY (University of Groningen)

Cycle XXXV

TITLE OF THE Ph.D. THESIS

Photophysics and optoelectronics of metal halide perovskites and other unconventional semiconductors

Scientific Disciplinary Sector(s)

FIS/03

Ph.D. Student:	Riccardo Pau
Supervisor (UniCa)	Prof. Michele Saba
Supervisor (UG)	Prof. Maria A. Loi

Final exam. Academic Year 2021/2022
Thesis defence session: May 2024

La borsa di dottorato è stata cofinanziata con risorse del
Programma Operativo Nazionale Ricerca e Innovazione 2014-2020 (CCI 2014IT16M2OP005),
Fondo Sociale Europeo, Azione I.1 “Dottorati Innovativi con caratterizzazione Industriale”

UNIONE EUROPEA
Fondo Sociale Europeo

Table of Contents

Chapter 1

Introduction

1.1 Solar cells

A solar cell is a device in which the light absorbed is directly converted into electrical energy by the photovoltaic effect. Most traditionally solar cells are p-n junction devices, that consists of semiconductor crystal with a p-type doped and a n-type doped region. The formation of the depletion region between these two doped regions is key in the functioning of semiconductor devices such as LEDs and solar cells. The solar cell functions as a forward-biased p–n junction, with current flowing in a direction opposite to a normal forward-biased p–n diode. Light that enters the p–n junction and reaches the depletion region of the solar cell generates electron–hole pairs. The generated minority carriers will drift across the depletion region and enter the n- and p-regions as majority carriers, being extracted in the external circuit by an anode and a cathode electrode at the p- and n- side, respectively.

More recently this classical structure has been generalized, and nowadays often we speak of p-i-n structures, namely structures where the functions of the original p-n junction are separated, and even different materials are used.
As of these days, the photovoltaic market is still predominantly occupied (>90%) by silicon (Si)-based solar cells. However, this technology suffers from limitations due to the low absorption coefficient, which stems from the indirect bandgap (bringing to devices of large thickness), and the extreme requirements in purity and temperature needed to process the Si modules. Also for this reason, since the early 90s, new materials have been explored in the scientific research community, with the aim of reaching power conversion efficiencies closer to the theoretical limit calculated by Shockley and Queisser in 1961 of 33.7% for a semiconductor with an energy bandgap of around 1.34 eV[1].

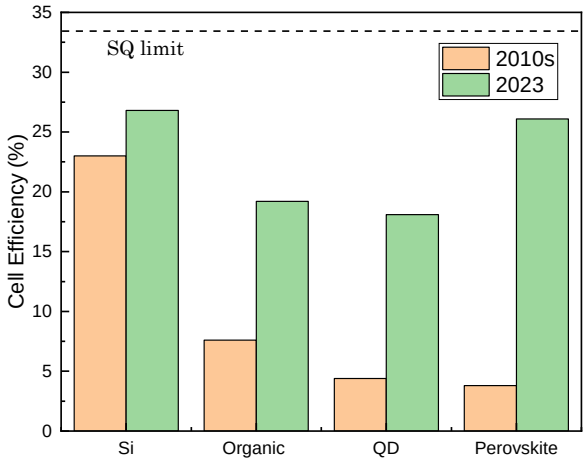

Figure 1.1 Best research-cell efficiencies for Si-based photovoltaics and emerging PV technologies (organic, quantum-dot and perovskite) comparing 2010s vs 2023. The Shockley-Queisser limit for single-junction solar cells is denoted by the black dashed line. Data source: NREL research efficiency chart[2].

In this framework, metal halide perovskites have seen their efficiency skyrocketing to values that can compete with the laboratory-scale efficiencies of single crystalline Si and are superior to copper indium gallium selenide (CIGS) and cadmium telluride (CdTe) devices. However, these materials struggle to look out to the well-established market, as critical obstacles like long-term durability, scalability, toxicity still need to be addressed. Other than that, Si-based PV has seen its cost progressively decrease due to large-scale manufacturing and strong demand, making the necessity of developing another technology not obvious. In this contest it is seen as one of the best strategy the integration of metal halide perovskite devices on Si devices in the tandem configuration[3,4].

After more than ten years of intense research on the physical properties and device optimization of metal halide perovskites, the large progresses made are a motivation to further increase the efforts in this direction. Chemical optimization, a deep understanding of the photophysics underlying these materials and device engineering are the main strategies that we have towards the establishment of solar technology based completely, or partially on metal halide perovskites.

1.2 Solution processable semiconductors

The materials studied in this thesis, namely hybrid metal halide perovskites and organic semiconductors, can be classified as emerging semiconductors processable from solution. These materials are dissolved in appropriate solvents, the resulting solution or dispersion (depending on the cases) can be then deposited into substrates to realize thin films with variable thicknesses of the order of hundreds of nanometers. Among the many different deposition techniques, the main one adopted in the works described in this thesis is spin coating. When depositing metal halide perovskites several modifications have been made to the simple single step deposition, with the aim of controlling the nucleation and the crystallization of the material at the aim of obtaining the polycrystalline closed films that are necessary for the fabrication of solar cells. The most common of this modifications are the anti-solvent dropping, the multiple steps deposition, the hot-casting, etc..

In a standard spin coating deposition, the precursor solution is dropped into a rotating substrate from a microsyringe and the substrate is then accelerated to the desired speed. The solution is spread through the whole substrate due to centrifugal forces, while the excess one is quickly expelled from the surface. Ultimately, the layer reaches its desired speed, and the further shrinkage is due to solvent loss, in the meantime the nucleation of the material and its crystallization in a coated thin film has started. With an additional anti-solvent treatment, to increase the number of nuclei for crystallization and in a certain sense to accelerate the crystallization and improve the compactness of the film[5,6]. The final thickness achieved ranges between few hundreds of nanometers to micrometers and mainly depends on the solution concentrations, the spinning speed, and on the solvents used. After the process, typically films are thermal annealed to remove any residual solvent and to complete the crystallization of the material.

As a mature technique with an easy control on the experimental parameters, spin-coating presents also some criticalities, such as the size limitations on the substrates and the lack of material efficiency. It is estimated that more than 90% of the dispensed material is flung off in the deposition bowl and therefore disposed. This limits in scalability and in manufacturing costs (materials and disposal) give not hope for the technique to be used in the manufacturing process of solar panels.

Additional experimental details about materials used, deposition parameters and characterization are addressed in the experimental section of the specific chapters.

1.3 Metal halide perovskites

Perovskites trace their roots to the oxide calcium titanate ($CaTiO_3$), a mineral discovered in 1839 by the mineralogist Gustav Rose, who named it after the Russian Count Lev A. Perovskiy (1792-1856).
Later, many inorganic metal oxides were found to have the perovskite structure, and after that, the term perovskite became the definition of a whole class of materials crystallizing in the same structure[7,8].
The conventional perovskite structure was defined in 1926 by Goldschmidt and it is described by the general chemical formula ABX_3, where A and B are cations and X is an anion. In the cubic unit cell of these compounds, the A cations occupy the corners of the cube, while the B cation is located at the body-centered position and the X anions are distributed in the face-centered positions, as depicted in Fig.1.2. The ideal cubic structure therefore has the A-site cations surrounded by 12 anions in twelve-fold cuboctahedral coordination, while the B cations are surrounded by an octahedron of anions[9].

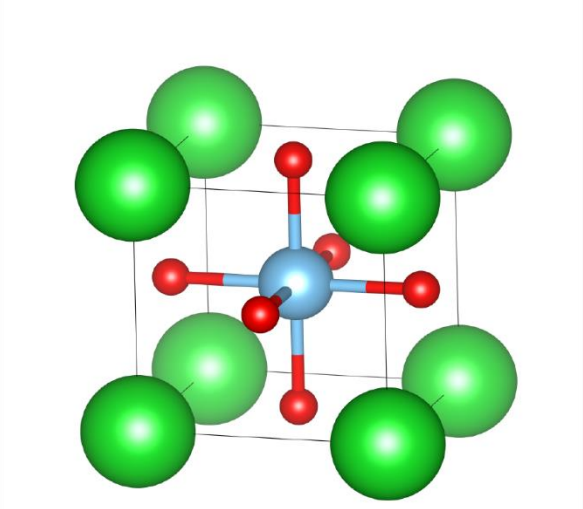

Figure 1.2 Perovskite cubic structure. Larger A cations (green) form a simple cubic structure, where the center of each face is occupied by the X anion (red), that are six-fold coordinated to the smaller cation B, located at the center of the cube.

The structural stability of perovskites as described by Goldschmidt is determined by two empirical parameters, namely the tolerance factor (t) and the octahedral factor (μ). The tolerance factor *t* is defined by the following equation[10]

$$t = \frac{r_a + r_x}{\sqrt{2}(r_b + r_x)} \qquad (1)$$

where r_a, r_b and r_x are respectively the ionic radii of A, B and X site ions, while the octahedral factor is defined by the ratio r_b/r_x, assessing whether the B cation can fit in the octahedron of anions. The condition of an ideal cubic perovskite structure corresponds to $t = 1$, but in many cases, there are slight structural distortions due to ionic displacement, that can influence the physical properties of the material. Empirically, for stable 3D perovskite structures, the *t* value ranges between 0.8 and 1.0 and the octahedral factor between 0.44 and 0.90. For values of tolerance factor in the range $0.80 < t < 0.9$, distorted structures are observed. Interestingly, these two parameters provide a quick 0^{th} order prediction of the stability of a certain ions combination in a perovskite structure, however, some adjustments have been made for example by Bartel et al. in 2019 to improve the accuracy of the tolerance factor (8% incorrect)[11].

Before the last decade, the most appealing class of perovskites for the scientific community was the oxides one, described by the ABO_3 formula. These fully inorganic perovskites, such as $SrTiO_3$, $BaTiO_3$, $PbTiO_3$, $CaTiO_3$, $CdTiO_3$, etc., show interesting physical properties, and a wide range of chemical tunability. Perovskite oxides have been used as catalysts, superconductors, insulators, piezoelectrics and ferroelectric materials[12–14]. However, most of these materials show poor semiconducting properties.

Unlike oxides perovskites, the metal halide perovskites (MHPs) subclass, has become recently one of the most promising semiconductors for photovoltaics and other optoelectronic applications, due to their excellent optoelectronic properties, such as the high optical absorption coefficients and their good transport properties.

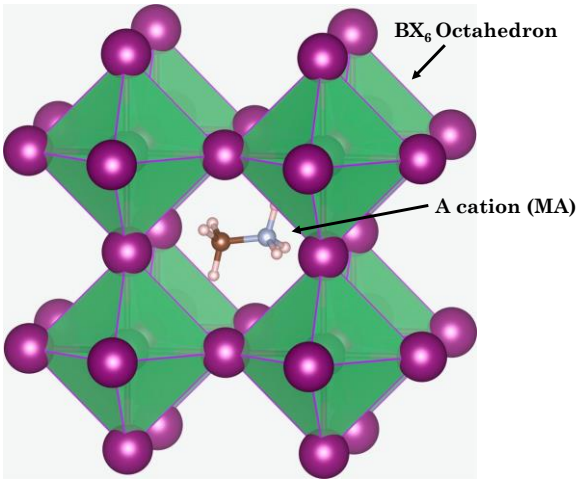

Figure 1.3 Metal halide perovskite crystal structure of $CH_3NH_3BX_3$ in its cubic phase, showing the typical CH_3NH_3 (methylammonium, MA) organic cation in the A-site, located between the voids of the inorganic octahedra BX_6. Figure adapted from ref.[15]

In their structure, A is a monovalent cation such as methylammonium (MA^+), formamidinium (FA^+) or cesium (Cs^+), B is a bivalent metal cation (Pb^{+2}, Sn^{2+}), while the X sites are occupied by a halide monovalent anion (Cl^-, Br^- or I^-). One of the main features of metal halide perovskites is the possibility to tune their bandgap by modification of the chemical composition, by variations of the halide's ratio. In the case of the extensively studied methylammonium lead tri-halide perovskite, by swapping the I atoms from the Br one, the energy gap can be modified from 1.55 eV, to 2.23 eV, respectively, and can even be broadened till 3.11 eV utilizing Cl. A more fine tailoring can be done by mixing halides to obtain intermediate stoichiometries[16].
Smaller changes in the bandgap can also be achieved by cationic substitution and mixing. In the case of $MAPbI_3$, the bandgap increases from 1.55 to 1.73 eV by replacing the MA cation with the smaller Cs and decreases to 1.48 eV with the larger FA. As for the metallic cations, the bandgap of pure $MASnI_3$ narrows down to a value of 1.35 eV, but when looking at the Sn/Pb mixtures, the complexity of the system brings non-linear variations of the bandgap[17,18].

Another way to tune energy gap in perovskites is to reduce their dimensionality by introducing a bulkier cation (mostly organic) at the A-site and therefore disrupting the 3D network.

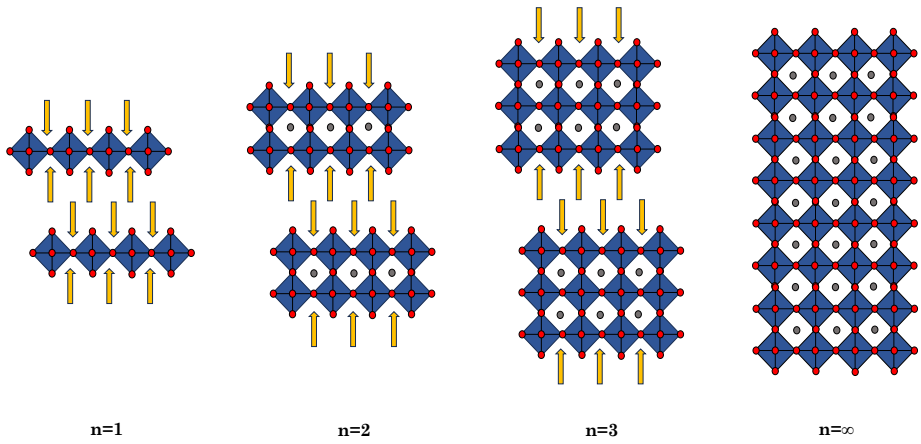

Figure 1.4 Schematic representation of the lower-dimensional perovskite structures. From left to right, Ruddlesden-Popper 2D phase for n=1, Quasi 2D phases n=2 and n=3 and 3D perovskite structure (n=∞).

Lower-dimensional perovskites can be obtained starting from the 3D structure by making slices along different crystallographic directions, resulting in a gradual lift of the size restrictions outlined by the tolerance factor (t > 1). Even if the size constraint is relaxed, the choice of the organic cation and the stoichiometry are very impactful parameters to design and synthesize a desired layered, low-dimensional perovskite structure[19]. Because of this extended chemical tunability and their interesting optical properties, two-dimensional halide perovskites and mixed 2D/3D structures are becoming more and more investigated also in optoelectronic devices. Among the different types of low dimensional perovskites systems, 2D Ruddlesden-Popper materials are extremely popular thanks to their growing performances and enhanced stability in the solar cells. This layered structure is described by the formula $A'_2A_{n-1}B_nX_{3n+1}$, where A' is the large spacer cation and n is the number of layers of the octahedral included. For n = 1, we have a 2D Ruddlesden-Popper phase, in which only one layer of inorganic octahedra is included between the organic layers, while, on the other limit situation, for n = ∞, we have the 3D perovskite structure in which one of more cations correctly fit in the A site.

Another important feature of metal halide perovskites is their defect-tolerance, despite their simple solution processability. Defects can be classified in point defects, such as atomic vacancies, interstitials, anti-site substitutions and in line/planar defects such as dislocations and

grain boundaries. The formation of defects significantly depends on fabrication conditions, like precursors concentration, annealing temperature and choice of solvents[20,21].
Given a spatially localized defect state in the semiconductor, this can act as trapping site for an approaching electron or hole. The trapped charge carrier can be emitted or "de-trapped" thermically if the trap energy is sufficiently small (shallow trap). However, if the activation energy is large, it is likely that the charge carrier will recombine through non-radiative processes with the emission of phonons, therefore leading to undesired loss mechanisms in the device. Despite the multiple advantages of metal halide perovskites, these materials are characterized by low defect formation energies that suggest large concentration of defects. However, in MHPs, the formation of shallow defect states is favored, making them contemplated as defect-tolerant materials. The possibility to fabricate by solution such materials, makes metal halide perovskite a uniqueness in the semiconductors field. [22,23]. However, it is important to realize that defects can deeply influence degradation processes of perovskites.

1.4 Characterization techniques

The section below is aimed at giving a brief description of the main experimental techniques that have been applied to the materials studied in this thesis. A more specific discussion on the experimental setups used can be found in the Methods section of the respective chapter.

1.4.1 Absorption spectroscopy

When a beam of light interacts with a material, photons can be either reflected, absorbed or transmitted. A portion of the light can be reflected from the surface of the material, while the rest can propagate through the medium. During propagation, if the light has a resonant frequency with the atoms of the material, absorption can occur with a consequent attenuation of the beam. The fraction of the light that passes through the medium is called transmittance. This mechanism is formally expressed by the Lambert-Beer law, in which the intensity

of the light incident beam at a certain propagation distance z is given by[24]:

$$I(z) = I_0 e^{-\alpha z} \qquad (2)$$

where I_0 is the initial light beam intensity and α is the absorption coefficient, that is a function of frequency of the light.
The absorption of a material can be also expressed in terms of optical density (O.D.) or absorbance:

$$O.D. = -\log_{10} \frac{I(l)}{I_o} \qquad (3)$$

In a typical absorption measurement, monochromatic light is generated by passing a white-light source into a monochromator. The sample, a thin film or a solution is then scanned by light of several wavelengths in a range that is usually between 300 and 1200 nm. The resulting absorbance is plotted as a function of the wavelength and several information can be extracted such as the absorption coefficient and the energy gap of the material.

1.4.2 Photoluminescence spectroscopy

Photoluminescence is a particular case of light emission that occurs when a semiconductor is irradiated by photons of energy *hv* higher than its energy bandgap. Upon absorption of the light, electrons are excited from the valence band to the conduction band, and then quickly relax to the bottom of the band, dissipating the excess energy by emitting phonons. For most semiconductors, these relaxation processes take place on time scales of the order of 100 femtoseconds. The same mechanism happens for an equal number of holes in the valence band, as the absorption of a photon creates an electron-hole pair in the material. Recombination can take place radiatively, when electrons and holes recombine through the emission of a photon, or non-radiatively, when energy is dissipated by phonon emission or transferred to defect states inside the energy gap.

In an excited state, the recombination rate goes through the competing radiative and non-radiative processes, therefore the rate equation for its population is given by:

$$\frac{dn(t)}{dt} = -\frac{n(t)}{\tau} = -n(t)\left(\frac{1}{\tau_R} + \frac{1}{\tau_{NR}}\right) \tag{4}$$

Where τ_R and τ_{NR} are the radiative and non-radiative lifetimes, respectively. The photoluminescence intensity is directly proportional to the population of the excited state:

$$I_{pl} \propto n(t) = n_0 e^{-\frac{t}{\tau}} \tag{5}$$

Experimentally, this translates in the possibility of using the PL intensity decay curves to determine the average lifetime of an excited state.
The parameter that quantifies the radiative efficiency of the material is called luminescence quantum yield (QY) and it is defined as the ratio between the radiative recombination rate and the total recombination rate[25]:

$$QY = \frac{1/\tau_R}{\left(\frac{1}{\tau_R} + \frac{1}{\tau_{NR}}\right)} = \frac{1}{1 + \frac{\tau_R}{\tau_{NR}}} \leq 1 \tag{6}$$

For $\tau_R \ll \tau_{NR}$, radiative recombination is much more likely to happen, thus QY value approaches the unit. On the other hand, very short τ_{NR} are typical of high defect density materials and their QY is very low.
It is important to point out that the radiative lifetime τ_R is not the same as the measured luminescence decay time τ. The latter can be the result of multiple decay processes contributions, so that the values of radiative and non-radiative lifetime cannot be determined independently from a single measured PL decay.

In the case of metal halide perovskites, the recombination dynamics can be described by the following rate equation, which accounts for all the recombination processes involved:

$$\frac{dn(t)}{dt} = -k_1 n - k_2 n^2 - k_3 n^3 \qquad (7)$$

where n is the charge-carrier density. Eq. 7 accounts for all the main recombination processes involved in MHPs. The rate constant k_1 is associated with monomolecular recombination, thus due to trap-assisted recombination involving the capture of an individual carrier (an electron or a hole). The bimolecular charge-carrier recombination constant k_2 is related to intrinsic electron-hole recombination and depends on both electron and hole densities (n_e and n_h respectively), and therefore on $n_e n_h = n^2$ for photoexcitation. The last term corresponds to Auger recombination, a process occurring when electron and hole recombine, accompanied by energy and momentum transfer to a third participant. This process can potentially involve phonon absorption or emission and is described by the constant k_3.
These three mechanism contribute to the total recombination rate *r(n,t)* that affects the charge-carrier diffusion length L_D following the equation:

$$L_D = \sqrt{\frac{\mu k_B T}{r(n) e}} \qquad (8)$$

where $r(n) = k_3 n^2 + k_2 n + k_1$, μ is the charge-carrier mobility, T is the temperature, k_B is the Boltzmann constant and e is the electron charge.[26,27]

In a typical PL spectroscopy setup, a sample is excited with a monochromatic excitation source, for instance a laser beam, with photons having energy higher than the bandgap of the sample. The resulting PL signal from the sample is then collected through an optical system and dispersed in a spectrometer, coupled to a detector.
Using ultrashort laser pulses, in the order of 100 fs), the excitation is impulsive, and it is possible to perform measurements of the PL temporal evolution to get direct information about the radiative recombination processes, rates and lifetimes. The time dependence of the photoluminescence can be measured with time ranges of some nanoseconds and temporal resolutions of picoseconds by using for example a streak camera. With such experimental apparatus, it's possible to extract PL spectra at specific delay times and PL decays at a selected wavelength range.

1.4.3 Pump-probe spectroscopy

Pump-probe is a powerful optical technique to characterize the excited state in a semiconductor material, giving information about the photophysical dynamics in time scales on the order of picoseconds, with the resolution ultimately equal to the width of the laser pulse.
In a typical pump-probe experiment, the pump pulse excites the material, while the transmission change of the system is monitored by a delayed probe pulse, in the assumption that between two pump pulses the system is fully recovered to its initial state.

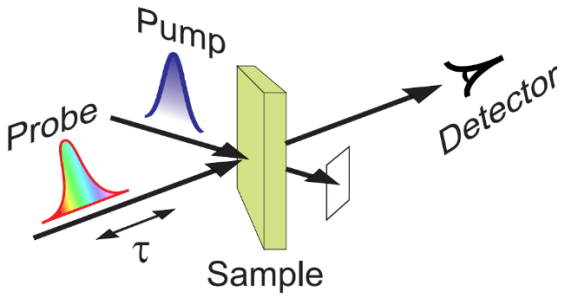

Figure 1.5 Schematical representation of a pump-probe experiment[28]

Pump and probe signals are often obtained from the same laser source after multiple non-linear optical operations, such as supercontinuum generation, harmonic generation and parametric amplification. The two pulses are shifted in time, by using a delay line. The experimental signal is the variation of transmission ΔT, normalized to the ground state transmission, as a function of the pump-probe delay and of the wavelength. The two signals are focused on the same spot in the sample, with the precaution of using a larger pump spot then the probe spot, to guarantee overlap and investigate the right excited region of the sample. Additionally, the probe should be a negligible perturbation of the system and therefore a smaller intensity with respect to the pump[29].
In a pump-probe measurements, three main spectral features can be distinguished, depending on the differential transmission ΔT/T signal (Fig 1.6).

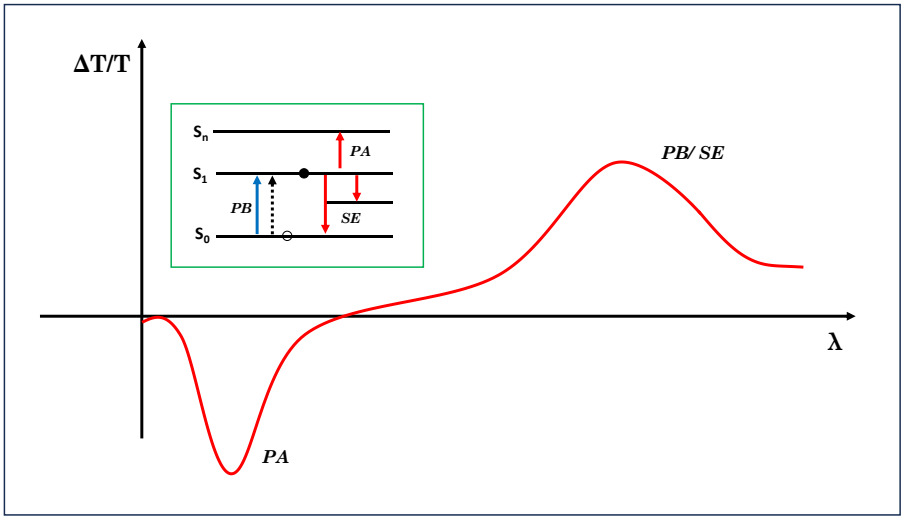

Figure 1.6 Pump-probe spectrum representing ΔT/T as a function of the wavelength. The spectral features are indicated as photoinduced absorption (PA) and photobleaching/stimulated emission (PB/SE). In the green rectangle inset an illustration of the three mechanism. Solid and open circles represent occupied and empty states, respectively. The dashed line arrow represents a weaker intensity transition, caused by population depletion. Inset adapted from Ref.[29]

In the first case, called photobleaching (PB), the pump pulse populates the excited state of the material, with a consequent diminishing of the number of electrons in valence band (ground-state depletion). This mechanism induces an absorption decrease (enhanced transparency), at probe frequencies, and therefore corresponds to positive ΔT/T.
In the two other cases, the probe pulse can stimulate both upward and downward transitions. In the second case, called stimulate emission (SE), with the pump pulse populating the excited state, the probe can stimulate the downward transition with consequent photon emission, leading to an increase in differential transmission. The third case is called photoinduced absorption (PA) and it is caused by the probe stimulating the upward transition to the higher excited state, causing a $\Delta T/T<0$.

1.4.4 Solar cells characterization

The worldwide standard to characterize a solar cell is under AM1.5G solar spectrum with power density of P_{in} = 100 mW/cm^2. A typical current density-voltage characteristics (J-V characteristics) of a solar cell under illumination is presented in Fig. 1.7.

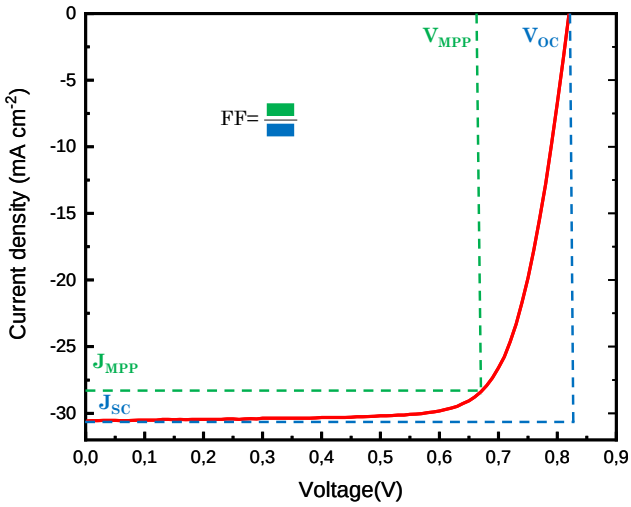

Figure 1.7 A typical J-V curve (red) of a solar cell measured under illumination, showing the parameters of interest and a representation of the fill factor as a ratio of the dashed green delimited area to the dashed blue delimited area.

The values of the photo-generated current and of the voltage at short-circuit (V=0) and open-circuit (J=0) conditions are named, respectively, short-circuit current density (J_{sc}) and open-circuit voltage (V_{oc}). In these two configurations, the electric power that can be obtained from the device is equal to zero.
The maximum power point (MPP) corresponds to the maximum power that can be extracted from the solar cell and it is defined as the product $J_{MPP} \cdot V_{MPP}$. An important PV parameter is the fill factor (FF) which is defined as the ratio between the maximum power P_{MP} and the electrical output of V_{oc} and J_{sc}:

$$FF = \frac{P_{MPP}}{J_{sc}V_{OC}} = \frac{J_{MPP}V_{MPP}}{J_{sc}V_{OC}} \qquad (9)$$

The power conversion efficiency (PCE) of a solar cell is defined by the maximum power generated by the solar cell divided by the incident power light:

$$PCE = \frac{J_{MPP}V_{MPP}}{P_{in}} = \frac{FFJ_{sc}V_{OC}}{P_{in}} \qquad (10)$$

As defined in Eq. 10, the PCE is defined in terms of experimental parameters, namely V_{oc}, J_{sc} and FF, measured under standard conditions, that must be optimized simultaneously in order to achieve the highest efficiencies.

Another important parameter to characterize a solar cell is the ratio between the number of collected photogenerated electrons and the number of incident photons, at a given wavelength λ. This quantity is called external quantum efficiency (EQE) and can be experimentally calculated by using the following:

$$EQE\ (\lambda) = \frac{N_e\ (\lambda)}{N_{ph}(\lambda)} = \frac{hc}{q\lambda}\frac{J(\lambda)}{P_{in}(\lambda)} \qquad (11)$$

where h is Planck's constant, c is the speed of light, q the electron charge and P_{in} is the incident light intensity at λ[30].
By integrating Eq. 11 over the wavelength, it is possible to calculate the short-circuit current density of the device:

$$J_{calc} = \int \frac{q\lambda}{hc} EQE(\lambda)P_{in}(\lambda)d\lambda \qquad (12)$$

1.5 Thesis outline

Understanding the nature and the dynamics of the photoexcitation in metal halide perovskite is of paramount importance to further develop high performing devices based on them. In **Chapter 2**, by utilizing a tandem setup that combines time-resolved photoluminescence spectroscopy and ultrafast pump-probe spectroscopy, both prototypical 3D and 2D halide perovskites have been studied. A rational comparison of photoluminescence and differential transmission signals has been possible due to the use of the very same train of laser pulses to produce them, creating the same excitation density in the same sample spot. Our results indicate the formation of a plasma of charged carriers, coupled to lattice deformation to form large polarons, in chemical quasi-equilibrum with a minority phase of excitons.
In **Chapter 3**, by setting up a radiometric time-resolved PL experiment, the radiative recombination rates in 3D hybrid perovskites thin films have been calculated. The measured radiative decay is found to be significantly lower than the ones estimated under the assumption of the only presence of excitons and free carriers, suggesting the existence of large polarons as the majority population.

In **Chapter 4**, a wide-ranging optical characterization has been performed to understand the photophysics underlying a novel photocatalytic doping mechanism in organic semiconductors. A combination of absorption spectroscopy, time-resolved photoluminescence and pump-probe spectroscopy has been applied to this system unveiling how the photocatalyst is the main participant in the electron transfer process. In-situ measurements on the photocatalyst Mes-Acr-Me showed from an optical point of view the catalytic cycle and the possibility of full regeneration upon air exposure. Furthermore, a Stern-Volmer analysis has been conducted on the organic semiconductor PBTTT and photocatalyst Mes-Acr-Ph, allowing the calculation of the photoluminescence quencher constants.

In **Chapter 5**, we introduce for the first time copper iodide (CuI) l as hole transport layer (HTL) in a $EACl_{0.015}Cs_{0.25}FA_{0.75}Sn_{0.5}Pb_{0.5}I_3$ perovskite solar cell. The results obtained have been compared with devices realized with the most used HTL in literature, PEDOT:PSS. The characterization techniques used space from the microscopy imaging of the CuI film by atomic force microscopy and scanning electron microscopy, to structural characterization techniques such as

X-ray diffraction (XRD), to assess the quality of the material, to the photovoltaic characterization of the device.
The power conversion efficiency obtained for the best device based on CuI was 20.1%, with a remarkable improvement with respect to the 19.03% obtained by using PEDOT:PSS. The device stability was studied in N_2 shelf-lifetime, showing that the CuI device retained 92.8% of its initial efficiency after 155 days, and under thermal stress at 85°C. The results obtained represent a promising starting point for high efficiency Sn-based perovskite solar cell without the use of PEDOT:PSS.

1.6 References

[1] P. Wang, Y. Wu, B. Cai, Q. Ma, X. Zheng, W. H. Zhang, *Adv. Funct. Mater.* **2019**, *29*, 1807661.

[2] National Renewable Energy Laboratories (NREL), "Best Research-Cell Efficiency Chart", can be found under https://www.nrel.gov/pv/cell-efficiency.html, **2023**.

[3] H. Shen, D. Walter, Y. Wu, K. C. Fong, D. A. Jacobs, T. Duong, J. Peng, K. Weber, T. P. White, K. R. Catchpole, *Adv. Energy Mater.* **2020**, *10*, 1902840.

[4] M. H. Futscher, B. Ehrler, *ACS Energy Lett.* **2016**, *1*, 863-868.

[5] N. Sahu, B. Parija, S. Panigrahi, *Indian J. Phys.* **2009**, *83*, 493-502.

[6] Z. Liu, M. Chen, L. Wan, Y. Liu, Y. Wang, Y. Gan, Z. Guo, D. Eder, S. Wang, *SN Appl. Sci.* **2019**, *1*, 706.

[7] A. K. Jena, A. Kulkarni, T. Miyasaka, *Chem. Rev.* **2019**, *119*, 3036-3103.

[8] Q. A. Akkerman, L. Manna, *ACS Energy Lett.* **2020**, 604-610.

[9] R. H. Mitchell, M. D. Welch, A. R. Chakhmouradian, *Mineral. Mag.* **2017**, *81*, 411.

[10] V. M. Goldschmidt, *Naturwissenschaften* **1926**, *14*, 477.

[11] M. Pitaro, E. K. Tekelenburg, S. Shao, M. A. Loi, *Adv. Mater.* **2022**, *34*, 2105844.

[12] H. D. Megaw, *Proc. Phys. Soc.* **1946**, *58*, 133.

[13] Z. J. L. Bare, R. J. Morelock, C. B. Musgrave, *Sci. Data* **2023**, *10*, 244.

[14] D. B. Mitzi, in *Prog. Lipid Res.*, **1999**, pp. 1–121.

[15] C. Eames, J. M. Frost, P. R. F. Barnes, B. C. O'Regan, A.

Walsh, M. S. Islam, *Nat. Commun.* **2015**, *6*, 7497.

[16] N. Kitazawa, Y. Watanabe, Y. Nakamura, *J. Mater. Sci.* **2002**, *37*, 3585.

[17] S. Adjokatse, H. H. Fang, M. A. Loi, *Mater. Today* **2017**, *20*, 413-424.

[18] J. Xi, M. A. Loi, *ACS Energy Lett.* **2021**, *6*, 1803-1810.

[19] B. Saparov, D. B. Mitzi, *Chem. Rev.* **2016**, *116*, 4558.

[20] J. M. Ball, A. Petrozza, *Nat. Energy* **2016**, *1*, 16149.

[21] S. Bera, A. Saha, S. Mondal, A. Biswas, S. Mallick, R. Chatterjee, S. Roy, *Mater. Adv.* **2022**, *3*, 5234.

[22] A. Walsh, D. O. Scanlon, S. Chen, X. G. Gong, S. H. Wei, *Angew. Chemie - Int. Ed.* **2015**, *54*, 1791.

[23] H. Jin, E. Debroye, M. Keshavarz, I. G. Scheblykin, M. B. J. Roeffaers, J. Hofkens, J. A. Steele, *Mater. Horizons* **2020**, *7*, 397.

[24] M. Fox, *Optical Properties of Solids*, Oxford University Press, **2010**.

[25] I. Pelant, J. Valenta, *Luminescence Spectroscopy of Semiconductors,* Oxford University Press, **2012**.

[26] L. M. Herz, *Annu. Rev. Phys. Chem.* **2016**, *67*, 65-89.

[27] M. Saba, M. Cadelano, D. Marongiu, F. Chen, V. Sarritzu, N. Sestu, C. Figus, M. Aresti, R. Piras, A. Geddo Lehmann, C. Cannas, A. Musinu, F. Quochi, A. Mura, G. Bongiovanni, *Nat. Commun.* **2014**, *5*, 5049.

[28] G. Cerullo, C. Manzoni, L. Lüer, D. Polli, *Photochem. Photobiol. Sci.* **2007**, *6*, 135.

[29] G. Lanzani, *The Photophysics behind Photovoltaics and Photonics*, Wiley-VCH, **2012**.

[30] T. Dittrich, *Mater. Concepts Sol. Cells* **2018**, 3-43.

Chapter 2

Polaron plasma in equilibrium with bright excitons in 2D and 3D hybrid perovskites

A major reason for the success of perovskite photovoltaics is the presence of free carriers as majority optical excitations at room temperature. Instead in 2D perovskites the current understanding is that bound excitons form, which need to be split in solar cells and are not beneficial to photoconversion. In this chapter we apply a tandem spectroscopy technique that combines ultrafast photoluminescence and differential transmission to demonstrate the presence of a plasma of unbound charge carriers in chemical equilibrium with a minority phase of light-emitting excitons, even in 2D perovskites and at cryogenic temperatures. The underlying photophysics is interpreted as formation of large polarons, charge carriers coupled to lattice deformations, in place of excitons. A conductive polaron plasma foresees novel mechanisms for LEDs and lasers, as well as a prominent role for 2D perovskites in photovoltaics.

This chapter is based on the publication:
*A. Simbula, **R. Pau**, Q. Wang, F. Liu, V. Sarritzu, S. Lai, M. Lodde, F. Mattana, G. Mula, A. Geddo Lehmann, I.D. Spanopoulos, M.G. Kanatzidis, D. Marongiu, F. Quochi, M. Saba, A. Mura, and G. Bongiovanni, Advanced Optical Materials, **2021**, 9, 2100295*

Contribution to the experimental work: samples preparation, ultrafast tandem spectroscopy measurements: time-resolved photoluminescence, transient absorption spectroscopy and data analysis.

2.1 Introduction

Thanks to hybrid metal-halide perovskites (HPs), solution-process materials may now be employed in efficient single-junction and tandem solar cells. Photoconversion performances in these materials have been linked to unique photophysics properties.[1–7] First it was realized that, in spite of an absorption spectrum featuring a marked excitonic resonance, the majority optical excitation in prototypical HP materials for photovoltaics are not bound excitons, but unbound charge carriers. Therefore, electrons and holes excited by solar light can be directed to the electrodes at a negligible energy cost, without the need to split tightly bound excitons as in organics. Taking advantage of the flexibility of the materials class, layered 2D <1,0,0> HPs are obtained by inserting bulky organic cations into the formulation, leading to materials inherently more stable than their 3D counterparts against some forms of degradation.[8–10] However, in 2D HPs the exciton binding energy can be as large as 400 meV,[8] so that it is commonly assumed that their excited states are mostly excitons.

A second peculiar characteristic of the excited states in perovskites is the formation of large polarons, i.e., charge carriers coupled to lattice deformations and delocalized over many crystal lattice sites.[11–20] Unlike small polarons in organics, localized in a single molecule, large polarons are compatible with band transport, but are also able to screen the excited states from scattering with defects and reduce non-radiative recombination through trap states, resulting in large mobilities and long lifetimes. Large polarons are also believed to reduce scattering with phonons and have been proposed as an explanation for hot carriers persisting for several nanoseconds at temperatures significantly higher than the lattice one.[12,16,17,21–26] Large polarons may therefore be the enabling microscopic mechanism for efficient solar cells, including innovative architectures that exploit photoconversion with hot carriers.[27,28]

Theoretical estimations forecast that the energy associated with polaron formation is comparable with the binding energy gained by forming an exciton, maybe even larger in some materials.[12,14,24,29–32] When do polarons form and whether excitons or polarons are the lowest-energy optical excitations is still an open question. The issue is particularly relevant for layered 2D HPs, where polaronic effects have been demonstrated, although it is not clear if small or large polarons are formed.[33–37] In spite of the large exciton binding energy, unbound

charge carriers have been reported, so that it is not clear yet how much energy needs to be spent in solar cells to split bound excitons.[38–44]
Here we present ultrafast tandem spectroscopy experiments to investigate the roles of excitons, free charged carriers and polarons in HPs. The body of experimental results is consistent with a picture in which a majority of charged carriers, polarons, coexists with a minority of bound excitons in both 3D and 2D HPs, even when the exciton binding energy by far exceeds thermal energy.

2.2 Results

2.2.1 Ultrafast tandem spectroscopy

The optical properties of hybrid perovskites are typically studied with two ultrafast spectroscopy techniques, namely time-resolved photoluminescence (PL) and differential transmission (DT), also known as transient absorption or pump-probe. The two techniques probe different properties and are complementary to each other. PL is only sensitive to radiative species, as it collects the light emitted from the sample under pulsed laser excitation. On the other hand, DT is sensitive to all optical excitations, even if they cannot emit light ('dark states'), since a DT signal may arise from phase space filling in only one of the two bands involved (conduction or valence), but also from collisional broadening and other nonlinear interactions that do not require the same states to be occupied (see Figure A.1). Therefore, a DT signal can be produced even by excitations that are completely dark in photoluminescence. Furthermore, the DT signal is directly proportional to the excited-state population density, while the PL signal follows a power law with an exponent equal to the order of the recombination process leading to the emission: it is directly proportional to population density for monomolecular recombination, while proportional to the square of the population for bimolecular recombination. The synergy between the two techniques should therefore yield information on the nature of majority photoexcitations and whether or not they emit light. A previous study [45] has linked the two measurements on $MAPbI_3$ films employed for solar cells. A crucial experimental hurdle for quantitative comparison of PL and DT is that the time decays are inherently non-linear in the excitation density, i.e., they change with laser fluence. Furthermore, different spots on a thin film surface may produce different decay times. DT and PL setups may

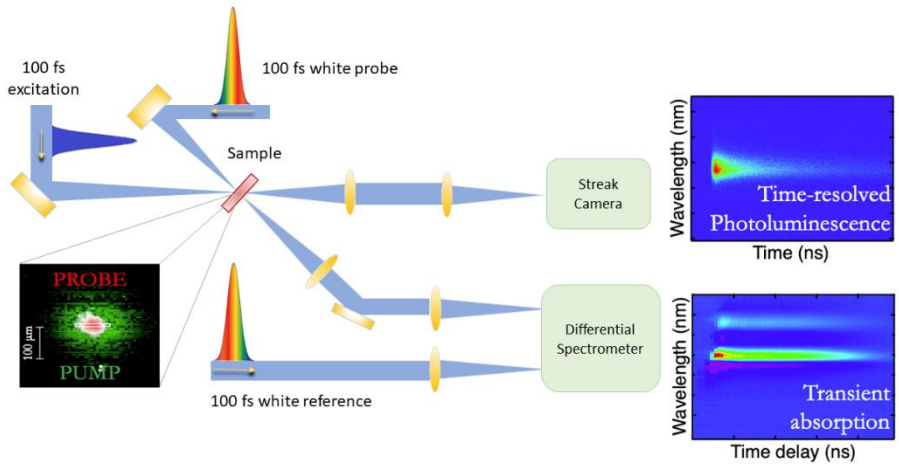

Figure 2.1 Ultrafast tandem spectroscopy setup. The sketch illustrates how a femtosecond pump laser is focused onto samples and then time-resolved PL is detected with a picosecond streak camera, while a second broadband femtosecond pulse acts as a probe for DT. The crucial feature of the setup is that the same pump pulses cause the two effects, which therefore occur by construction at the same excitation density and spot on the sample. In the lower left corner are shown the superimposed images of the probe spot, on which DT is measured, and pump spot, with the white rectangle delimiting the area selected for PL measurements by the vertical and horizontal slits in the streak camera setup.

employ excitation laser pulses with different duration, different wavelength and may be focused to a different waist, leading to different spatial excitation profiles and time decays that are not easily comparable.

We solved this issue by combining the two measurements into a single ultrafast tandem spectroscopy setup (see Figure 2.1): femtosecond laser pulses excite the sample and PL emission is detected by a picosecond streak camera, while, in the same setting, a transient change in the absorption coefficient is probed by delayed weak broadband laser pulses dispersed in a differential spectrometer. By construction, both PL and DT are produced with the very same train of laser pulses, creating the same excitation density; as shown in Figure 2.1, the two signals are collected from two largely overlapping sample spots.

We then set to apply the tandem spectroscopy technique to understand the relationship between excitons, polarons and free carriers in 2D and 3D HPs. Materials were selected to represent the variety of HPs of current interest. $MAPbI_3$ (with $MA=CH_3NH_3$, methylammonium) was

chosen as prototypical 3D HP absorber for single-junction solar cells, in particular we have also investigated the mixed-cation, mixed-halide variant $MA_{1-x-y}FA_xCs_yPbI_{3-z}Br_z$ (with $FA=HC(NH_2)_2$, formamidinium) where x,y and z represent small fractions with respect to unity, that is successfully applied in solar cells; $MAPbBr_3$ has been included for its potential as light emitter in LEDs and lasers, as photon absorber in photo-detectors or as top junction semiconductor in tandem solar cells. We selected BA_2PbI_4 ($BA=C_4H_{12}N$, n-butylammonium) and BA_2SnI_4 as archetypes of Ruddlesden–Popper 2D layered HPs.[8] Sn-based HPs were included, as replacing poisonous lead is considered a priority and such materials are currently employed to realize the highest photoconversion performances among lead-free HPs.[46–48] The crystal structures and optical properties of the investigated HPs are shown in Figure 2.2 (X-ray diffraction spectra are shown in Figure A.2). The onset of optical absorption spans the visible and near-infrared spectrum, ranging from 530 nm in wavelength for BA_2PbI_4 to 780 nm for $MAPbI_3$. The substitution of iodine with the lighter bromine halogen, as well as quantum confinement of the electronic excitations, widens the gap. The blue shift is accompanied by strengthening of the excitonic resonance at the band-edge. The increasing exciton oscillator strength is related to the larger exciton binding energy E_b, which happens to be comparable to room-temperature thermal energy $k_BT \cong$ 26meV in $MAPbI_3$, but increases to 60 meV in $MAPbBr_3$, i.e., much larger than k_BT at both $T = 77$K and $T = 300$K.[49–51] In 2D HPs, excitons are very robust electronic excitations with several hundreds of meV of binding energy, depending on layer thickness, namely 10-20 times k_BT at room temperature, because of the combined effect of spatial and dielectric confinement.

All HPs we have investigated are bright light emitters. The PL spectra shown in Figure 2.2 are peaked on the low-energy side of the exciton absorption transition. The reciprocity law between absorption and emission forecasts the correct emission spectrum by simply multiplying the absorptance spectrum by the Boltzmann factor to account for population decreasing with increasing energy, as shown in Figure A.3. Reciprocity, therefore, demonstrates that light is emitted by the same states responsible for band-edge absorption, a feature widely accepted in literature and even employed to correlate the emission quantum yield with photovoltaic performance.[7,52–54] In HPs with exciton binding energy much larger than thermal energy, $E_b \gg k_BT$, such as the layered 2D HPs, or $MAPbBr_3$ at low temperature, such reciprocity relation implies that emission is excitonic in nature, because free-carrier emission would be peaked in spectrum at higher photon energies,

blueshifted by $\cong E_b$ with respect to exciton emission, well outside the linewidth of the observed PL spectrum. $MAPbI_3$ and $MA_{1-x-y}FA_xCs_yPbI_{3-z}Br_z$ represent a borderline situation, since $E_b \cong k_BT$ and thus the intensity of light emission from free electron-hole pairs may become comparable to the exciton emission, especially at the high-energy side of the PL spectrum. Whenever free carriers are majority optical excitations however, the emission dynamics turns out to be independent of the nature of the emitting species, free carriers or excitons, since a bimolecular process is always involved, whether is exciton formation as intermediate step before emission or direct recombination of free carriers.

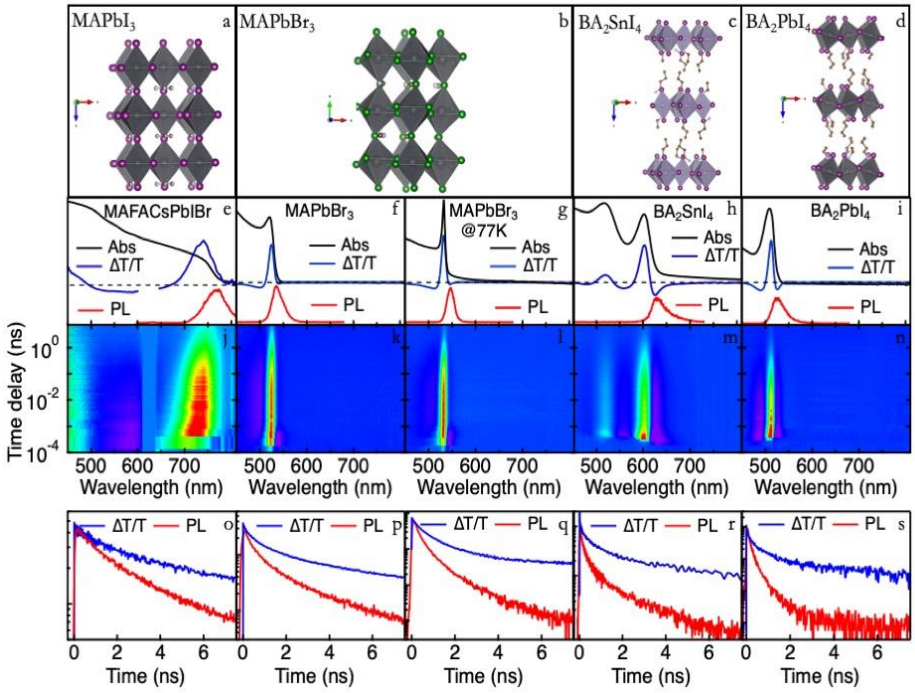

Figure 2.2 Ultrafast tandem spectroscopy on perovskite materials. a)-d) Sketches of the crystal structure of the investigated perovskite materials are depicted in the top row, with prototypical 3D materials ($MA_{1-x-y}FA_xCs_yPbI_{3-z}Br_z$ is a variation of $MAPbI_3$ and $MAPbBr_3$) as well as prototypical layered structures with n=1 (BA_2PbI_4 and BA_2SnI_4); purple dots represent iodine atoms, green dots are bromine one; metal atoms (Pb and Sn) are shown as gray dots; only bulky butylammonium cations are shown while smaller methylammonium ones are omitted for clarity. e)-i) The second row shows for each film the continuous-wave UV-Vis absorption spectrum (black line), the time-integrated differential transmission spectrum (blue line) with a

bleaching spectrum resonant with the exciton absorption peak, and the time-integrated photoluminescence spectrum (red line), also peaked at the exciton resonance; the $MAPbBr_3$ sample has been measured both at room and cryogenic temperature (77 K). The excitation wavelength was 430 nm for all samples, except for $MA_{1-x-y}FA_xCs_yPbI_{3-z}Br_z$, where 630 nm was employed. j)-n) In the third row the complete differential transmission spectrograms are shown, with a logarithmic time axis. o)-s) The fourth row depicts the comparison between the differential transmission (blue line) and photoluminescence (red line) time decays, demonstrating the photoluminescence in all samples is significantly faster than differential transmission.

The DT signal in all HPs shows a dominant bleaching feature, resonant with the lowest excitonic transition, with photoinduced absorption sidebands due to many-body effects.[6,11,55–57] The DT spectrum does not change with the delay, apart from the ultrafast spectral dynamics observed in the first 2ps after excitation, which will be discussed later. The PL decays and the DT transients measured under the same conditions in a window of several nanoseconds after excitation (extracted in a spectral window around the bleaching peak) are compared in Figure 2.2o-s. The comparison between the two transients provides the main preliminary information: PL decays are much faster than the corresponding DT ones, in all HPs. If we assume that the DT signal probes the time evolution of the majority photoexcitations, regardless of whether they are excitons or charged carriers, DT and PL signals are expected to be proportional to each other if the majority species are excitons, emitting light through a monomolecular process. The experimental evidence suggests instead that the majority photoexcited species are charged carriers, requiring a bimolecular process to recombine and therefore causing the PL signal to be proportional to the square of the excited population and to decay faster than DT. While such a picture is familiar for $MAPbI_3$ and $MAPbBr_3$ at room temperature, it is very surprising that the PL intensity decays faster than the DT one also for $MAPbBr_3$ at 77K and even for 2D HPs in which $E_b \gg k_B T$ and majority excitons are expected for all available photoexcitation densities. The possibility that the DT signal could be induced by a minority population of free carriers in a sea of majority excitons can be ruled out on the basis of the expected and observed scaling laws of the PL and DT signals on the laser pulse fluence. If the DT were induced by minority phase of charged carriers, the $PL(t = 0) \equiv PL_0$ intensity would scale linearly with the majority exciton population and thus with the laser fluence, while the DT signal would not be expected to increase linearly, in contrast with experimental

observations shown in the insets of Figure 2.3. The tandem spectroscopy results demonstrate therefore that excitons are always a minority species and are immersed in a plasma of unbound charge carriers. Clearly excitons are still formed, since PL is emitted from excitons, consistently with recent reports,[38–42] but they are not the majority species.

2.2.2 Bimolecular photoluminescence and minority excitons

To study the extent to which photon emission in HPs stems from bimolecular recombination of charged carriers, we quantitatively compare the PL and DT transients, the latter being proportional to the photoexcitation population. Accordingly, Figure 2.3 reports the PL decays as a function of the laser pulse fluence F together with the square of the corresponding DT traces, namely $\left(\frac{\Delta T}{T}\right)^2$, rescaled to match the PL transients. In 3D HPs, PL and DT squared traces are remarkably superimposed. Deviations from this behaviour are only observed at low temperature and for long delay times in $MAPbBr_3$. In 2D $BASnI_4$, the superpositions of the two signals is satisfactory at all densities. A transient overshooting of the PL signal is, however, detected at short delays and lower laser fluences. This behaviour was also recorded in 2D $BAPbI_4$ together with a slower decay of the DT signal at long times for the highest excitation rates. A good agreement between PL and DT squared traces may only occur if PL is generated through bimolecular recombination from the reservoir of photoexcitations that causes the DT signal. Two are the possible scenarios compatible with such dynamics: either free carriers recombine directly to emit light, or excitons are formed in equilibrium as a minority species through bimolecular pairing of free carriers and then emit light with a monomolecular process. The second scenario, exciton emission, appears as the one compatible with reciprocity in 2D HPs and in $MAPbBr_3$ at low temperature, given the fact that the optical emission spectrum is resonant with excitonic absorption. We will therefore adopt from now on the picture of minority bright excitons immersed in a majority plasma of free carriers, since it is the only one compatible with the entire body of experimental data. Possible explanations for the variance from the PL-$\left(\frac{\Delta T}{T}\right)^2$ behaviour will be discussed later on.

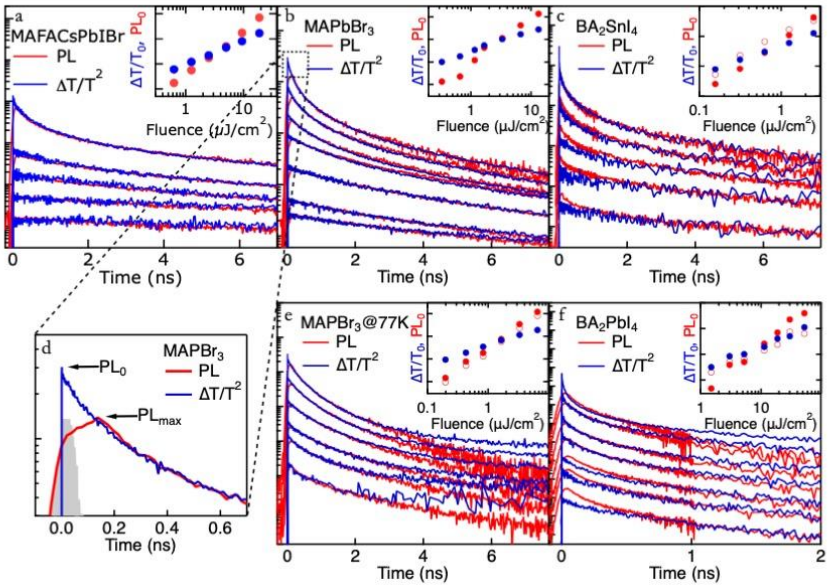

Figure 2.3 Comparison between photoluminescence and square of differential transmission. Each panel shows for each sample the photoluminescence decays (red lines) and the square of differential transmission decays (blue lines, extracted at the maximum of the bleaching signal) as a function of laser fluence. Each pair of decays is measured with the same fluence. The close correspondence between photoluminescence and the square of differential transmission demonstrates that the two techniques monitor two different species, excitons and charged carriers respectively, in chemical equilibrium. The inset in each panel shows as a function of laser fluence the power law for the initial values of differential transmission (solid blue dots), which happens to be linear, and photoluminescence (solid red dots), which instead is quadratic. The temporal resolution of the streak camera smooths the initial photoluminescence transient; to compensate for such an effect, the initial value for the photoluminescence is extracted from the square of the corresponding differential transmission decay, where temporal resolution is around 100 fs. Panel d illustrates the difference between the correct value PL_0 extrapolated according to the procedure and the maximum intensity PL_{max} (maximum values are also added in some insets as empty red dots to visually demonstrate how the apparent power law for PL can be affected by the limited resolution). The curve delimiting the gray-colored area represents the streak camera response function, i.e. the temporal resolution of the detection apparatus.

The equilibrium condition for excitons and free carriers is predicted by Saha's equation,[2,4–6] in the form $n_{cc}^2(t) = n_{eq} n_X(t)$, where $n_X(t)$ and

$n_{cc}(t)$ are the population densities of excitons and charged carriers at time t, while n_{eq} is the equilibrium constant. Since charge carriers are the majority population, $n_{cc} \gg n_X$, then $\frac{\Delta T}{T}(t) \propto n_{cc}(t)$, while $PL(t) \propto n_x(t)$, so that the equilibrium condition implies that $PL \propto \left(\frac{\Delta T}{T}\right)^2$, in agreement with experimental results. The kinetics of the two photoexcitations can therefore be described as a time-sequence of chemical equilibrium states in which the population of one species determines the population of the other one. As a consequence, whatever annihilation process the two types of photoexcitations undergo, the interconversion rate between bound and unbound pairs is always fast enough to guarantee the thermodynamic equilibrium. Significant effects from non-thermal or hot carrier populations were excluded (see Figure A.4).

The equilibrium condition is further supported by the quadratic dependence of the $PL(t = 0) \equiv PL_0$ intensity on the pulse fluence and the $\frac{\Delta T}{T}(t = 0) \equiv \frac{\Delta T}{T}\Big|_0$ linear dependence, as shown in the inset of the $MAPbBr_3$ panel of Figure 2.3. At the highest excitations, the initial transient of the exciton population is very fast and cannot be correctly captured by our PL streak-camera apparatus due to its 50-ps time resolution. The method used to extrapolate PL_0 for kinetics faster than the experimental resolution time is illustrated in the lower-left panel of Figure 2.3. Even when PL results from radiative annihilation of excitons through a monomolecular process, the exciton density increases quadratically with the overall photoexcitation population as long as charged carriers are the majority species and the quasi-stationary Saha equilibrium is achieved. The superlinear PL dependence on the DT signals, close to a quadratic power-law in all HPs, appears as a general, intrinsic feature of 3D and 2D perovskite photophysics and does not depend on extrinsic factors such as traps and defects; results shown in Figure 2.3 were replicated (see Figure A.5) for a pure $MAPbI_3$ perovskite, even though the PL lifetime at low fluences was significantly shorter. Moreover, a quadratic PL with respect to injected carrier concentration was observed even under resonant excitation at the exciton peak in $MAPbBr_3$ at cryogenic temperatures, both under one photon and two-photon excitation (Figure A.6).

Saha's equation forecasts that the ratio of excitons to free carriers increases with excitation fluence so that, for excited-state densities above the equilibrium constant $n_{eq} = \left(\frac{k_B T \tilde{m}_{eh}}{2\pi\hbar^2}\right)^{\frac{3}{2}} e^{-\frac{E_b}{k_B T}}$ most of the photoexcitations are excitons ($\tilde{m}_{eh}$ is the reduced electron-hole mass).

For $MAPbI_3$, $E_b \cong 26meV$ and therefore the equilibrium density is $n_{eq} \cong 1.5 \cdot 10^{17} cm^{-3}$. In $MAPbBr_3$ ($E_b = 64meV$) the predicted crossover occurs at $n_{eq} \cong 3.3 \cdot 10^{16} cm^{-3}$ for $T = 300$ K and $n_{eq} \cong 3.3 \cdot 10^{12} cm^{-3}$ for $T = 77$ K. Above such densities, both PL and DT should monitor the exciton population, and thus $PL \propto \frac{\Delta T}{T}$ is predicted by Saha equilibrium. In all 3D HPs, the densities of photoexcitations created by laser pulses range from slightly above $10^{16} cm^{-3}$ to more than $10^{18} cm^{-3}$ (see Table S1), therefore largely exceeding n_{eq}, by several orders of magnitude at low temperature. Yet, all experimental results reported in Figure 2.3 showed $PL \propto \left(\frac{\Delta T}{T}\right)^2$, meaning that the crossover to an exciton majority was never observed. One possible explanation could be a decrease in E_b for increasing excitation, owing to many-body effects. Yet, this interpretation is ruled out by the observation of a still intense exciton resonance in absorption even at the highest excitation regimes investigated in our experiments (see Figure A.7). Since the exciton oscillator strength f is related to the binding energy by $f \propto E_b^{1.5}$, a marginal reduction in the exciton oscillator strength, e.g. by ten percent, implies that E_b is not significantly reduced either.
The most surprising result in Figure 2.3 is that the linear relationship, $PL \propto \frac{\Delta T}{T}$, was never observed even in 2D HPs, in spite of their giant exciton binding energies. Saha's crossover density in two dimensions reads $n_{eq}^{2D} = \frac{\tilde{m}_{eh} k_B T}{2\pi\hbar^2} e^{-\frac{E_b}{k_B T}} \cong 5 \cdot 10^6 cm^{-2}$ for $E_b \cong 300$ meV at room temperature. In the density regime we explored, $10^9 - 10^{12} cm^{-2}$ (see Table A.1), virtually all photoexcitations are predicted to be excitons, the opposite of what is observed.

2.3 Discussion

2.3.1 Polaron plasma

The formation of a charged carrier plasma as majority photoexcitation at all excitation regimes and in all HP materials calls for a fundamental physical mechanism that favours accumulation of a high density of unbound electrons and holes with respect to bound and charge-neutral excitons. The one mechanism up to now neglected in our analysis is carrier-lattice interaction, which can induce the formation of large charged polarons, as well documented in literature.[11–20] Dressing charged carriers by lattice deformations

brings two main consequences: the first one is that polarons are energetically stabilized with respect to free electrons and holes, meaning that they sit at lower energy and therefore effectively reduce the exciton binding energy; the second one is the heavier mass of polarons than free carriers, which increases the density of states making them entropically favoured with respect to excitons. Both effects reduce the probability of exciton formation, as also inferred from the analytical expression of the modified Saha constant $n_{\mathrm{eq}} = \left(\frac{k_{\mathrm{B}}T\tilde{m}_{\mathrm{p}}}{2\pi\hbar^2}\right)^{\frac{3}{2}} e^{-\frac{E_{\mathrm{b}}-(E_{\mathrm{p}+}+E_{\mathrm{p}-})}{k_{\mathrm{B}}T}}$, in which the exciton binding energy E_{b} is reduced by the stabilization energy for the two polarons ($E_{\mathrm{p}+} + E_{\mathrm{p}-}$), and $\tilde{m}_{\mathrm{eh}}$ is replaced by the much larger mass $\tilde{m}_{\mathrm{p}} = \frac{m_{\mathrm{p}+}m_{\mathrm{p}-}}{m_{\mathrm{e}}+m_{\mathrm{h}}}$, where $m_{\mathrm{p}+,\mathrm{p}-}$ and $m_{\mathrm{e,h}}$ are the polaron and free carrier masses, respectively (see Materials and Methods section for derivation).

We now focus on the situations when experimental data reported in Figure 2.3 deviate from the behaviour $PL \propto \left(\frac{\Delta T}{T}\right)^2$, meaning that the equilibrium condition is not met. We first examine the decay of $\left(\frac{\Delta T}{T}\right)^2$ in $MAPbBr_3$ at 77 K, which becomes slower than the PL's one at long times after excitation. Similar deviations are also observed in BA_2PbI_4. We attribute such deviations to unbalanced populations of positive ($n_{\mathrm{p}+}$) and negative ($n_{\mathrm{p}-}$) polarons that occur at low concentrations due to a more efficient trapping of one of the two polarons by deep defects (or preferential formation of small polarons of one type). Since $PL \propto n_{\mathrm{X}} \propto (n_{\mathrm{p}+} \times n_{\mathrm{p}-})$, while $\frac{\Delta T}{T} \propto (n_{\mathrm{p}+} + n_{\mathrm{p}-})$, unbalanced polaron populations ($n_{\mathrm{p}+} \neq n_{\mathrm{p}-}$) cause the PL signal to decay faster than the square of DT ($PL < \left(\frac{\Delta T}{T}\right)^2$ once the two signals have been normalized at $t = 0$). Tandem spectroscopy proves therefore a suitable optical tool to single out contribution from traps and defects, a key issue in this class of materials.[59]

The deviations from equilibrium observed at short times in 2D HPs, both BA_2SnI_4 and BA_2PbI_4, seem instead of intrinsic nature and could represent the transient photoexcitation dynamics preceding the establishing of chemical equilibrium between excitons and polarons. The $\left(\frac{\Delta T}{T}\right)^2$ curves have been rescaled to fit the long-time PL decays, when light emission results from the excitonic population in equilibrium with polarons. The PL signal at early times overshoots the DT squared one, especially for low fluences. Such overshoot is rationalized as originating from emission of out-of-equilibrium,

geminate excitons, directly created in the absorption process, which dissociate into unbound polaron pairs a few hundred picoseconds after generation. While barely visible for 3D HPs, the observation of geminate excitons becomes evident in 2D systems, presumably due to the stronger Coulomb attraction between photogenerated charged pairs.[60] The finite PL time resolution at the highest fluences in combination with the geminate emission at the lowest excitations explains why the power-law dependence of PL_0 on fluence F leads to an exponent smaller than 2, as also recently reported.[61] We finally mention that the stronger contribution of geminated excitons at lower fluences may imply that thermodynamic equilibrium is not fully established at the carrier generation rates typically involved under continuous-wave excitations, as, e.g., those achievable under solar illumination or LEDs.

2.3.2 Markov dynamics, rate equations and identification of decay processes

Polarons and excitons decay through different channels, so that both their respective population densities are needed to reproduce the observed dynamics. The equilibrium condition however locks the PL and DT decays to each other, since the ratio between the concentration of polarons, n_{p} (assuming $n_{\mathrm{p}+} = n_{\mathrm{p}-}$), and excitons, n_{X}, is fully determined by the equilibrium condition $n_{\mathrm{p}}^2 = n_{\mathrm{eq}} n_{\mathrm{X}}$. As a result, the recombination rates of the photoexcited carriers only depend on the instantaneous value of the total excited-state density $n = n_{\mathrm{p}} + n_{\mathrm{X}} \cong n_{\mathrm{p}}$, regardless of the previous history of the photoexcitations, a situation often referred to as a Markovian process. To highlight the Markov dynamics, DT and PL signals can be shifted on the horizontal time axis traces measured for different initial densities so that they fall on top of each other;[62] the decays obtained for lower fluences match the tails of the ones obtained for higher fluences, as they refer to the same excited-state density. Figure 2.4 demonstrates such a property for both DT and PL decays in all the HPs we have studied. PL and DT traces measured for the same fluence were obviously shifted by the same delay.

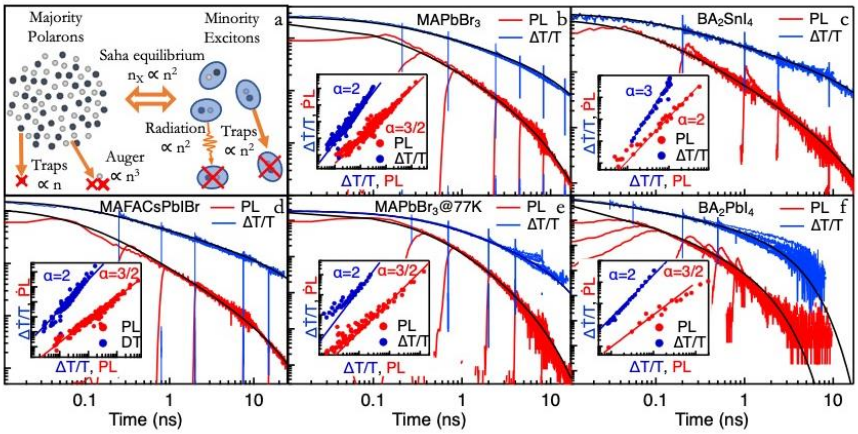

Figure 2.4 Markov dynamics of polaron and excitons according to rate equations. a) Sketch of the chemical equilibrium between a plasma of majority polarons and a minority population of bright excitons; decay channels are shown for both populations, but, because of the equilibrium, decay for each component also affects the other one. b)-f) Series of differential transmission (blue lines) and photoluminescence (red lines) decays, each decay shifted in time according to the procedure discussed in the main text. The rate equation predictions are represented by the black lines; in each panel, the rate equation prediction for PL is the square of the rate equation prediction for differential transmission. The fact that a single rate equation curve can predict the whole dynamics of a series of time-shifted decays demonstrates the Markovian dynamics, i.e. that the time evolution at time t only depends on the excited state density at time t and not on the density at previous times. In the insets, PL and DT time derivatives are plotted as a function of the PL and DT signal amplitudes; the slope in log-log scale represents therefore directly the order of the main decay channel in the rate equation.

While the experimental results clearly show the Markovian nature of the decay of polarons and excitons, few deviations are noticeable in films where trapping of just one type of polarons occurs. In these regimes, the fate of the photoexcitations also depends on the preceding history, namely on the density of long lived trapped polarons. The contribution of non-equilibrium geminate excitons to the PL signal does not satisfy either, as expected, the Markovian test, since the time-shifted decays deviate from a universal curve. Concerning the ubiquitous sub-picosecond spike observed in DT decay curves reported in Figure 2.4, and widely reported in literature, its analysis, detailed in the Materials and Methods section, is consistent with the ultrafast

polaron formation dynamics and highlights the involved many-body effects.

We have now all the elements to identify and quantify the decay processes through the population rate equations, which should account for the main findings emerged from tandem spectroscopy: the chemical equilibrium between excitons and polarons, the prevalence of the polaron population, and the Markovian nature of the recombination processes. As shown in the Materials and Methods section, these conditions lead to the following rate equations for the populations of the majority (polarons, n_{p}) and minority (excitons, n_{X}) species:

$$\dot{n}_{\mathrm{p}} \cong -k_{1,\mathrm{p}} n_{\mathrm{p}} - \left(k_{\mathrm{r,p}} + \frac{k_{1,\mathrm{X}}}{n_{\mathrm{eq}}}\right) n_{\mathrm{p}}^2 - k_{3,\mathrm{p}} n_{\mathrm{p}}^3 \qquad (1)$$

$$\dot{n}_{\mathrm{X}} \cong -2k_{1,\mathrm{p}} n_{\mathrm{X}} - 2\left(k_{\mathrm{r,p}} + \frac{k_{1,\mathrm{X}}}{n_{\mathrm{eq}}}\right) n_{\mathrm{eq}}^{\frac{1}{2}} n_{\mathrm{X}}^{\frac{3}{2}} - 2k_{3,\mathrm{p}} n_{\mathrm{eq}} n_{\mathrm{X}}^2 \qquad (2)$$

Equation 1 holds for both positively and negatively charged polarons, as their populations, created equal by photoexcitation, remain balanced over time owing to the Markovian processes. Remarkably, Equation 1 and 2 are not a system of two independent equations, but effectively a single equation, due to the additional constraint that n_{p} and n_{X} are linked to each other ($n_{\mathrm{p}}^2 = n_{\mathrm{eq}} n_{\mathrm{X}}$); there is therefore only one independent variable and the time decay of n_{X} is forced by the equilibrium condition to be always the square of the n_{p} decay. The rate equation to determine n_{X} is nonetheless explicitly reported to show how the kinetics of the minority species is affected by the interconversion rate establishing a quasi-stationary equilibrium state. In Equation 1, $k_{1,\mathrm{p}}$ stems from polaron trapping. The third order term is proportional to $k_{3,\mathrm{p}}$ and accounts for Auger recombination of three polarons. The second order constant $k_{2,\mathrm{p}}$ is composed by two terms, $k_{\mathrm{r,p}}$ representing the direct bimolecular radiative recombination of charged carriers, and $\frac{k_{1,\mathrm{X}}}{n_{\mathrm{eq}}}$, that comes from the monomolecular recombination of excitons and is a direct consequence of the chemical equilibrium regime, since decayed excitons need to be replenished from the polaron plasma. A decay driven by a quadratic term cannot be therefore taken as a proof of direct radiative recombination of unbound pairs. On the contrary, since PL spectra prove that light emission is excitonic in nature, the rate for direct emission from polarons $k_{\mathrm{r,p}}$ can be neglected in HPs and

hence $k_{2,\mathrm{p}} \cong \frac{k_{1,\mathrm{X}}}{n_{eq}}$, a term that includes both the radiative and non-radiative monomolecular decay of excitons ($k_{1,\mathrm{X}} = k_{\mathrm{r,X}} + k_{\mathrm{nr,X}}$). The equilibrium between polaron plasma and excitons provides therefore a natural explanation for the existence of a nonradiative bimolecular decay channel of polarons as the monomolecular decay of excitons mediated by the interconversion between excitons and polarons.

The rate equation for exciton population (Equation 2) is very unconventional, since excitons are the minority species and their decay is entirely driven by the decay of the polaron density. The monomolecular decay of excitons is therefore due to polaron trapping, which just shows up in the exciton equation with a doubled rate. Exciton trapping, together with polaron bimolecular emission, comes back into the exciton rate equation as a term with exponent 3/2, that could never be produced with a single-species process and is therefore a distinctive feature of the equilibrium condition. The third term is also unexpected, as the quadratic term in the exciton rate equation is not due to bimolecular exciton-exciton annihilation,[61] but is caused by Auger recombination of polarons followed by exciton-to-polaron conversion to maintain chemical equilibrium between the two species.

The functional dependence of PL and DT on the photoexcitation population put forward in the rate equations is fully confirmed by the experiments. Since PL monitors the exciton population ($PL(t) \propto n_{\mathrm{X}}(t)$) and DT monitors polarons ($\frac{\Delta T}{T}(t) \propto n_{\mathrm{p}}(t)$), our analysis protocol simply forecasts that the very same set of fit parameters ought to describe both PL and DT measurements. The pairs of black curves shown in each panel of Figure 2.4 represent coupled PL and DT decays obtained with the same parameters (reported in Table A.2); the agreement between experimental results and calculated curves encompasses four orders of magnitude in time, ranging from 1 picosecond to 20 nanoseconds.

Tandem spectroscopy measurements on different materials explore different regimes for the rate equations, confirming the existence of each of the unconventional terms. To avoid the pitfalls of a multi-parameter fit to the transient kinetics, which may not be very sensitive on the nature of the decay process, we directly identify the leading decay process by plotting in log scale (insets in Figure 2.4) the decay rates of PL and DT signals, $\dot{PL}$ and $\frac{\dot{\Delta T}}{T}$, that are proportional to the exciton and polaron populations, $\dot{n}_{\mathrm{X}}$ and $\dot{n}_{\mathrm{p}}$, respectively, as a function of the signal amplitude themselves ($PL(t) \propto n_{\mathrm{X}}(t)$ and $\frac{\Delta T}{T}(t) \propto n_{\mathrm{p}}(t)$). In most cases, $\dot{n}_{\mathrm{p}}$ growths quadratically in n_{p} and $\dot{n}_{\mathrm{X}}$ increases as $n_{\mathrm{X}}^{\frac{3}{2}}$,

as predicted by the rate equations when the dominant decay channel is the monomolecular decay of excitons. The analysis for BA_2SnI_4 demonstrates the existence of cubic law in DT due to Auger recombination of polarons ($\dot{n}_p \propto n_p^3$) as leading decay rate, coupled to the quadratic term for excitons in PL.

2.3.3 Polaron stabilization energy

If polarons were the lowest-energy states, exciton radiative recombination would be thermally activated, in contrast with experimental evidences in $MAPbBr_3$ and $MAPbI_3$.[63] Therefore, the polaron stabilization energy ($E_{p+} + E_{p-}$) is constrained to be lower than the exciton binding energy E_b. Reciprocity in presence of an exciton linewidth comparable to thermal energy $k_B T$ implies a Stokes shift ΔE_{PL} of the order of the linewidth itself, as the emitting states are the ones on the low-energy tail that are multiplied by a large Boltzmann factor, while the high-energy side of the exciton resonance is comparably suppressed. If we consider such redshift of the PL with respect to the exciton absorption peak, the constrain on polaron energy reads $E_{p+} + E_{p-} < E_b + \Delta E_{PL}$. In $MAPbBr_3$, $\Delta E_{PL} \approx 50$ meV and our experimental estimate of E_b was ≈ 60 meV,[30] which leads to $E_{p+} + E_{p-} < 110$ meV; in $MAPbI_3$, the upper bound condition for the polaron energy is $E_{p+} + E_{p-} \approx 65$ meV ($\Delta E_{PL} \approx 40$ meV and $E_b \approx 25$ meV). Such values represent a rare experimental test for theoretical calculations of polaron energies, that have assessed $E_{p+} + E_{p-} \approx 70$ meV in $MAPbBr_3$ and ≈ 50 meV $MAPbI_3$.[12,30] Several important questions are left to be explored, especially a precise determination of the polaron stabilization energy, understanding similarity and differences in polaron dynamics between 2D and 3D perovskites, how polaron-polaron interactions at high excitation fluences modify the stabilization energy and how stabilization energy is allocated to positive and negative polarons.

2.3.4 Comparison with literature

The photophysics of HPs is the subject of a significant body of literature and it is important to establish how our experimental findings relate to published results. PL measurements taken on their own without the comparison to DT do not allow unambiguous identification of the excited-state species in 2D perovskites and the subsequent attribution of decay processes. The PL_0 dependence on laser fluence has been employed to identify the presence of free carriers in 3D

perovskites,[4,64,65] but a superlinear PL_0 was reported also in 2D perovskites, consistent with our observation, although with a different interpretation.[61]
DT measurements on 2D and 3D perovskites, without matching PL, can also be interpreted with the standard rate equation model, where nonlinear effects can be either attributed to carrier-carrier or exciton-exciton interactions; the DT portion of our measurements is therefore analogous to published results.[6,56,66] The coexistence of bound excitons and large densities of polarons or free-carriers in $MAPbBr_3$ has been recently explored based on DT measurements. [67] The assumption of polaron formation is also consistent with published results, since the sub-ps initial DT spectral dynamics as well as ultrafast coherent oscillations have been described as evidence for polaron formation, in agreement with our interpretation.[11,17,68–70]
The most interesting comparison is perhaps with ultrafast measurements in the THz spectral region, where bound excitons and unbound carriers could be discriminated. THz measurements have provided, together with evidence for free carriers in 3D HPs and ultrafast exciton formation in 2D materials, some interesting signatures of significant presence of free carriers even in 2D perovskites and at low temperatures,[38–42, 68, 69] where only excitons would have been expected. The overall scenario from THz measurements appears therefore compatible with our interpretation of contemporaneous presence of bright excitons and a polaron plasma.
While each piece of data we have presented is consistent with evidences presented in literature, the DT-PL comparison provided by the tandem spectroscopy technique allowed us to introduce the polaron-exciton dynamics to frame HP photophysics, discussed in terms of a chemical thermodynamic equilibrium picture as guiding reference model.

2.4 Conclusions

Charged photoexcitations in hybrid metal halide perovskites can form neutral exciton states with binding energies ranging from thermal energy, $k_B T$, up to several hundreds of meV. When the binding energy exceeds by far $k_B T$ e.g., in 2D HPs or in 3D HPs at low enough temperature, excitons are expected to be the majority photoexcitation species, with significant implications for both charge transport and light emission properties. The light emission rate from a majority population of excitons is expected to scale linearly with the injected

carrier density, radiative recombination of exciton being a monomolecular process. Yet, we have always observed a superlinear light emission rate, even at low temperature and in 2D HPs, an indication that a majority of excitons does not form. Measurements from a ultrafast tandem optical spectroscopy experiment, combining time-resolved photoluminescence and differential transmission in a unified setup, allow to interpret such surprising result as the manifestation of a photoexcitation cycle characteristic of HP materials: a plasma of charged carriers- likely coupled to lattice deformation to form large polarons- forms in chemical quasi-equilibrium with a minority phase of excitons, even when the exciton binding energy by far exceeds thermal energy. Light emitted by HPs is resonant with the exciton transition, while its intensity is determined by the concentration of non-emitting polarons, foreseeing novel mechanisms for LEDs and lasers. 2D HPs materials are considered more stable than 3D counterparts against degradation, but also less suitable for photovoltaics because insulating excitons were believed to prevent charge conduction in the excited state requiring significant energy loss for charge splitting. The presence of high concentrations of charged polarons in place of excitons suggests that such drawbacks are less serious than previously thought and provides a very positive outlook for efficient and stable photovoltaics employing layered perovskites.

2.5 Experimental Section

Materials preparation: The 2D n=1 perovskite films were fabricated by spin coating, at 3000 rpm for 30 s, a 0.13 M solution of 2D single crystals, synthesized as previously described,[71] dissolved in anhydrous dimethylformamide (DMF) at 70°C. After the deposition the films were annealed at 100°C for 10 min.
The 2D n=1 Sn perovskite films were prepared with n-$CH_3(CH_2)_3NH_2I$ (BAI) and SnI_2 dissolved in DMF with a molar ratio 2:1 and a final concentration of 0.5 M. The solution was pre-heated at 70°C for 30 min then 50 µL were dropped on the substrate and spin-coated at 3000 rpm for 30 s. The film was annealed at 75°C for 10 minutes.
The 3D Bromide and Iodide perovskite films were fabricated by one-pot and two-steps spin coating deposition respectively. The $CH_3NH_3PbBr_3$ ($MAPbBr_3$) solution was prepared by dissolving $MABr+PbAc_2*3H_2O$ with a molar ratio 3:1 in DMF and a final

concentration of 0.5 M. The films were deposited on a glass slide at 6000 rpm for 60 s and then annealed at 100°C for 5 minutes.
The $CH_3NH_3PbI_3$ ($MAPbI_3$) solution was prepared by dissolving MAI+$PbCl_2$ with a molar ratio 3:1 in DMF with a final concentration of 0.27 M. The solution was deposited on a glass slide at 6000 rpm then, after 6 s, 150 mL of chlorobenzene were dropped in the center of the spinning substrate and left to spin for an additional 30 s. A 100°C thermal treatment was then performed for 50 minutes.
The $MA_{1-x-y}FA_xCs_yPbI_{3-z}Br_z$ perovskite film was prepared with a 0.3 M precursor solution of FAI, MABr, CsI, PbI_2 and $PbBr_2$ with final stoichiometry $Cs_{0.05}FA_{0.81}MA_{0.14}PbI_{2.55}Br_{0.45}$ in a mixed solvent of DMF and DMSO with a volume ratio of 4:1. The solution was deposited onto a glass substrate with a two-step spin coating procedure. First, two drops of solution were spun at 2000 rpm for 10 s with an acceleration of 200 rpm/s, then at 4000 rpm for 20 s with an acceleration of 1000 rpm/s. Ten seconds before the end of the whole spinning cycle, 100 µL of chlorobenzene were dropped on the substrate. The substrate was then thermally treated at 100 °C on a hotplate for 10 min.
All the film depositions were performed inside a nitrogen-filled glove box.

Materials characterization: The X-ray diffraction patterns of the films were performed with a Siemens D5000 θ-2θ diffractometer, with Cu k_α radiation and graphite monochromator.UV-Vis optical absorption of HP films was measured with a dual-beam spectrophotometer equipped with an integrating sphere accessory (Agilent Technologies Cary 5000 UV-Vis-NIR) to collect diffused transmission and reflection.[72] A simpler procedure was employed only for BA_2SnI_4, measuring just transmission in Perkin Elmer Lambda 950 dual beam spectrometer, in order to avoid sample degradation under ambient humidity.

Ultrafast tandem spectroscopy setup: The laser source was a titanium:sapphire regenerative amplifier (Coherent Libra) delivering 100-fs long pulses, 794 nm in wavelength, up to 4mJ in energy, with a 1KHz repetition rate. The pump pulses were obtained with an optical parametric amplifier (Topas 800 from Light Conversion) equipped with nonlinear crystals. The differential transmission spectrometer (Helios from Ultrafast Systems) measured individual probe and reference spectra with custom CMOS spectrometers achieving 1nm spectral resolution. Home-made optomechanical modifications to the setup allowed collection of luminescence, then dispersed with a grating spectrometer (Acton 2300i) and then detected with the streak camera

(Hamamatsu C10910). The acquisition of PL and DT was done sequentially and the white light probe was blocked while measuring PL. BA_2SnI_4 films were kept in vacuum during measurements.

Physical origin of the DT signal: A DT signal at the lowest allowed exciton resonance (X_0, namely the one observed in photoluminescence) can be due to phase space filling, collisional broadening and other nonlinear interactions. None of these mechanisms necessarily requires a population of the bright excitons X_0. To this regard there exists a vast and robust experimental and theoretical bibliography (particularly the fundamental work by Schmitt-Rink and coworkers in the 80s),[58] especially in inorganic semiconductors with delocalized electronic states (mostly, III-V's quantum wells), much less in organics. As an example, nonlinear interactions of the excitons X_0 with a majority population of dark states can lead to a renormalization of the X_0 wavefunction, which in turns modifies the oscillator strength. The resulting DT signal at the X_0 resonance is proportional to the majority population of dark states. We now address bleaching of the X_0 transition induced by phase space filling. The exciton state is a composite particle made by a pair of interacting electrons and holes. According to Schmitt-Rink et al's theory, an exciton cannot be created in regions of the semiconductor where another electron (or hole, or both) is present because of the Pauli's exclusion principle. As a consequence, the DT signal induced at the X_0 transition is proportional to the sum $an_e + bn_h$, where a and b are constants, while n_e and n_h are, respectively, the overall populations of the electrons and holes. It is worth pointing out that exciton bleaching cannot be ascribed to ground state bleach alone, but includes the excited state, as both ground and excited states may be partly occupied by free carriers, or shared by composite multiparticle states such as excitons, trions, biexcitons, trap states and so on. The bleaching electrons, or holes, can be therefore part of another bound or unbound electron-hole state, that can be either dark or bright, and may not necessarily coincide with the X_0 exciton on which bleaching is detected. As an example, let us consider the case of a bleaching quasi two-particle state made by an unbound electron and hole pair, the former with wavevector k=0 and the second with wavevector much larger than the inverse of the X_0 radius. This state is dark (direct one-photon transition is forbidden), but the electron (not the hole) contributes to the bleaching of the X_0 transition. Even more illuminating is the case of an X_0 exciton with wavevector smaller than the inverse of the exciton radius, but not null. As only X_0 excitons with $k \sim 0$ are bright, this bound electron-hole state is dark,

but, as in the previous case, provides a not negligible contribution to bleaching of the X_0 transition. Same reasoning applies to electrons and holes that, because of lattice relaxation, form large polaron states. Finally, it is worth pointing out that all these bleaching mechanisms scale linearly with the population of the majority species for not too large excitations.

Markov plots and rate equations: Whether or not the photoexcitation kinetics can be described as a Markovian process depends on several factors: intrinsic and extrinsic properties of the materials, the excitation regime and so on. For these reasons, we exploited Markovian plots as a general and powerful tool to demonstrate basic properties of the excited-states in hybrid perovskites, as discussed below, which cannot be unambiguously demonstrated by passing through complicated, and often controversial, multiparameter fit analyses.
The kinetics of charged and neutral photoexcitations would imply considering at least six unknown quantities, the population of free and trapped positive and negative charge carriers, and the population of free and trapped excitons. The Markovian plots for both the DT and PL transients demonstrate unequivocally that the total excitation density is sole independent variable determining the overall kinetics of excitons and charged carriers. How can this happen in a complex dynamic system in which six populations evolve according to six coupled first order ordinary equations (ODEs)? Three are the basic conditions that allow the excited-state transients to be described as a Markovian process: i) the excited species leading to the DT signal (namely, the majority population of charged carriers) and that responsible for the PL (namely, the minority population of excitons) reach the thermodynamic equilibrium in a short time so that at any instant following excitation the population of one species determines the population of the other one; ii) The populations of trapped particles do not play a role in the DT and PL transients in the investigated time-scales, and therefore can be neglected in the coupled ODEs. This does not mean that excitons and charged carriers are not trapped somewhere in the surface or the bulk of the crystal, as they actually are: it simply states that trapping processes enter the ODEs of exciton and charged carrier populations only through constant terms (i.e., which do not depend neither on time nor on space) and do not depend on trap populations (i.e., the rate equations for exciton and charged carrier populations are not coupled to the ODEs describing the population of trap states). If this were not the case, the solution of the ODE systems of excitons and charged particles would depend on the

degree of trap filling, which is determined by the previous history of the relaxation process (and not just by the overall carrier population), and hence the photoexcitation kinetics could not be described as a Markovian process; iii) The population of positive and negative charged carriers are equal. If this condition were not satisfied, the populations of opposite charged carriers would again depend on previous times of the relaxation process and not just on the overall carrier population at a given instant.

Derivation of the rate equations for polaron and exciton populations: The time derivatives $\dot{n}_\mathrm{p}$ and $\dot{n}_\mathrm{X}$ for polaron and exciton populations, once the generation with the pulsed laser is over, can be written accounting for a monomolecular, quadratic and Auger decay for polarons (with constants $k_{1,\mathrm{p}}$, $k_{\mathrm{r,p}}$ and $k_{3,\mathrm{p}}$ respectively, where the r subscript in the quadratic term stands for radiative), as well as a monomolecular decay term for excitons (proportional to $k_{1,\mathrm{X}}$) and an equilibration term that converts excitons into polarons and vice versa driving populations towards chemical equilibrium:

$$\dot{n}_\mathrm{p} \cong -k_{1,\mathrm{p}} n_\mathrm{p} - k_{\mathrm{r,p}} n_\mathrm{p}^2 - k_{3,\mathrm{p}} n_\mathrm{p}^3 - C\left(\frac{n_\mathrm{p}^2}{n_\mathrm{eq}} - n_\mathrm{X}\right) \tag{3}$$

$$\dot{n}_\mathrm{X} \cong -k_{1,\mathrm{X}} n_\mathrm{X} + C\left(\frac{n_\mathrm{p}^2}{n_\mathrm{eq}} - n_\mathrm{X}\right) \tag{4}$$

The total population $n = n_\mathrm{p} + n_\mathrm{X}$ will then decay with the sum of the two rates:

$$\dot{n} \cong -k_{1,\mathrm{p}} n_\mathrm{p} - k_{\mathrm{r,p}} n_\mathrm{p}^2 - k_{3,\mathrm{p}} n_\mathrm{p}^3 - k_{1,\mathrm{X}} n_\mathrm{X} \tag{5}$$

Assuming the equilibrium is always maintained, the additional condition $n_\mathrm{p}^2 = n_\mathrm{eq} n_\mathrm{X}$ has to be met.
Furthermore, experiments demonstrate that polarons are the majority species, so that their decay rate will be well approximated by the total rate:

$$\dot{n}_\mathrm{p} \cong \dot{n} \cong -k_{1,\mathrm{p}} n_\mathrm{p} - \left(k_{\mathrm{r,p}} + \frac{k_{1,\mathrm{X}}}{n_\mathrm{eq}}\right) n_\mathrm{p}^2 - k_{3,\mathrm{p}} n_\mathrm{p}^3 \tag{6}$$

meaning that because of the equilibrium condition, the decay of excitons shows up as a quadratic decay term in the population of polarons, since polarons are depleted to replenish the decayed excitons.

Since exciton and polaron populations are linked by their equilibrium conditions, so are their decay rates, as obtained by taking the time derivative of chemical equilibrium: $2n_{\mathrm{p}}\dot{n}_{\mathrm{p}} = n_{\mathrm{eq}}\dot{n}_{\mathrm{X}}$.
This is the reason why decays of order α for polarons, i.e. proportional to n_{p}^{α}, produce terms $\propto n_{\mathrm{p}}^{\alpha+1} \propto n_{\mathrm{X}}^{\frac{\alpha+1}{2}}$ in the exciton decay rate.

Now $\dot{n}_{\mathrm{X}}$ can be simply obtained as:

$$\dot{n}_{\mathrm{X}} = \frac{2n_{\mathrm{p}}\dot{n}_{\mathrm{p}}}{n_{\mathrm{eq}}} \cong -2k_{1,\mathrm{p}}\frac{n_{\mathrm{p}}^2}{n_{\mathrm{eq}}} - 2\left(k_{\mathrm{r,p}} + \frac{k_{1,\mathrm{X}}}{n_{\mathrm{eq}}}\right)\frac{n_{\mathrm{p}}^3}{n_{\mathrm{eq}}} - 2k_{3,\mathrm{p}}\frac{n_{\mathrm{p}}^4}{n_{\mathrm{eq}}} =$$
$$= -2k_{1,\mathrm{p}}n_{\mathrm{X}} - 2\left(k_{\mathrm{r,p}} + \frac{k_{1,\mathrm{X}}}{n_{\mathrm{eq}}}\right)n_{\mathrm{eq}}^{\frac{1}{2}}n_{\mathrm{X}}^{\frac{3}{2}} - 2k_{3,\mathrm{p}}n_{\mathrm{eq}}n_{\mathrm{X}}^2 \qquad (7)$$

Since the density of excitons appear always to much lower than polaron density, exciton-exciton interaction has not been included for consistency, as it would produce a term proportional to n_{p}^4 in the rate equation for polarons and to $n_{\mathrm{X}}^{\frac{5}{2}}$ in the rate equation for excitons.

The modified Saha's equation for polaron and exciton populations: The populations of excitons and polarons can be expressed in terms of their chemical potentials ($\mu_{\mathrm{X}}, \mu_{\mathrm{p+}}$ and $\mu_{\mathrm{p-}}$ for excitons, positive and negative polarons respectively) as follows:

$$n_{\mathrm{X}} = 4\left[\frac{k_{\mathrm{B}}T(m_{\mathrm{e}} + m_{\mathrm{h}})}{2\pi\hbar^2}\right]^{\frac{3}{2}} e^{-\frac{E_{\mathrm{g}} - E_{\mathrm{b}} - \mu_{\mathrm{X}}}{k_{\mathrm{B}}T}} \qquad (8)$$

$$n_{\mathrm{p-}} = 2\left(\frac{k_{\mathrm{B}}Tm_{\mathrm{p-}}}{2\pi\hbar^2}\right)^{\frac{3}{2}} e^{-\frac{E_{\mathrm{c}} - E_{\mathrm{p-}} - \mu_{\mathrm{p-}}}{k_{\mathrm{B}}T}} \qquad (9)$$

$$n_{\mathrm{p+}} = 2\left(\frac{k_{\mathrm{B}}Tm_{\mathrm{p+}}}{2\pi\hbar^2}\right)^{\frac{3}{2}} e^{-\frac{E_{\mathrm{v}} + E_{\mathrm{p+}} + \mu_{\mathrm{p+}}}{k_{\mathrm{B}}T}} \qquad (10)$$

where E_{g} is the energy gap; E_{c} and E_{v} are the energies of the conduction and valence band extrema, respectively. If polarons are in chemical equilibrium with excitons, it follows that the chemical potentials of polarons pairs and that of excitons are equal: $\mu_{\mathrm{p+}} + \mu_{\mathrm{p-}} = \mu_{\mathrm{X}}$. The modified Saha's equation thus reads:

$$\frac{n_{\mathrm{p}+}n_{\mathrm{p}-}}{n_{\mathrm{X}}} = n_{\mathrm{eq}} = \left(\frac{k_{\mathrm{B}}T\widetilde{m}_{\mathrm{p}}}{2\pi\hbar^2}\right)^{\frac{3}{2}} e^{-\frac{E_{\mathrm{b}}-(E_{\mathrm{p}+}+E_{\mathrm{p}-})}{k_{\mathrm{B}}T}} \tag{11}$$

where $\widetilde{m}_{\mathrm{p}} = \frac{m_{\mathrm{p}+}m_{\mathrm{p}-}}{m_{\mathrm{e}}+m_{\mathrm{h}}}$. In the limit of a negligible polaron effect ($E_{\mathrm{p}+} + E_{\mathrm{p}-} \to 0, m_{\mathrm{p}-(+)} \to m_{\mathrm{e(h)}}$), the usual Saha's equation is recovered.

Analysis of DT for polaron formation and size: We analysed the sub-picosecond DT transients in analogy to similar analysis in literature that have attributed such transients to polaron formation.[11,23] We discuss the results of $MAPbBr_3$ and BA_2SnI_4, representative of 3D and 2D HPs, respectively. Figure A.8 shows the initial decay of the DT signal, for photon energies close to the exciton resonance for different pulse fluences. The fast contribution vanishes at the highest excitations. However, as we now show, this behaviour does not monitor the inhibition of polaron formation at high densities, but rather a modification of many-body interactions when polaron states are not formed yet. DT spectra acquired at two delays are reported in Figure A.8: the first one was taken at the maximum t_1=0.3 ps of the spikes reported in Figure 2.4, at the early stage of lattice relaxation, which is expected to be completed within 1ps;[11] the second one at t_2=2-5 ps, when the fast contribution has disappeared and photoexcitations are dressed by lattice distortion. We are actually interested in the absorbance changes, induced by polaron formation. These perturbations can be monitored by analysing the difference between DT spectra taken at the two delays, t_1 and t_2. For $MAPbBr_3$ at 77K (Figure A.8a) at low pulse fluences ($\phi = 1\mu J/cm^2$), the difference spectrum presents a negative peak centred at the exciton resonance, corresponding to a bleaching of the excitonic transition, counterbalanced by an induced absorption of equal strength on the low energy side. We attribute the nonlinear absorption signal to the excitation of a trion state, namely a composite particle made by an electron (hole) bound to an exciton. The photon absorption cross-section to form the three-particle state in presence of a population of charged carriers (electrons or holes) occurs at the expense of the optical excitation of neutral excitons, thus leading to a comparable reduction of the exciton oscillator strength. After reorganization of the polar lattice around charged carriers, Coulomb screening is enhanced, making the trion state unstable and, consequently, inducing the disappearance of the associated absorption peak and an increase of absorption at the exciton resonance. Increasing fluences, the difference spectrum broadens and the zero crossing shifts to higher energies until

it matches the exciton energy. The observed spectral shape now monitors a red shift of the exciton line produced by the initially photoexcited electron-hole plasma. At these fluences, the higher plasma density screens the Coulomb interaction between excitons and free carriers, which on one side destabilizes trion states but, on the other hand, induces a redshift of the exciton resonance. Both this latter many-body effect and the trion resonance gradually disappear after polaron formation. The sub-picosecond transient of the nonlinear response, triggered by lattice relaxation in the excited-state, is observed even at the highest fluences, $\phi = 36$ mJ/cm^2, corresponding to an injected photoexcitation population of 5.7×10^{18} cm^{-3}, equivalent to a polaron-polaron mean distance r=6.9 nm (see Figure A.8). Polar lattice deformations around the electronic excitations have a finite extension r_p. At high excitations, the interparticle distance can approach $2r_p$. Polaron-polaron interaction is expected to trigger a readjustment of the phonon cloud around charged carriers, which would result in polaron states with a more free-carrier character. In the low-density limit, first-principle calculations provided a lower bound estimate for positive polarons in $MAPbBr_3$, $2r_p$= 5.0 nm, which is smaller than the minimum interparticle distance reached in the highest excitation regime investigated in our experiments.[12,14,24,30] We finally recall that the excitonic resonance is still well resolved even at the highest fluences, which means that the excited semiconductor is well below the Mott density above which bound electron-hole states cannot exist. Figure A.8 also shows the nonlinear response of BA_2SnI_4. With respect to the case of $MAPbBr_3$, we observed only the low-density regime in which optical formation of trions is inhibited after lattice reorganization around charged carriers. Finally, ultrafast transients last a few hundred femtoseconds as in $MAPbBr_3$, with an intensity that is independent of fluence.

2.6 References

[1] C. C. Stoumpos, M. G. Kanatzidis, *Acc. Chem. Res.* **2015**, *48*, 2791.

[2] L. M. Herz, *Annu. Rev. Phys. Chem.* **2016**, *67*, 65.

[3] J. Huang, Y. Yuan, Y. Shao, Y. Yan, *Nat. Rev. Mater.* **2017**, *2*, 17042.

[4] M. Saba, M. Cadelano, D. Marongiu, F. Chen, V. Sarritzu, N. Sestu, C. Figus, M. Aresti, R. Piras, A. Geddo Lehmann, C. Cannas, A. Musinu, F. Quochi, A. Mura, G. Bongiovanni, *Nat. Commun.* **2014**, *5*, 5049.

[5] V. D'Innocenzo, G. Grancini, M. J. P. Alcocer, A. R. S. Kandada, S. D. Stranks, M. M. Lee, G. Lanzani, H. J. Snaith, A. Petrozza, *Nat. Commun.* **2014**, *5*, 3586.

[6] J. S. Manser, P. V. Kamat, *Nat. Photonics* **2014**, *8*, 737.

[7] D. Marongiu, M. Saba, F. Quochi, A. Mura, G. Bongiovanni, *J. Mater. Chem. C* **2019**, *7*, 12006.

[8] C. C. Stoumpos, D. H. Cao, D. J. Clark, J. Young, J. M. Rondinelli, J. I. Jang, J. T. Hupp, M. G. Kanatzidis, *Chem. Mater.* **2016**, *28*, 2852.

[9] T. M. Koh, B. Febriansyah, N. Mathews, *Chem* **2017**, *2*, 326.

[10] H. Tsai, W. Nie, J. C. Blancon, C. C. Stoumpos, R. Asadpour, B. Harutyunyan, A. J. Neukirch, R. Verduzco, J. J. Crochet, S. Tretiak, L. Pedesseau, J. Even, M. A. Alam, G. Gupta, J. Lou, P. M. Ajayan, M. J. Bedzyk, M. G. Kanatzidis, A. D. Mohite, *Nature* **2016**, *536*, 312.

[11] G. Batignani, G. Fumero, A. R. Srimath Kandada, G. Cerullo, M. Gandini, C. Ferrante, A. Petrozza, T. Scopigno, *Nat. Commun.* **2018**, *9*, 1971.

[12] D. Ghosh, E. Welch, A. J. Neukirch, A. Zakhidov, S. Tretiak, *J. Phys. Chem. Lett.* **2020**, *11*, 3271.

[13] H. Cho, Y. H. Kim, C. Wolf, H. D. Lee, T. W. Lee, *Adv. Mater.* **2018**, *30*, 1704587.

[14] C. Motta, S. Sanvito, *J. Phys. Chem. C* **2018**, *122*, 1361.

[15] T. Ivanovska, C. Dionigi, E. Mosconi, F. De Angelis, F. Liscio, V. Morandi, G. Ruani, *J. Phys. Chem. Lett.* **2017**, *8*, 3081.

[16] M. Schlipf, S. Poncé, F. Giustino, *Phys. Rev. Lett.* **2018**, *121*, 086402.

[17] H. Zhu, K. Miyata, Y. Fu, J. Wang, P. P. Joshi, D. Niesner, K. W. Williams, S. Jin, X. Y. Zhu, *Science* **2016**, *353*, 1409.

[18] F. G. Santomauro, J. Grilj, L. Mewes, G. Nedelcu, S. Yakunin, T. Rossi, G. Capano, A. Al Haddad, J. Budarz, D. Kinschel, D. S. Ferreira, G. Rossi, M. G. Tovar, D. Grolimund, V. Samson, M. Nachtegaal, G. Smolentsev, M. V. Kovalenko, M. Chergui, *Struct. Dyn.* **2017**, *4*, 044002.

[19] C. Liu, H. Tsai, W. Nie, D. J. Gosztola, X. Zhang, *J. Phys. Chem. Lett.* **2020**, *11*, 6256.

[20] M. Puppin, S. Polishchuk, N. Colonna, A. Crepaldi, D. N. Dirin, O. Nazarenko, R. De Gennaro, G. Gatti, S. Roth, T. Barillot, L. Poletto, R. P. Xian, L. Rettig, M. Wolf, R. Ernstorfer, M. V. Kovalenko, N. Marzari, M. Grioni, M. Chergui, *Phys. Rev. Lett.* **2019**, *124*, 206402.

[21] J. M. Frost, L. D. Whalley, A. Walsh, *ACS Energy Lett.* **2017**, *2*, 2647.

[22] D. Niesner, H. Zhu, K. Miyata, P. P. Joshi, T. J. S. Evans, B. J. Kudisch, M. T. Trinh, M. Marks, X. Y. Zhu, *J. Am. Chem. Soc.* **2016**, *138*, 15717.

[23] K. Miyata, D. Meggiolaro, M. Tuan Trinh, P. P. Joshi, E. Mosconi, S. C. Jones, F. De Angelis, X. Y. Zhu, *Sci. Adv.* **2017**, *3*, e1701217.

[24] M. Bokdam, T. Sander, A. Stroppa, S. Picozzi, D. D. Sarma, C. Franchini, G. Kresse, *Sci. Rep.* **2016**, *6*, 28618.

[25] F. Zheng, L. W. Wang, *Energy Environ. Sci.* **2019**, *12*, 1219.

[26] H. H. Fang, S. Adjokatse, S. Shao, J. Even, M. A. Loi, *Nat. Commun.* **2018**, *9*, 243.

[27] S. Kahmann, M. A. Loi, *J. Mater. Chem. C* **2019**, *7*, 2471.

[28] M. Li, J. Fu, Q. Xu, T. C. Sum, *Adv. Mater.* **2019**, *31*, 1802486.

[29] J. M. Frost, *Phys. Rev. B* **2017**, *96*, 195202.

[30] D. Meggiolaro, F. Ambrosio, E. Mosconi, A. Mahata, F. De Angelis, *Adv. Energy Mater.* **2019**, *10*, 1902748.

[31] A. Mahata, D. Meggiolaro, F. De Angelis, *J. Phys. Chem. Lett.* **2019**, *10*, 1790.

[32] A. M. Soufiani, F. Huang, P. Reece, R. Sheng, A. Ho-Baillie, M. A. Green, *Appl. Phys. Lett.* **2015**, *107*, 231902.

[33] J. Yin, P. Maity, R. Naphade, B. Cheng, J. H. He, O. M. Bakr, J. L. Brédas, O. F. Mohammed, *ACS Nano* **2019**, *13*, 12621.

[34] A. R. Srimath Kandada, C. Silva, *J. Phys. Chem. Lett.* **2020**, *11*, 3173.

[35] H. Esmaielpour, V. R. Whiteside, S. Sourabh, G. E. Eperon, J. T. Precht, M. C. Beard, H. Lu, B. K. Durant, I. R. Sellers, *J. Phys. Chem. C* **2020**, *124*, 9496.

[36] J. Yin, H. Li, D. Cortecchia, C. Soci, J. L. Brédas, *ACS Energy Lett.* **2017**, *2*, 417.

[37] X. Jia, J. Jiang, Y. Zhang, J. Qiu, S. Wang, Z. Chen, N. Yuan, J. Ding, *Appl. Phys. Lett.* **2018**, *112*, 143903.

[38] M. C. Gélvez-Rueda, E. M. Hutter, D. H. Cao, N. Renaud, C. C. Stoumpos, J. T. Hupp, T. J. Savenije, M. G. Kanatzidis, F. C. Grozema, *J. Phys. Chem. C* **2017**, *121*, 26566.

[39] A. Kumar, A. Solanki, M. Manjappa, S. Ramesh, Y. K. Srivastava, P. Agarwal, T. C. Sum, R. Singh, *Sci. Adv.* **2020**, *6*, eaax8821.

[40] G. Folpini, L. Gatto, D. Cortecchia, M. Devetta, G. Crippa, C. Vozzi, S. Stagira, A. Petrozza, E. Cinquanta, *J. Chem. Phys.* **2020**, *152*, 214705.

[41] O. F. Williams, N. Zhou, J. Hu, Z. Ouyang, A. Kumbhar, W. You, A. M. Moran, *J. Phys. Chem. A* **2019**, *123*, 11012.

[42] A. Burgos-Caminal, E. Socie, M. E. F. Bouduban, J. E. Moser, *J. Phys. Chem. Lett.* **2020**, *11*, 7692.

[43] A. Burgos-Caminal, E. Socie, M. E. F. Bouduban, J.-E. Moser, *J. Phys. Chem. Lett.* **2020**, *11*, 7692.

[44] L. Luo, L. Men, Z. Liu, Y. Mudryk, X. Zhao, Y. Yao, J. M. Park, R. Shinar, J. Shinar, K. M. Ho, I. E. Perakis, J. Vela, J. Wang, *Nat. Commun.* **2017**, *8*, 15565.

[45] F. Deschler, M. Price, S. Pathak, L. E. Klintberg, D. D. Jarausch, R. Higler, S. Hüttner, T. Leijtens, S. D. Stranks, H. J. Snaith, M. Atatüre, R. T. Phillips, R. H. Friend, *J. Phys. Chem. Lett.* **2014**, *5*, 1421.

[46] J.-P. Correa-Baena, M. Saliba, T. Buonassisi, M. Grätzel, A. Abate, W. Tress, A. Hagfeldt, *Science* **2017**, *358*, 739.

[47] M. Wei, K. Xiao, G. Walters, R. Lin, Y. Zhao, M. I. Saidaminov, P. Todorović, A. Johnston, Z. Huang, H. Chen, A. Li, J. Zhu, Z. Yang, Y. K. Wang, A. H. Proppe, S. O. Kelley, Y. Hou, O. Voznyy, H. Tan, E. H. Sargent, *Adv. Mater.* **2020**, *32*, 1907058.

[48] W. Ke, C. C. Stoumpos, M. Zhu, L. Mao, I. Spanopoulos, J. Liu, O. Y. Kontsevoi, M. Chen, D. Sarma, Y. Zhang, M. R. Wasielewski, M. G. Kanatzidis, *Sci. Adv.* **2017**, *3*, e1701293.

[49] M. Baranowski, P. Plochocka, *Adv. Energy Mater.* **2020**, *10*, 1903659.

[50] Y. Jiang, X. Wang, A. Pan, *Adv. Mater.* **2019**, *31*, 1806671.

[51] N. Sestu, M. Cadelano, V. Sarritzu, F. Chen, D. Marongiu, R. Piras, M. Mainas, F. Quochi, M. Saba, A. Mura, G. Bongiovanni, *J. Phys. Chem. Lett.* **2015**, *6*, 4566.

[52] C. L. Davies, M. R. Filip, J. B. Patel, T. W. Crothers, C. Verdi, A. D. Wright, R. L. Milot, F. Giustino, M. B. Johnston, L. M. Herz, *Nat. Commun.* **2018**, *9*, 293.

[53] V. Sarritzu, N. Sestu, D. Marongiu, X. Chang, S. Masi, A. Rizzo, S. Colella, F. Quochi, M. Saba, A. Mura, G. Bongiovanni, *Sci. Rep.* **2017**, *7*, 44629.

[54] M. Stolterfoht, C. M. Wolff, J. A. Márquez, S. Zhang, C. J. Hages, D. Rothhardt, S. Albrecht, P. L. Burn, P. Meredith, T. Unold, D. Neher, *Nat. Energy* **2018**, *3*, 847.

[55] B. Anand, S. Sampat, E. O. Danilov, W. Peng, S. M. Rupich, Y. J. Chabal, Y. N. Gartstein, A. V Malko, *Phys. Rev. B* **2016**, *93*, 161205.

[56] Y. Yang, M. Yang, Z. Li, R. Crisp, K. Zhu, M. C. Beard, *J. Phys. Chem. Lett.* **2015**, *6*, 4688.

[57] K. Pydzińska, J. Karolczak, M. Szafrański, M. Ziółek, *RSC Adv.* **2018**, *8*, 6479.

[58] S. Schmitt-Rink, D. S. Chemla, D. A. B. Miller, *Phys. Rev. B* **1985**, *32*, 6601.

[59] J. M. Ball, A. Petrozza, *Nat. Energy* **2016**, *1*, 16149.

[60] V. Sarritzu, N. Sestu, D. Marongiu, X. Chang, Q. Wang, M. A. Loi, F. Quochi, M. Saba, A. Mura, G. Bongiovanni, *Adv. Opt. Mater.* **2018**, *6*, 1700839.

[61] G. Delport, G. Chehade, F. Lédeé, H. Diab, C. Milesi-Brault, G. Trippé-Allard, J. Even, J. S. Lauret, E. Deleporte, D. Garrot, *J. Phys. Chem. Lett.* **2019**, *10*, 5153.

[62] J. M. Richter, M. Abdi-Jalebi, A. Sadhanala, M. Tabachnyk, J. P. H. Rivett, L. M. Pazos-Outón, K. C. Gödel, M. Price, F. Deschler, R. H. Friend, *Nat. Commun.* **2016**, *7*, 13941.

[63] V. Sarritzu, N. Sestu, D. Marongiu, X. Chang, Q. Wang, S. Masi, S. Colella, A. Rizzo, A. Gocalinska, E. Pelucchi, M. L. Mercuri, F. Quochi, M. Saba, A. Mura, G. Bongiovanni, *Adv. Opt. Mater.* **2018**, *6*, 1701254.

[64] M. B. Johnston, L. M. Herz, *Acc. Chem. Res.* **2016**, *49*, 146.

[65] M. Saba, F. Quochi, A. Mura, G. Bongiovanni, *Acc. Chem. Res.* **2016**, *49*, 166.

[66] J. Cho, J. T. DuBose, P. V. Kamat, *J. Phys. Chem. Lett.* **2020**, *11*, 2570.

[67] T. Palmieri, E. Baldini, A. Steinhoff, A. Akrap, M. Kollár, E. Horváth, L. Forró, F. Jahnke, M. Chergui, *Nat. Commun.* **2020**, *11*, 850.

[68] T. Ghosh, S. Aharon, L. Etgar, S. Ruhman, *J. Am. Chem. Soc.* **2017**, *139*, 18262.

[69] W. Zhao, Z. Qin, C. Zhang, G. Wang, X. Dai, M. Xiao, *Appl. Phys. Lett.* **2019**, *115*, 243101.

[70] Z. Liu, C. Vaswani, L. Luo, D. Cheng, X. Yang, X. Zhao, Y. Yao, Z. Song, R. Brenes, R. J. H. Kim, J. Jean, V. Bulović, Y. Yan, K.-M. Ho, J. Wang, *Phys. Rev. B* **2020**, *101*, 115125.

[71] D. H. Cao, C. C. Stoumpos, O. K. Farha, J. T. Hupp, M. G. Kanatzidis, *J. Am. Chem. Soc.* **2015**, *137*, 7843.

[72] D. Marongiu, S. Lai, V. Sarritzu, E. Pinna, G. Mula, M. Laura Mercuri, M. Saba, F. Quochi, A. Mura, G. Bongiovanni, *ACS Appl. Mater. Interfaces* **2019**, *11*, 10021.

Appendix A: Additional data to Chapter 2

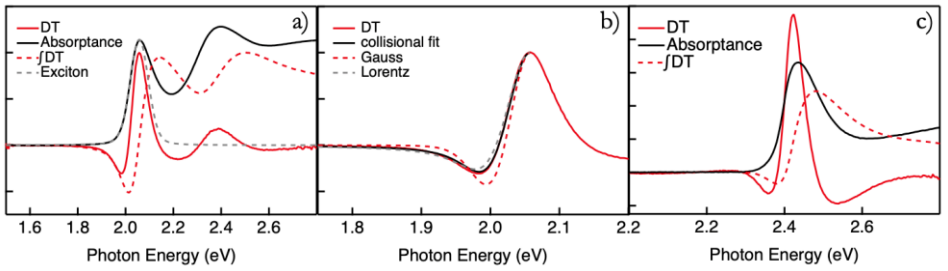

Figure A.1 DT spectral analysis
a) BA_2SnI_4. Black line: absorption coefficient; Grey dashed line: best line-fit [Voigt profile, $V(\hbar\omega, \Gamma_G, \Gamma_L)$] to the low-energy side of the exciton absorption coefficient ($\hbar\omega < E_X$). Full-width of the absorption line at half-maximum (Γ_G) of the gaussian contribution is 81 meV, the Lorentzian one (Γ_L) is 18 meV; Red line: DT signal (t=2-10 ps, F= 7.5 mJ/cm²); red dashed line: I-DT: spectra integral of the DT signal ($\int_{-\infty}^{\hbar\omega} DT(E)dE$). I-DT crosses zero at the exciton energy E_X, as expected for nonlinear differential transmission caused by collisional broadening.
b) Comparison of broadening mechanisms in the DT lineshape for BA_2SnI_4. Red line: DT signal (t=2-10 ps); Black line: best line-fit to the low energy side ($\hbar\omega < E_X$) of the experimental DT signal by assuming collisional broadening as the main nonlinearity: $DT\_Fit(\hbar\omega) = \frac{\partial V(\hbar\omega,\Gamma_G,\Gamma_L)}{\partial \Gamma_G}\delta\Gamma_G + \frac{\partial V(\hbar\omega,\Gamma_G,\Gamma_L)}{\partial \Gamma_L}\delta\Gamma_L$, $\delta\Gamma_G$ =13 meV ($\frac{\delta\Gamma_G}{\Gamma_G} = 0.27$) and $\delta\Gamma_L$=30 meV ($\frac{\delta\Gamma_L}{\Gamma_L} = 3.4$). Grey dashed line: lineshape of the pure Lorentzian contribution. Red dashed line: lineshape of the pure Gaussian contribution. Comparison with the experimental DT signal shows that the leading contribution is, by far, Lorentzian with an extended low energy tail, as expected for a nonlinear mechanism induced by exciton-charged carrier scattering.
c) BA_2PbI_4 DT spectral analysis. Black line: absorption coefficient; Red line: DT signal (t=1-2 ps, F= 18.8 mJ/cm²); Dashed red line: spectral integral of the DT signal ($\int_{-\infty}^{\hbar\omega} DT(E)dE$). I-DT crosses zero at an energy lower than E_X, suggesting that different nonlinear mechanisms drive the nonlinear response of BA_2PbI_4.

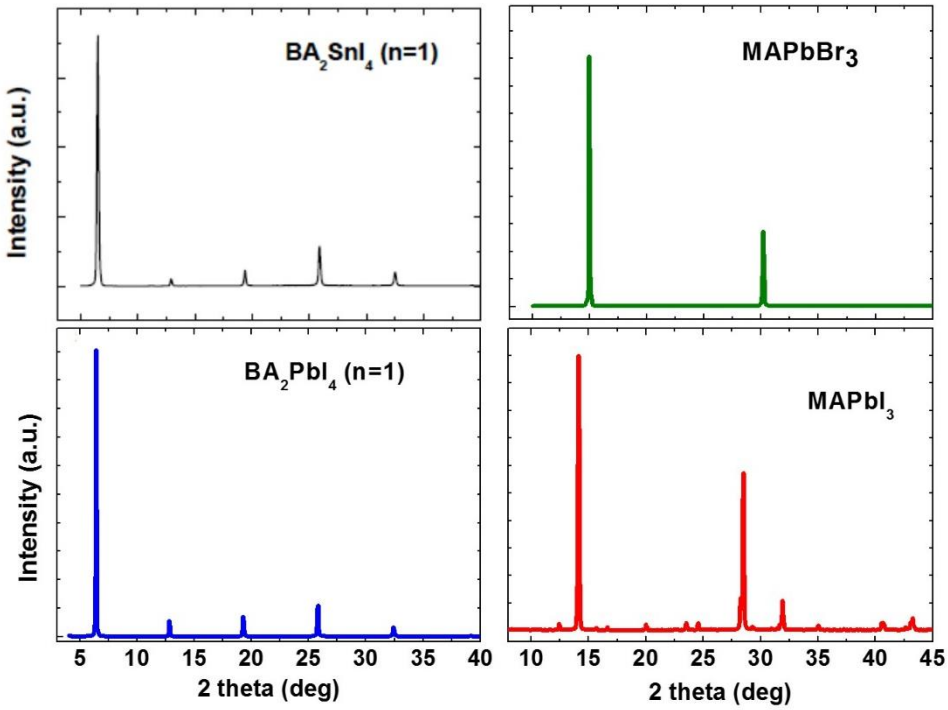

Figure A.2 XRD spectra for measured samples.

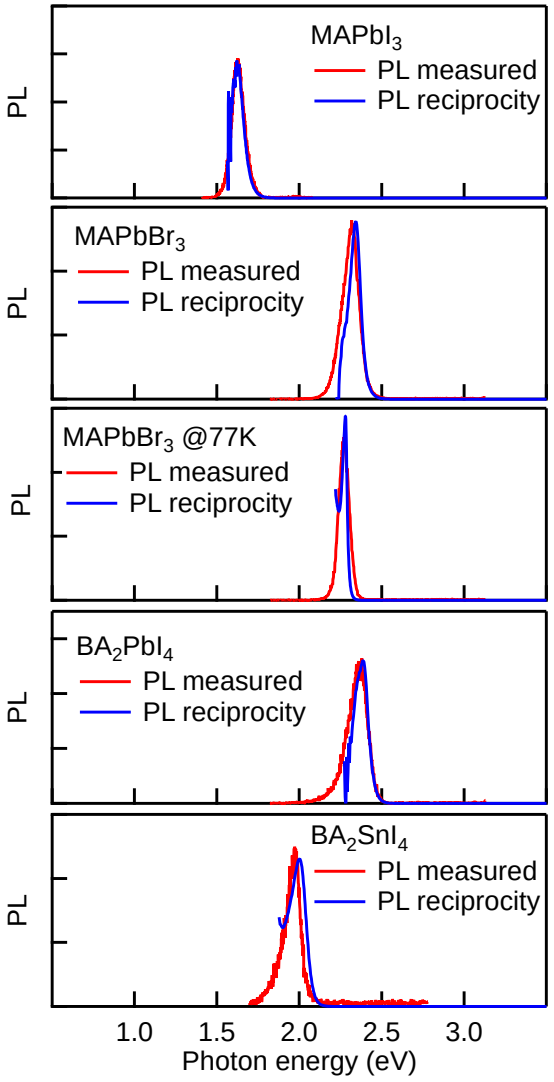

Figure A.3 Reciprocity relation. PL spectra for various HPs as measured and as predicted by the reciprocity relation starting from absorption spectra.

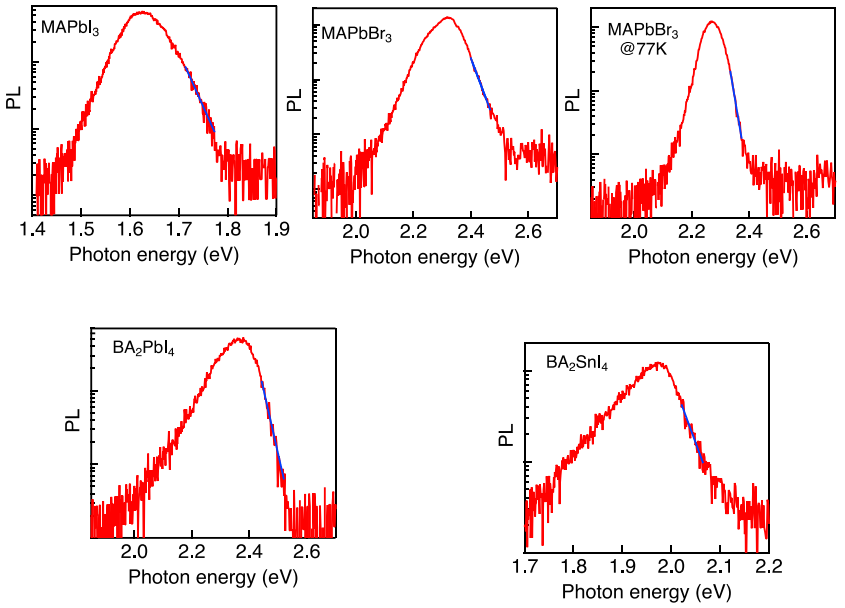

Figure A.4 Carrier temperature. PL spectra obtained for all investigated samples under pulsed excitation and integrated in a 10 ns window were analyzed to identify the thermal distribution of excited carriers. The high-energy tail of the PL spectra was fitted with the Boltzmann function (blue lines) expected for a non-degenerate thermal population ($PL(\hbar\omega) \propto (\hbar\omega)^2 e^{-\frac{\hbar\omega}{k_B T}}$) and the temperature resulting from the least square fit always resulted to be less than 20K larger than the sample temperature. Possible hot carrier populations would show as deviation from the fitting curve and were below our detection limit.

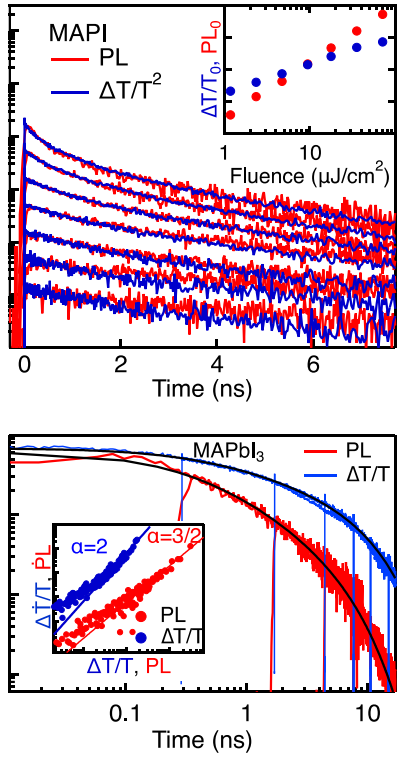

Figure A.5 Tandem spectroscopy on pure $MAPbI_3$ perovskite sample. Top panel: PL and DT squared decays superimposed, with signals at time zero as a function of fluence (inset), like in Figure 3 in the main text for other materials. Bottom panel: Markov plots and power laws (inset), analogous to what shown in Figure 4 in the main text for all other materials.

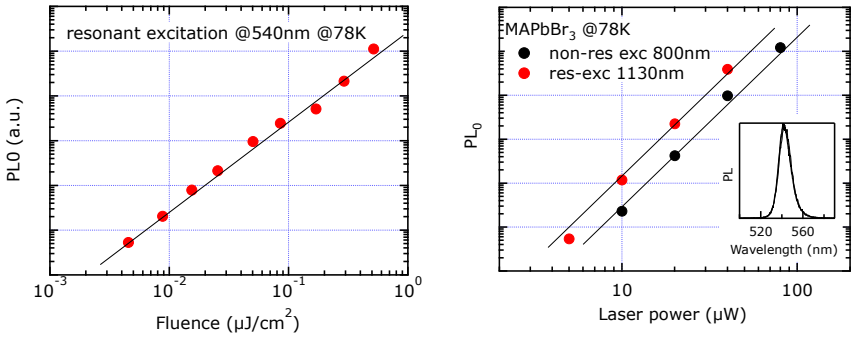

Figure A.6 Resonant excitation. Left Panel. PL_0 signal for $MAPbBr_3$ at low temperature under laser excitation resonant with the PL emission. Only PL emission in the low-energy tail, outside of the laser bandwidth was considered. Diffused laser light was rejected with a beam block and a polarizer. Even though resonant excitation is supposed to inject bound excitons, the quadratic dependence of PL_0 on laser fluence demonstrates (the black line represents, as a guide for the eye, a quadratic power law dependence) that excitons are ionized in favor of free carriers within the time resolution of the apparatus (40ps). Right Panel: Two-photon excitation. PL_0 signal for $MAPbBr_3$ at low temperature under two-photon laser excitation, that allows clear comparison between non-resonant excitation of free carriers and resonant creation of excitons without stray laser light entering the detection apparatus. In both cases the PL_0 signal appears to be proportional to the fourth power (black lines) of the laser fluence, meaning that is quadratic in the injected density of excitations, as expected for free carriers.

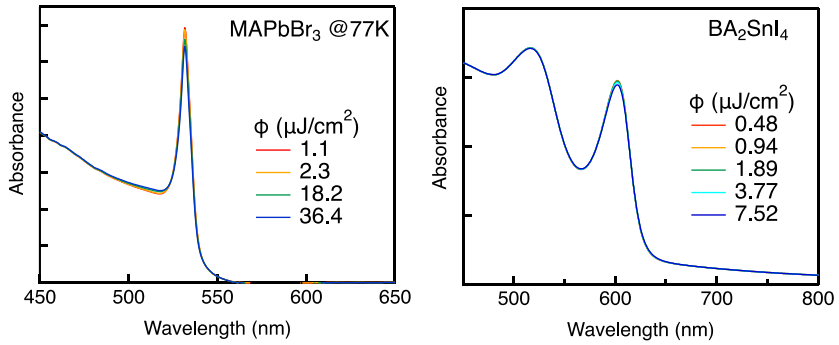

Figure A.7 Excitonic absorption. Absorption spectra of $MAPbBr_3$ (low temperature, left panel) and BA_2SnI_4 (right panel) under pulsed excitations demonstrate the persistence of the exciton peak up to the highest measured fluences. Spectra were obtained adding the differential absorption from DT measurements to the linear absorption coefficient from UV-Vis spectrometer.

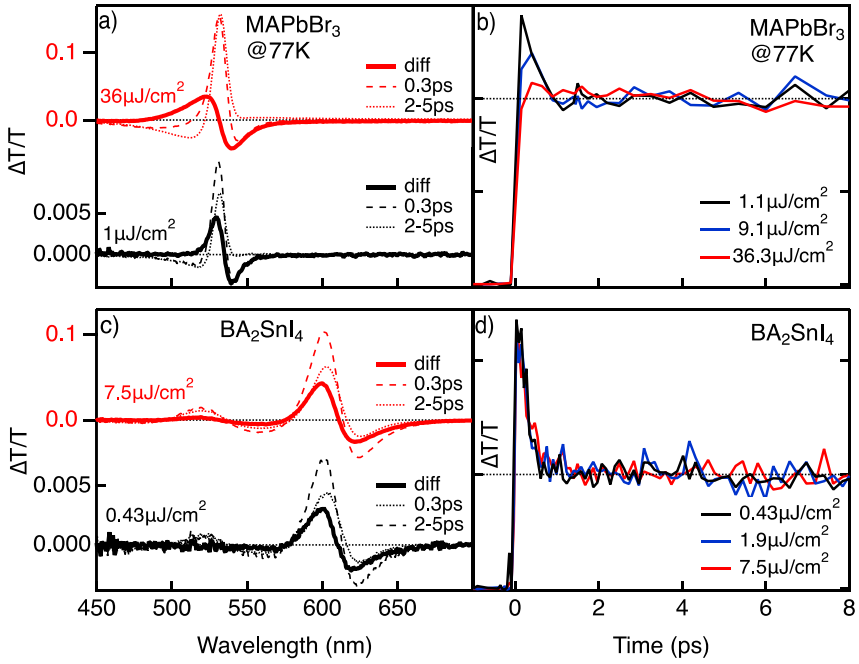

Figure A.8 Polaron formation and size. a) and c) Dashed and dotted lines are DT spectra acquired for $MAPbBr_3$ and BA_2SnI_4 at two different delays and two different laser fluences, as marked. The solid lines are differences among the spectra at earlier and later times. b) and d) are the corresponding time traces for DT measurements at three different laser fluences.

$MAPbI_3$		$MAPbBr_3$		$MAPbBr_3$@77K		BA_2SnI_4		BA_2PbI_4	
Φ(μJ/cm²)	n(cm⁻³)	Φ(μJ/cm²)	n(cm⁻³)	Φ(μJ/cm²)	n(cm⁻³)	Φ(μJ/cm²)	n(cm⁻²)	Φ(μJ/cm²)	n(cm⁻²)
0.19	$2.84\ 10^{16}$	0.75	$7.83\ 10^{16}$	0.45	$7.09\ 10^{16}$	0.4	$6.81\ 10^{9}$	1.50	$2.93\ 10^{10}$
0.38	$5.68\ 10^{16}$	1.50	$1.57\ 10^{17}$	0.98	$1.54\ 10^{17}$	0.94	$1.35\ 10^{10}$	3.01	$5.86\ 10^{10}$
0.75	$1.14\ 10^{17}$	2.63	$2.74\ 10^{17}$	1.88	$2.96\ 10^{17}$	1.88	$2.70\ 10^{10}$	5.27	$1.03\ 10^{11}$
1.50	$2.27\ 10^{17}$	3.76	$3.9\ 10^{17}$	3.76	$5.91\ 10^{17}$	3.76	$5.40\ 10^{10}$	11.28	$2.20\ 10^{11}$
2.82	$4.26\ 10^{17}$	7.52	$7.83\ 10^{17}$	7.52	$1.18\ 10^{18}$	7.52	$1.08\ 10^{11}$	18.81	$3.66\ 10^{11}$
5.64	$8.52\ 10^{17}$	15.04	$1.57\ 10^{18}$	15.04	$2.36\ 10^{18}$			30.09	$5.86\ 10^{11}$
11.28	$1.70\ 10^{18}$	30.09	$3.13\ 10^{18}$					52.66	$1.03\ 10^{12}$

Table A.1 Excitation densities on the various samples corresponding to the applied laser pulse fluence.

3D HPs	**T (K)**	$k_{1,p}$ **(s^{-1})**	$k_{2,p}$ **(cm^3s^{-1})**	$k_{3,p}$ **(cm^6s^{-1})**
$MAPbI_3$	R.T.	$(1.6 \pm 0.1) \times 10^8$	$(1.2 \pm 0.1) \times 10^{-10}$	$(3.3 \pm 0.2) \times 10^{-28}$
$MA_{1-x-y}FA_xCs_yPbI_{3-z}Br_z$	R.T.	$(1.6 \pm 0.1) \times 10^8$	$(1.2 \pm 0.1) \times 10^{-10}$	$(3.3 \pm 0.2) \times 10^{-28}$
$MAPbBr_3$	R.T.	$(4.3 \pm 2) \times 10^7$	$(4.4 \pm 0.6) \times 10^{-10}$	$(2.0 \pm 0.3) \times 10^{-28}$
$MAPbBr_3$	77	$(2.7 \pm 0.5) \times 10^8$	$(3.8 \pm 1.7) \times 10^{-10}$	$(1.2 \pm 0.8) \times 10^{-28}$
2D HPs	**T (K)**	$k_{1,p}$ **(s^{-1})**	$k_{2,p}$ **(cm^2s^{-1})**	$k_{3,p}$ **(cm^4s^{-1})**
BA_2SnI_4	R.T.	$10^7 \div 10^8$	$(7 \pm 4) \times 10^{-3}$	$(2.6 \pm 0.4) \times 10^{-13}$
BA_2PbI_4	R.T.	$(1.0 \pm 0.2) \times 10^9$	$(9 \pm 0.2) \times 10^{-3}$	$(2.1 \pm 0.2) \times 10^{-14}$

Table A.2 Fit Parameters. $k_{1,p}$, $k_{2,p}$ and $k_{3,p}$ are the first, second and third order constants in the rate equation 2 (main text) for the polaron population n_p. We performed a global fit to the DT transients and a polynomial fit to the $\dot{n}_p$ (proportional to $\frac{\dot{\Delta T}}{T}$) versus n (proportional to $\frac{\Delta T}{T}$) data. Fits to each DT transient were performed only in the time window for which the polaron decay is assumed to be intrinsic, i.e., excluding the decay at long times for which the chemical equilibrium condition, $PL \propto \left(\frac{\Delta T}{T}\right)^2$, is not fulfilled anymore. Values in the table are a weighted average of the results obtained through the two methods.

Chapter 3

Direct measurement of radiative decay rates in metal halide perovskites

The rate of light emission per unit carrier concentration, or radiative rate, is a fundamental semiconductor parameter that determines the limit photoconversion efficiency of solar cells. In hybrid perovskites, optical emission results from a bimolecular process, so that the radiative rate depends on the carrier density and cannot be directly measured with standard techniques. Instead, it is estimated either from UV-Vis absorption or from the kinetics of photoexcitation decays in time-resolved spectroscopy experiments. In this work, an ultrafast radiometric experiment is introduced to directly assess the radiative decay rate in perovskites thin films through a calibrated measurement of the instantaneous photoluminescence flux under pulsed laser excitation. The measured radiative decay rate is found to be significantly lower than the second order decay constant determined from photoluminescence decay kinetics, contrary to what often assumed; it is also 50-100 times slower than estimates for a plasma of free excitons and free charged carriers, obtained from absorption coefficients through optical reciprocity relations. We attribute the microscopic origin of the measured low radiative rate to the formation of a population of dark excitations, specifically large polarons. Our results provide a coherent framework to rationalize radiative and non-radiative carrier recombination processes in metal halide perovskites, as well as the photophysical basis to optimize device performances for this emerging class of semiconductors.

This chapter is based on the publication:
*A. Simbula, **R. Pau**, F. Liu, L. Wu, S. Lai, A. Geddo-Lehmann, A. Filippetti, M.A. Loi, D. Marongiu, F. Quochi, M. Saba, A. Mura and G. Bongiovanni, Energy Environ. Sci., **2022**, 15, 1211*

Contribution to the work: samples preparation, calibrated photoluminescence apparatus set up and corresponding measurements.

3.1 Introduction

Performances of semiconductor-based optoelectronic devices depend critically on their radiative emission efficiency. While the connection is apparent for light-emitting devices, it holds for solar cells as well, since pure radiative recombination is needed to approach the Shockley-Queisser limit for photoconversion efficiency.[1–4] The goal in solar cell optimization is to reduce unwanted, non-radiative decay rates below the benchmark set by the radiative rate, so that their effects on solar cell efficiency are negligeable. The progress towards the radiative limit has been rapid in solar cells based on hybrid lead-halide perovskites, where in a few years voltage losses due to non-radiative decay have been reduced to the level of the best silicon solar cells.[5–7] However, the actual values of radiative decay rates in perovskites are currently not agreed upon. The catch with perovskite solar cells is that radiative recombination is a bimolecular process whose rate increases proportionally to the carrier concentration. In turn, carrier concentration under continuous-wave (CW) excitation is determined by the balance between generation and recombination rates, so that a CW measurement alone cannot access the radiative recombination rate because carrier concentration is unknown. To supplement CW measurements, ultrafast time-resolved photoluminescence (TRPL) is typically employed to measure real time decay rates for photoexcitations created by ultrafast laser pulses; radiative and non-radiative decay rates are then estimated by fitting the photoluminescence time traces with a rate equation model, also known as the ABC model, that includes a monomolecular term (A), usually attributed to traps, a bimolecular term (B), assumed as radiative recombination, and a trimolecular term (C), due to Auger recombination.[8–11] Such time-domain determination of radiative recombination rates is however based on the unproven assumption that, since radiative recombination is a bimolecular recombination process between two free carriers, then all bimolecular recombination in perovskites is radiative, even though some studies have suggested otherwise.[12–16] Restricting the field to methylammonium lead halide $CH_3NH_3PbI_3$ (MAPI), the prototype of perovskites successfully employed in solar cells, analyses based on rate equations produced a wide variety of results for the bimolecular radiative recombination rate coefficients, within the range $2 \times 10^{-11} \div 2 \times 10^{-8} cm^3 s^{-1}$.[17–25] Such a wide spread cannot be attributed to variations in the oscillator strength of optical transitions, given that measurements for the absorption

coefficient at the exciton peak, which results from the inverse process of optical emission,[26,27] are for MAPI consistently reported within a much narrower interval, around $3 \times 10^4 \mathrm{cm}^{-1}$.[21,27–32] This inconsistency has been tentatively attributed to either extrinsic effects, like spatial diffusion and vertical inhomogeneity of charge carriers,[19,20,33,34] or to intrinsic effects that breach the symmetry between absorption and emission, like Rashba effect or the formation of large polarons.[13,35–41] It appears therefore of paramount importance to establish a reliable value for the radiative recombination rate.
The aim of this work is to provide an experimental technique to directly access the radiative recombination rate by measuring at the same time the absolute photon emission flux and the carrier density. In the setup proposed here, ultrafast laser excitation creates a known density of photoexcitations, while the instantaneous absolute flux of photons emitted per unit time is measured with a radiometrically calibrated streak camera set-up. The technique has been applied to a variety of hybrid perovskite compounds of interest for optoelectronics, both with iodine and bromine as halide anions. The values obtained for the radiative recombination rates are at least one order of magnitude lower than the bimolecular decay rates measured from photoluminescence time traces, and up to two orders of magnitude lower than the radiative rates estimated from optical absorption under the assumption of a population of free electrons, holes, and excitons. Such results are interpreted as evidence for the presence of dark photoexcitations, namely the formation of large polarons.

3.2 Results

3.2.1 Direct measurement of the radiative decay rates

Direct measurement of the radiative bimolecular recombination constant requires absolute measurements of both the carrier density n and the emitted radiance. When a semiconductor thin film is optically excited above the gap with laser pulses much shorter than the carrier recombination time, the optically injected carrier density, $n(t = 0) = n_0$, can be estimated accurately from the pulse photon fluence times the absorptance, divided by the film thickness. The ensuing instantaneous photoluminescence (PL) emitted over a time interval much shorter than the carrier lifetime, namely $PL(t = 0) = PL_0$, represents the external light radiance emitted perpendicularly to the films surface, produced by the carrier density n_0. The goal of our experiment is to

measure the absolute PL_0 value through a calibrated streak camera spectrometer. A sketch of the experimental setup used for the determination of absolute PL emission is shown in the upper panel of Fig. 3.1. Optical excitation was provided by a wavelength-tuneable regenerative amplifier laser source delivering 100-fs long pulses at 1KHz repetition rate. A portion of photoluminescence emitted perpendicularly to the sample surface in the backward direction, collected over a small solid angle, is focused onto the entrance slit of a spectrometer coupled to a 2D streak camera. The image of the excitation spot is shown in the left inset of Fig. 3.1(a), where the small green rectangle, much smaller than the laser spot, represents the intersection of the spectrometer vertical entrance slit with the horizontal streak camera slit, highlighting that the probed PL comes from a homogeneously excited region on the in-plane sample surface. The streak camera response was calibrated by directing a laser pulse of known fluence through the same setup through which PL is collected, yielding the detection quantum yield as the ratio between streak camera counts to incident photons; the absolute calibration was repeated at all wavelengths of interest. More details about the calibration procedure can be found in Experimental section.

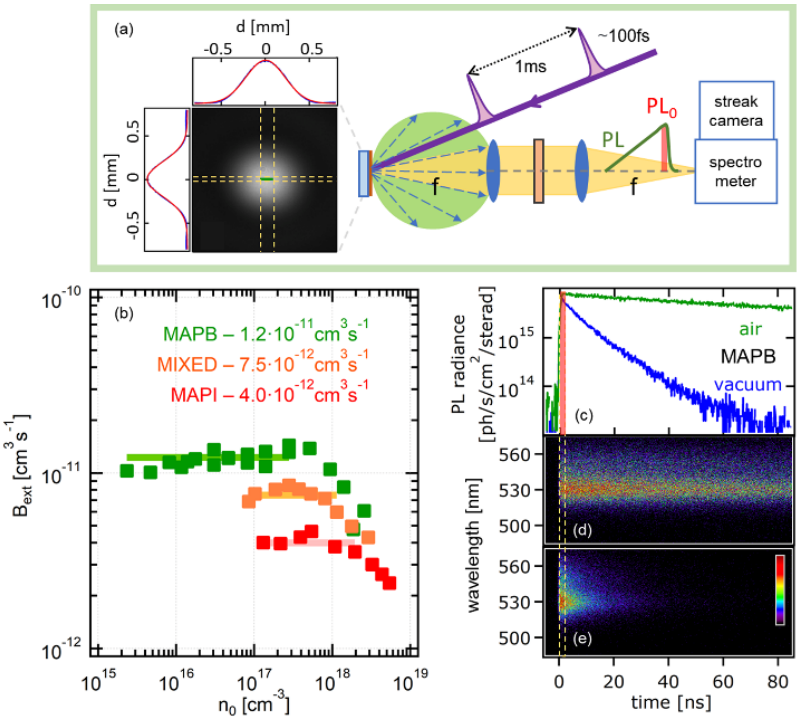

Figure 3.1 (a) Sketch of the experimental setup for the measurement of the absolute time resolved PL radiance, with a pulsed source exciting the front side of the sample and a portion (in yellow) of the PL emission being collected and focused on the entrance slit of the time-resolving detection system. Light emission is assumed to follow a Lambertian angular dispersion as represented by the green lobe in front of the sample surface. Inset on the left is an image of the excitation spot in the plane of the sample, with horizontal and vertical profiles fitted by gaussian functions. Here the small homogeneously pumped region probed in the measurement is represented by the green rectangle resulting from the intersection of the images of the spectrometer and streak camera entrance slits. In order to ensure vertically-homogeneous excitation, the pump laser wavelength was 630 nm for MAPI and mixed perovskite films, 430 nm for MAPB. Graph (b): values of B_{ext} obtained from absolute $t = 0$ radiance (PL_0) as a function of the injected carried density n_0 for MAPB (green), mixed perovskite (orange), and MAPI (red), with thick lines representing the best fit with a linear function and resulting in the average values reported on top of the graph, excluding the data at high injected carrier density, where Auger effect becomes dominant. PL measurements in the lower carrier density regime for MAPI and MIXED were not accessible due to lower emission efficiency of the samples. On the right side: (c) absolute PL radiance time profiles obtained from spectrograms (d) and (e) measured in the same MAPB sample inside a vacuum chamber, with (d) recorded at atmospheric pressure, and (e) measured at low pressure, temporarily recovering the behaviour previous to photohealing. The two decay profiles in (c) have the same PL_0 but very different photoluminescence decay times

We investigated three different lead iodide and bromide perovskites, that will be referred to as MAPB ($CH_3NH_3PbBr_3$), MAPI ($CH_3NH_3PbI_3$) and mixed perovskite ($(CH_3NH_3)_{1-x-y}(CH(NH_2)_2)_xCs_yPbI_{3-z}Br_z$), a mixed-cation, mixed-halide variant that is successfully applied in solar cells.[17] All samples were thin films, spin-coated on glass and covered with a protective poly (methyl methacrylate) (PMMA) layer. The film thickness was around 100 nm, comparable to the penetration depth of light at the excitation wavelength, resulting in minimal spatial inhomogeneities in the carrier density across the sample depth (see Fig. B.1). The angular dispersion of the emission is assumed to be Lambertian, namely with intensity proportional to $cos\theta$, where θ is the angle between the normal to the surface and the photon direction, as schematically represented by the green lobe in Fig. 3.1 (a). Only the light emitted within a small solid angle along the backward direction perpendicular to the film surface is detected, highlighted as the yellow cone in Fig. 3.1 (a).

A set of absolute TRPL measurements as a function of the injected carrier density n_0 was performed for each sample under study. We then considered $r_{ext,0}$, *i.e.*, the total number of photons emitted per unit time and unit film volume which eventually escape the film from both the front and back film surfaces after multiple emission and absorption processes. We obtain $r_{ext,0} = (2\pi/d)PL_0$, where d is the film thickness and 2π accounts for the effective emission solid angle of the two emitting surfaces under the assumption of a Lambertian angular dispersion. The validity of this latter hypothesis was confirmed by photoluminescence measurements in an integrating sphere, whose results will be discussed in the next paragraph. By exploiting the relation between $r_{ext,0}$ and the injected carrier density n_0,

$$B_{ext} = r_{ext,0}/n_0^2, \quad (1)$$

we could determine the external radiative bimolecular recombination constant B_{ext}. The results are reported in Fig. 3.1(b), where the quadratic dependence of $r_{ext,0}$ from n_0 is confirmed by B_{ext} being approximately constant over a wide range of excitation densities, with deviations at higher densities due to saturation effects. The average B_{ext} values are reported on top of the graph. The fact that B_{ext} does not depend on the excitation fluence also demonstrates that the residual background doping is negligeable with respect to the injected carrier concentrations, even at the lowest fluences we have explored.

In Fig. 3.1(d-e) are shown two PL spectrograms of a MAPB film: spectrogram (d) was recorded in a vacuum chamber filled with air after

a prolonged film illumination at atmospheric pressure, while (e) was taken holding the sample at low pressure. Photo-healing increases PL decay times up to more than 100 ns, while lifetime is reverted to less than 10ns when the sample is kept in vacuum. This increased non-radiative lifetime is a well-known phenomenon, resulting in an increase in the time-integrated PL and consequently in the photoluminescence quantum yield (QY).[42–46] The radiometric measurements demonstrates that the absolute radiance at $t = 0$ (PL_0), which is proportional to B_{ext}, is actually not affected by photohealing, showing no evident correlation between the radiative recombination rate constant derived from equation (1) and the characteristic time of the PL decay. To exclude possible ultrafast decays of the excited population, also femtosecond differential transmission measurements have been performed on the MAPB film kept in vacuum, as reported in Fig. B.2.

B_{ext} also depends on film interfaces, which can be suitably designed to enhance the fraction of light emitted externally, as is often done in light emitting devices. The intrinsic recombination constant of the material is $B_{\text{int}} = r_{\text{int},0}/n_0^2$, where $r_{\text{int},0}$ is the spontaneous photon emission rate per unit of volume inside the bulk material. In the limit of isotropic internal light emission, $r_{\text{int},0}$ can be estimated from the knowledge of PL_0 alone, namely the external light radiance emitted perpendicularly to the film surface, whose value would not be affected by the angular dispersion possibly deviating from a Lambertian pattern. In the limit of very thin layers, B_{int} reads:

$$B_{\text{int}} \approx \frac{4\pi\tilde{n}_{\text{film}}^2}{1-R}\frac{PL_0}{d\,n_0^2} \quad (2)$$

where $\tilde{n}_{\text{film}}$ represents the film refractive index, R the sample reflectance at the PL emission wavelength. According to our definition of B_{ext}, it can be shown that $B_{\text{int}} = 2\tilde{n}_{\text{film}}^2/(1-R)\,B_{\text{ext}}$. We refer to section B.3 in Appendix for a detailed analysis of the thermodynamic equations connecting B_{int} to PL_0 and B_{ext}. The values of B_{int} and B_{ext} are reported in Tables 3.1 and 3.2.

	B_{ext} ($cm^{-3}s^{-1}$)	k_2 ($cm^{-3}s^{-1}$)
MAPB	$1.1 \cdot 10^{-11}$	$1.1 \cdot 10^{-10}$
MAPI	$4.0 \cdot 10^{-12}$	$2.7 \cdot 10^{-10}$
MIXED MAPI	$7.5 \cdot 10^{-12}$	$1.6 \cdot 10^{-10}$

Table 3.1: Radiative and non-radiative bimolecular decay rate constants. External radiative bimolecular recombination constant B_ext is obtained by applying equation (1) to experimental data reported in Fig. 3.1(b). The second order rate constant k_2 is obtained from the global fit of PL decays, represented with blue squares in Fig. 3.2 (d-f).

	B_{int} ($cm^{-3}s^{-1}$)	
	Measured from PL	**Calculated from abs**
MAPB	$1.8\ 10^{-10}$	$1.5\ 10^{-8}$
MAPI	$6.3\ 10^{-11}$	$2.2\ 10^{-9}$

Table 3.2: Internal radiative decay rates from PL and from absorption. Values for the internal bimolecular radiative recombination rate coefficient B_{int} derived from the calibrated measurement of the PL radiance through equation (2), or estimated from the absorption coefficient through the generalized Planck law, using equations (6) and (7), with effective masses $m_e = 0.22\, m_0$, $m_h = 0.23\, m_0$ for electron and hole respectively in MAPI[27] and $m_e = 0.277\, m_0$, $m_h = 0.245\, m_0$ in MAPB[56] (see S9, ESI†). The bandgaps extracted from absorption through Elliott formula are $E_g = 1.648\, eV$ for MAPI and $E_g = 2.40\, eV$ for MAPB.

3.2.2 Radiative and non-radiative bimolecular decays

To determine the nature of the processes governing the carrier recombination kinetics in our films, we first analysed the temporal PL decays at different excitation fluences. In Fig. 3.2 (a-c) Markov plots are shown,[13] obtained by shifting each PL transient along the time axis until it overlaps with the decay curve corresponding to the next higher fluence. In each of the investigated films of MAPI, mixed perovskite and MAPB, the resulting PL transients merge with each other, identifying a single decay curve extending over more than six orders of magnitude in the PL instantaneous intensity. The existence of a single decay curve for each sample implies that, at any time after excitation, the PL radiance does not depend on the previous history of the excited state, but only on the instantaneous value of the carrier density n, the key feature defining a Markov process.

The Markovian nature of the decay allows us to neglect contributions of non-Markovian kinetics in the analysis of the PL transients, such as excitation-induced saturation of electronic traps, which would introduce trapped populations as further excited-state parameter, or the kinetics of carrier diffusion, which would require the introduction of a spatial population profile spreading over time.[12]
The charge carrier concentration n being the only relevant parameter, the transient PL decay could be modelled by solving
the standard ABC rate equations, with three elementary processes, related to monomolecular (rate constant k_1), bimolecular (rate constant k_2) and trimolecular Auger recombination (rate constant k_3):

$$\frac{dn}{dt} = -k_1 n - k_2 n^2 - k_3 n^3. \quad (3)$$

A global fit was then performed on all the PL time profiles recorded for each sample. The squares of the solutions for the rate equations $n^2(t) \propto PL(t)$, reported as solid black curves in Fig. 3.2 (a-c), reproduce the Markov recombination curve with remarkable accuracy in all the three perovskite films, across six orders of magnitude in photoluminescence signal amplitude and five decades in time span (30 ps to 3ms). Such an agreement ensures us that the rate coefficients are not depending on the carrier density, otherwise the ABC model would not be able to provide a global fit.
The three processes contribute differently to the total decay rate, with the third order k_3 term being the dominant one in the first few tens of ps after excitation at the highest fluence, then the bimolecular $k_2 n$ rate taking over for several hundreds of picoseconds, and finally, when the density n is substantially reduced, the monomolecular trapping rate causing the long mono-exponential decay, that may extend for over a microsecond. The one-to-one correspondence between the carrier density n and time t allows to invert the solution of rate equations and plot the decay rate (*i.e.*, the inverse of the decay time), namely $(-dn/dt)/n$, as a function of the density n, as shown in the insets of Fig. 3.2 (a-c). The slope in log-log scale directly indicates the leading recombination order, 1 at low densities, increasing to 2 and then 3 at higher carrier densities.
The main takeaway from the rate equation analysis, shown in Fig. 3.2 (d-f), is that the value of the bimolecular k_2 constant extracted from the PL dynamics is much higher than the value of the radiative constant B_{ext}. In other words, we find a dominant contribution to k_2 that comes

from non-radiative bimolecular annihilation processes, which is not affecting B_{ext}.

Our conclusion is strengthened by comparing the results obtained before and after photo-healing of the MAPB film (crossed squares in Fig. 3.2(d)): we found a reduction by a factor ~7 of k_2 with respect to the value before treatment, without any concomitant change in the radiative decay constant B_{ext}, whose value is indistinguishable before and after photo-healing.

A non-radiative contribution to k_2 requires going beyond a conventional annihilation process of the electron-hole pair, in which the energy of the couple is transferred to the photon, according to the scheme $e + h \longrightarrow \hbar\omega$. One possibility is non-radiative recombination of free carriers through shallow traps, i.e. traps with energy depth smaller than the energy difference between the band edge and the quasi-Fermi level. In such a case, the trap-assisted recombination would still be bimolecular, because the trapped carrier population is in equilibrium with the free carrier population. Another mechanism could be trap-mediated Auger recombination, which involves two free charges and one trapped.[47] An alternative explanation has been recently proposed, which is peculiar of metal halide perovskites and naturally results from considering that the excited state contains both charged carriers and neutral bright excitons, the former constituting the majority population and the latter the minority one.[13]

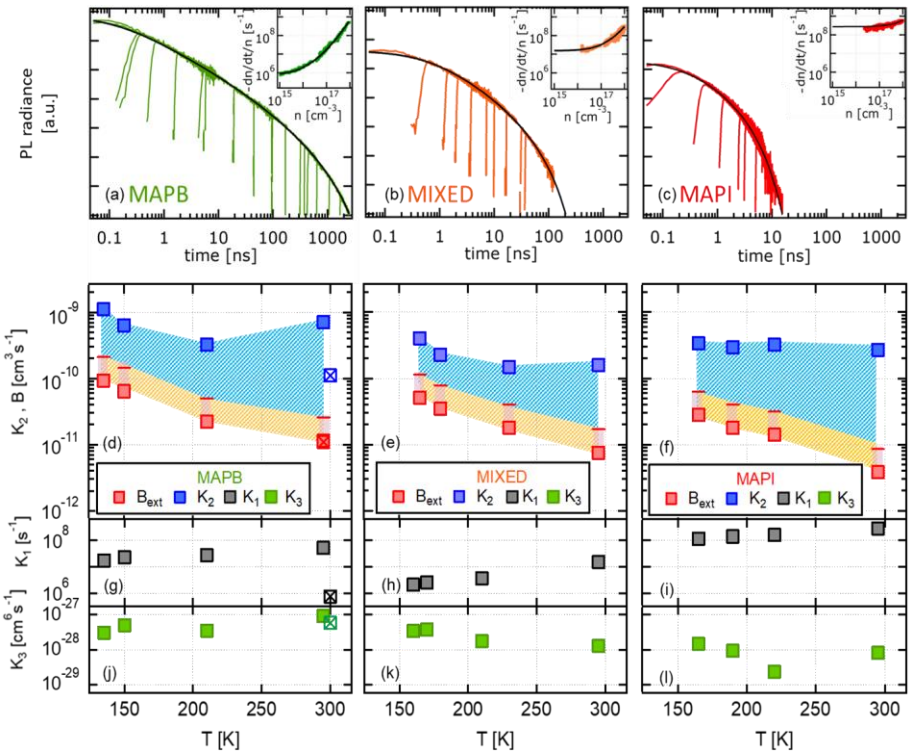

Figure 3.2 Upper panel (a-c): Markov plot of the PL time decays in log-log scale, obtained shifting the initial time of each decay to match the PL radiance curves at higher excitations. Black curves represent the result of the global fit with an ordinary differential equation with a common set of k_1, k_2 and k_3 coefficients for all the decay profiles of the same sample. The insets in the upper right corner of each graph show the decay rate (the inverse of the decay time) versus the injected carrier density in log-log scale: experimental data are reported as coloured dots, while the black curve represents the fitted decay equation. Lower panel: Comparison between B_{ext} and k_2 at different temperatures in the range 130K - 300K for MAPB (d), mixed perovskite (e) and MAPI (f). The values of B_{ext}, obtained from absolute PL_0 radiances, are represented with red squares, while horizontal red segments represent the highest achievable B_{ext}, under the assumption that all the light waveguided along the film plane ultimately leaves the sample. The range of B_{ext} values resulting from only a partial extraction of the waveguided light is represented by the yellow areas. The global fit coefficients k_1, k_2 and k_3 are reported in graphs (g-i), (d-f) and (j-l) respectively, with the light-blue region in (d-f) highlighting the difference between maximum B_{ext} and k_2 for the same set of measurements. In (d) we report with crossed squares the results for MAPB after photo-healing treatment, with the values of B_{ext} before and after photo-healing not distinguishable since overlapped.

Since all decay rate constants are known to depend on temperature, our analysis was extended from 300K down to 130K (see Fig. B.4 and B.5). Fig. 3.2 (d-l) show the best values of k_1, k_2 and k_3 coefficients resulting from the global fits. The values of k_2 (blue squares) are to be compared with the values of B_{ext} (red squares) extracted from absolute PL radiances coming from the same sets of measurements, whose room-temperature values are reported in Table 3.1.

At all temperatures and for all the samples under analysis the second order recombination constant k_2 is much higher than B_{ext}. The horizontal segments above the red squares represent the maximum values of B_{ext} that can be achieved depending on the extraction efficiency of photons generated inside the film, that can be up to $\tilde{n}_{\text{cap}}^2$ times higher, with $\tilde{n}_{\text{cap}}$ the refractive index of the capping layer on top of the surface (see Fig. 3.3(b) and Fig. B.6 for more details). The possible range of values that can be taken by B_{ext} is represented by the vertical pink bars in Fig. 3.2 (d-f), with interpolated regions depicted as yellow shaded areas. It is evident that, even accounting for different photon extraction efficiencies, the discrepancy between B_{ext} and the corresponding k_2 can exceed one order of magnitude even at low temperatures, as highlighted also by the blue-shaded regions in Fig. 3.2 (d-f).

Fig. 3.3 (a) reports the QY measured under pulsed excitation, where QY data (empty squares) are obtained by integrating over time the transient PL radiance, divided by the injected carrier density n_0 and multiplied by 2π to account for the overall emission form the front and back film surfaces. As an independent validation, we measured the QY of the MAPB sample with an integrating-sphere PL set-up (Fig. 3.3 (b)), under the same pulsed excitation as in the absolute radiance measurements. The results, represented by black squares in Fig. 3.3 (a), are consistent with those obtained in the radiometric time-resolved PL setup assuming a Lambertian angular dispersion of light emission (see B6 Appendix, for integrating sphere measurements and the contribution to the external PLQY by light propagating along the film plane).

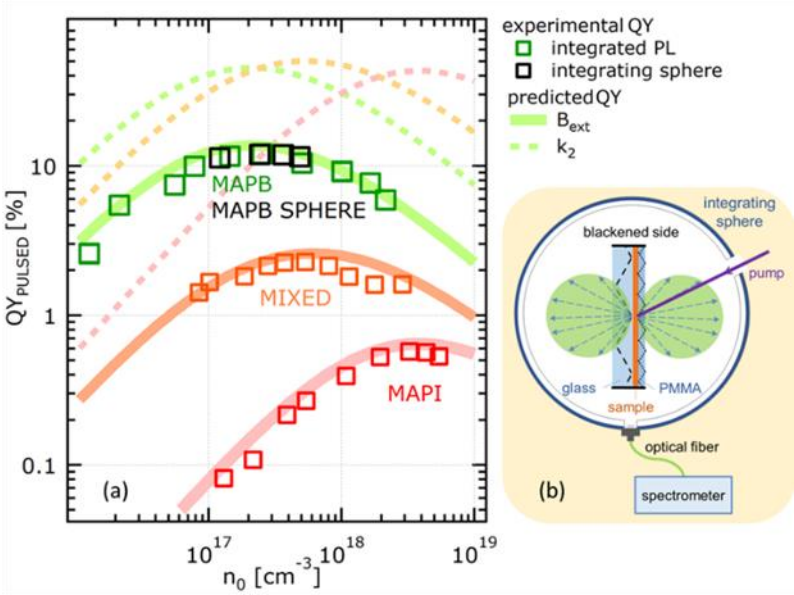

Figure 3.3 (a) QY measured under pulsed excitation as a function of injected carrier density n_0 at room temperature. Green, orange, and red squares are estimated from the time-integral of calibrated radiance measurements of MAPB, mixed perovskite and MAPI, respectively. Black squares show the results of measurements on MAPB using the setup sketched in inset (b), keeping the sample under the same pulsed excitation inside an integrating sphere to collect emission (sizes are not to scale for sake of clarity). The edges of the glass were blackened to block the light propagating in the plane of the glass or PMMA. Emission from MAPI and mixed perovskite samples was so feeble that could not be measured with the integrating sphere, due to a limitation in the maximum exposure time. In (a) solid lines are representing the QY versus n_0 computed as explained in the main text, considering B_{ext} as the radiative decay rate, while dashed lines represent the values of QY if considering k_2 in place of Bext.

The solid curves in Fig. 3.3(a) represent the QY estimated as $QY = (1/n_0)\int_0^\infty B_{\text{ext}}\, n^2(t)\, dt$. The instantaneous carrier density $n(t)$ was calculated from the rate equation (3) with the initial condition $n(0) = n_0$, using the decay rate constants k_i from the global fit analysis. Looking at the QY trend versus n_0 in Fig. 3.3(a), a bell-shape can be recognised, with the QY being limited by the monomolecular trapping process at lower excitation fluences, and by Auger recombination at higher fluences. In Fig. 3.3 (a), we also show the QY (dashed lines) calculated as $(1/n_0)\int_0^\infty k_2 n^2(t)\, dt$, i.e., assuming that all bimolecular decays are radiative. The resulting QY largely exceed the experimental one, confirming that $k_2 \gg B_{ext}$.

3.2.3 Reciprocity law between light emission and absorption

The analysis performed so far on different perovskite films does not require any assumption on the nature of the light-emitting species. In this section, the absorptance and photoluminescence spectra of perovskite films are analysed to identify which are the excitations responsible of photon emission and their contributions. The starting point of our analysis, based on the reciprocity between photon absorption and emission (in the non-quantum-degenerate Boltzmann limit), is the Planck law for a black body, generalized by Würfel to extend its validity to semiconductors:[48]

$$r_{\hbar\omega,\mathrm{ext}} = \frac{2\pi\, e^{\frac{\mu}{kT}}}{4\pi^3\hbar^3 c_0^2 d}\, a(\hbar\omega)[\hbar\omega]^2 e^{-\frac{\hbar\omega}{kT}} \quad (4)$$

$$r_{\hbar\omega,\mathrm{int}} = \frac{4\pi\, e^{\frac{\mu}{kT}}}{4\pi^3\hbar^3 c_0^2}\, n_r^2(\hbar\omega)\alpha(\hbar\omega)[\hbar\omega]^2 e^{-\frac{\hbar\omega}{kT}}. \quad (5)$$

Here $r_{\hbar\omega,\mathrm{ext}}$ and $r_{\hbar\omega,\mathrm{int}}$ are the external and internal spontaneous photon emission rate per unit of photon energy $\hbar\omega$ and of film volume. In the above relations $a(\hbar\omega)$ is the film absorptance, $\alpha(\hbar\omega)$ the absorption coefficient, $\tilde{n}_r(\hbar\omega)$ the real index of refraction and μ the chemical potential of the electron and hole pairs, namely the split of the quasi Fermi level. If electronic excitations are only created by thermal energy, $\mu = 0$ holds and eq. (5) recovers the Van Roosbroeck–Shockley relation, which simply states that, according to the principle of detailed balance, the spontaneous photon emission rate equates the absorption rate of thermal radiation at any given photon energy.[49] This reciprocity law is widely used to estimate the radiative limit of the open circuit voltage of a solar cell,[50,51] and specifically of perovskite-based photovoltaic devices.[52] Since $a(\hbar\omega)$ and $\alpha(\hbar\omega)$ were measured in a spectrophotometer, as described in Experimental section, the integration of equations (4) and (5) allows us to determine the overall external and internal thermal emissions, respectively. The factor 2 in the numerator of (4) is due to the contributions coming both from back and front surface (more details on the derivation can be found in B3, Appendix). We used these equations to infer the internal radiative bimolecular recombination constant B_{int}, and to distinguish the contributions resulting from the decay of excitons and of free electron-hole pairs.

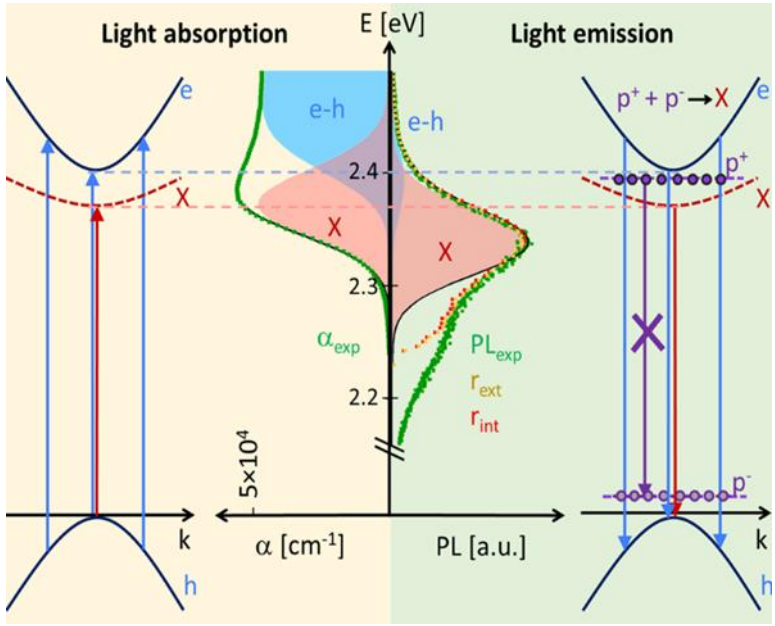

Figure 3.4: Sketches of light absorption (left) and emission (right) processes, with black and dashed red curves representing electron-hole and exciton bands, respectively; purple circles on the right represent polaronic states. Graphs in the centre compare experimental and theoretical absorption coefficient a and PL spectra for MAPB film. Left graph: theoretical absorption coefficient (black) resulting from the contributions of exciton (pink filling) and valence-to conduction band transitions (light blue filling), in good agreement with experimental absorption coefficient spectrum (green trace). Right graph: experimental PL spectrum (PL_{exp}, green) compared with the external r_{ext} (yellow) and internal r_{int} (red) luminescence estimated, respectively, from absorptance and absorption spectra through the generalized Planck laws. As the investigated film was very thin, the spectral shapes of r_{ext} and r_{int} are indistinguishable. The close correspondence between PL_{exp} and r_{ext} confirms that the same states are involved in absorption and emission processes. PL spectrum estimated from theoretical absorption coefficient through the same generalized Planck law is represented in black, with exciton and band-to-band contributions also shown as pink and light blue filled areas, respectively.

We first checked whether the generalized Planck law (4) reproduced the spectrum of spontaneous emission in our films, focusing on the experimental data of MAPB, whose absorption spectrum features a pronounced contribution from excitonic transitions as can be seen in

Fig. 3.4 (the same analysis for MAPI is reported in B7, Appendix). The central graph in Fig. 3.4 shows a good agreement between the measured PL spectrum PL_{exp} (green) and the spectrum obtained by applying equation (4), r_{ex} (yellow). The low-energy shoulder in the experimental PL spectrum is also reproduced, indicating that it may be arising from ground-state defects. This positive check ensures us that the same states and transitions are involved in photon absorption and emission.
As a second step, the absorption coefficient was fitted with Elliott's law for excitonic band-edge absorption to disentangle excitonic transitions from band-to-band ones (see discussion in B8, Appendix). Once the two absorption contributions were fixed, we calculated the overall internal emission $r_{\hbar\omega,\mathrm{int}}$ and the contributions resulting from exciton and unbound electron-hole pair recombination. As shown in Fig. 3.4, most photons are emitted following exciton annihilation.
We may now estimate the predicted recombination rate as:

$$B_{\mathrm{int}} = \frac{\int_0^{\infty} r_{\mathrm{sp,int}} d(\hbar\omega)}{n_{\mathrm{th}}^2}, \quad (6)$$

i.e., by integrating equation (5) and dividing it by the square of the thermal population:

$$n_{\mathrm{th}} \sim 2(2\pi mkT/h^2)^{3/2} e^{-E_{\mathrm{g}}/2kT}, \quad (7)$$

where m is the effective mass of photoexcitations and E_g the energy gap (see discussion B9, Appendix, for more details on the calculation of B_{int} and n_{th}). The resulting values are reported in Table 3.2: the value predicted from absorption with the described calculation turned out to be 80 times larger than the experimental value of B_{int}, directly measured from PL without any assumption on the nature of the excited state population. Similar results were also found for MAPI (Table 3.2). Our result considering the free-carrier contribution only to B_{int}, as assessed from the Van Roosbroeck–Shockley relation, is in good agreement with values reported in literature.[21,27] Yet, the approximation of neglecting the radiative recombination of excitons is not justified in the light of the previous discussion (see Fig. 3.4).

3.3 Discussion

3.3.1 Rigid-lattice assumption versus polaron formation

The excited-state picture emerging from our set of optical measurements in MAPI and MAPB is characterized by: *i)* a sharp absorption edge and an excitonic spectral feature with absorption coefficient in excess of $10^4\ \mathrm{cm}^{-1}$; *ii)* spontaneous light emission resulting from the same optical transitions involved in the absorption spectrum; *iii)* a quadratic dependence of the PL intensity on the density of photoexcitations, and most important *iv)* a bimolecular recombination of carriers mostly nonradiative in nature, with a radiative rate ~80 (in MAPB) and ~40 (in MAPI) times smaller than those expected for a population of excitons and free carriers.

At first sight, point *ii)* and *iii)* could appear in contrast with the monomolecular radiative decay of excitons.[21] Yet, as discussed in reference [13], the quadratic dependence of the PL intensity can be naturally explained by assuming that charged carriers represent the majority population, while excitons are minority bright species, formed following bimolecular pairing of charges with opposite sign (see Fig. 4a in reference [13] for a scheme of decay processes). On one side the generalized Planck law in hybrid perovskites accurately reproduces the emission spectrum, on the other hand the measured B_{int} is much lower than the value expected from the optical emission of excitons and free electron-hole pairs, the excited species created upon absorption. A re-examination of the evaluation of B_{int} is therefore warranted, particularly of the charged carrier effective masses and bandgap energies employed to calculate the value of the thermal population n_{th}.

There exists a growing body of experimental evidence in literature indicating that the perovskite lattice relaxes around electrons and holes to form large charged polarons.[53–55] Lattice reorganization in the excited state to form charged polarons shifts the chemical equilibrium between excitons and charged carriers towards these latter. In other words, the presence of polarons reduces the concentration of light-emitting excitons, being polarons heavier and closer in energy to excitons with respect to lattice-unrelaxed charges. As a result, a thermal population constituted by polarons is considerably larger than what obtained under rigid lattice assumption.

A simple estimate based on the Feynman polaron model gives a thermal population enhancement factor of 58.5 for MAPI (details of the calculation are in Appendix B10), not far from the factor 40 suppression in the radiative coefficient reported in Table 3.2.

The physics of electron and hole polarons in hybrid perovskites was recently simulated through advanced ab initio molecular dynamics,[40] where it was found that the spatial overlapping between electrons and holes in MAPI is reduced by about two-orders of magnitude following lattice relaxation. The degree of overlap determines the rate at which polarons of opposite sign pair to form bright excitons.
The results of these simulations appear therefore consistent with our experimental results, the bimolecular radiative decay constant B_{int} being in MAPI (MAPB) 40 (80) times smaller than estimates under the assumption of no lattice deformation in the excited state.

3.3.2 Effects on the prediction of solar cell performances

The competition between radiative and nonradiative bimolecular recombination plays a key role in determining the photoconversion efficiency of perovskite solar cells and is central for approaching the Shockley-Quessier limit. The maximum open circuit voltage can be achieved in the pure radiative limit, and depends on the ratio between the injection rate of electron-hole pairs due to absorption of solar and thermal radiation.[52] As such, the radiative limit efficiency is independent of the actual radiative decay rate. Conversely, every drop of a factor 10 in the QY leads to an additional 60 meV voltage loss. For this reason, the very low radiative recombination rate of hybrid perovskites necessarily requires an even slower nonradiative decay to maximize the QY.
Fig. 3.5 illustrates the expected quantitative effects of photohealing of the the MAPB film on the CW emission quantum yield (QY_{cw}) under steady-state excitation with sunlight, i.e., how close a solar cell based on such materials may operate to the radiative limit. The rate equation is solved by equating the total decay rate $k_1 n + k_2 n^2 + k_3 n^3$ to the carrier generation rate $G = \int_0^\infty I \frac{\mathrm{S}(\hbar\omega)}{\hbar\omega} \alpha(\hbar\omega) d(\hbar\omega)$ due to the absorption of sunlight ($\mathrm{S}(\hbar\omega)$ is the AM 1.5G spectrum, 100mW/cm^2, and I is the applied sunlight intensity measured in suns) by the MAPB film with absorption coefficient $\alpha(\hbar\omega)$. Once the carrier density $n(I)$ is obtained as a function of the applied light intensity, $QY_{\mathrm{cw}} = B_{\mathrm{ext}} n^2 / (k_1 n + k_2 n^2 + k_3 n^3)$ is obtained as the ratio between radiative and total decay rates. In the MAPB films we studied, light irradiation under atmospheric pressure reduced the monomolecular decay constant k_1 by a factor ~70, and the second order one, k_2, by a factor

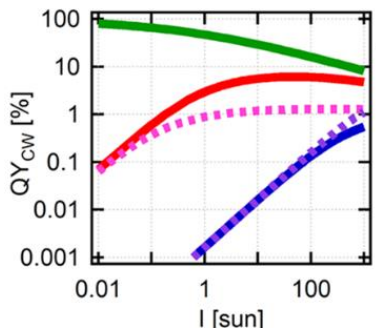

	$k_1(s^{-1})$	$k_2(cm^3s^{-1})$
Only Auger	0	0
k_1 k_2 healed	8×10^5	1×10^{-10}
k_1 healed	8×10^5	7×10^{-10}
k_2 healed	5×10^7	1×10^{-10}
not healed	5×10^7	7×10^{-10}

Figure 3.5 Expected quantum yield under continuous wave excitation (QY_{CW}) versus the intensity of the applied sunlight, distinguishing different scenarios where $k_1$and k_2 are affected or not by photohealing. The corresponding values of $k_1$and k_2 are reported in the table on the right, for each QY_{CW} curve. The blue solid curve (not healed) represents the QY_{CW} obtained with values of k_1 and k_2 from the fit of MAPB PL decay without photo-healing. The red curve is obtained considering the values of k_1 and k_2 after photo-healing. Pink and purple dashed curves are hypothetical results that would be obtained if photo-healing was affecting only k_1 or k_2, respectively. Green solid line finally represents the ideal case in which both k_1 and k_2 are negligible, and Auger recombination is considered as the only intrinsic effect.

~ 7, as reported in the table on the right side of Fig. 3.5. The solid blue curve is calculated with the values of k_1 and k_2 of MAPB film before photo-healing, while the red one is obtained from the values of k_1 and k_2 reduced due to photo-healing. The dashed pink and purple curves are calculated considering the effect of photo-healing on k_1 or k_2 only, respectively. From this projection, it is evident that the increase in QY_{cw} following photo-healing is resulting from the synergy between both contributions of k_1 and k_2, the decrease of the monomolecular decay rate being not sufficient to explain the total improvement in QY_{cw}. The green line in Fig. 3.5 also shows the highest QY_{cw} that could be obtained if Auger recombination, assumed as intrinsic, would be the only nonradiative decay channel. This analysis points to the fact that small k_1 values in high quality samples allow the build-up of a large carrier density, which however in turn enhances the contribution of the bimolecular nonradiative decays. The contribution of k_2 to the overall non-radiative decay rate under 1 sun illumination may therefore become important, even the dominant one, and needs to be dealt with to approach the radiative Shockley-Quessier limit. To create the range of injected carrier densities considered in this work under cw

illumination, intensities significantly greater than 1 sun are needed, causing significant temperature variations in perovskite films and sample instabilities; for such reasons calculations in Fig. 3.5 could not be supported with experimental data.

3.4 Conclusions

In this work we determined the radiative recombination rates in 3D hybrid perovskite thin films by setting up a radiometric time-resolved PL measurement. The measured radiative recombination constants are much lower than the ones estimated from the absorption spectrum through the Van Roosbroeck–Shockley relation under the assumption that only excitons and free carriers are present, pointing to the existence of a majority population of dark excitations, possibly large polarons. The bimolecular radiative decay constant B_{ext} is also substantially smaller than the second order constant k_2 obtained from the PL decay dynamics, demonstrating that bimolecular decay in hybrid perovskites is mostly non-radiative and extrinsic in nature. Photo-healing is found to reduce the second order nonradiative decay channel (k_2) in addition to the first order one (k_1). The findings reported here impose stringent limits on improving the open circuit voltage and efficiency of solar cells, since unwanted, non-radiative decay rates need to be suppressed much further than previously thought.

3.5 Experimental

3.5.1 Samples preparation

All the film depositions were performed inside a nitrogen-filled glove box. Bromide, Iodide and mixed I-Br perovskite thin films were fabricated by one-pot, two-steps and antisolvent spin coating deposition, respectively.
The $CH_3NH_3PbBr_3$ (MAPB) solution was prepared by dissolving MABr+$PbAc_2$*$3H_2O$ with a molar ratio 3:1 in dimethylformamide (DMF) and a final concentration of 0.5 M. The films were deposited on a glass slide at 6000 rpm for 60 s and annealed at 100°C for 5 minutes. The $CH_3NH_3PbI_3$ (MAPI) film was prepared by spinning a 0.5 M PbI_2 solution in DMF on a glass slide at 6000 rpm for 30 s followed by annealing at 80°C for 10 min. Then some drops of MAI dissolved in

isopropanol (10 mg/ml) were cast on the film and left it react for 2 minutes before the spinning. The MAPI film was annealed at 100°C for 30 min and then washed with isopropanol with a subsequent annealing at 100°C for 1 h.
The $MA_{1-x-y}FA_xCs_yPbI_{3-z}Br_z$ perovskite film was prepared with a 0.3 M precursor solution of FAI, MABr, CsI, PbI_2 and $PbBr_2$ with final stoichiometry $Cs_{0.05}FA_{0.81}MA_{0.14}PbI_{2.55}Br_{0.45}$ in a mixed solvent of DMF and dimethyl sulfoxide (DMSO) with a volume ratio of 4:1. The spin coating procedure in this case is assisted by an antisolvent: first, two drops of solution were spun at 2000 rpm for 10 s with an acceleration of 200 rpm/s, then at 4000 rpm for 20 s with an acceleration of 1000 rpm/s. Ten seconds before the end of the whole spinning cycle, 100 µL of chlorobenzene were dropped on the substrate. The substrate was then thermally treated at 100 °C on a hotplate for 10 min.
After the annealing, all the films were coated with a layer of PMMA dissolved in chlorobenzene.

3.5.2 Calibrated time-resolved PL measurements

Our ultrafast pulsed laser source was a Ti:sapphire regenerative amplifier (Coherent Libra) delivering 100-fs long pulses at 794 nm, with energy up to 4mJ and 1KHz repetition rate. The frequency conversion of the pulses was obtained with an optical parametric amplifier (TOPAS 800 from Light Conversion) equipped with nonlinear crystals, providing the excitation wavelength of 430nm for MAPB and 630nm for MAPI and mixed MAPI. Time-resolved detection system was constituted of a grating spectrometer (Acton 2300i) coupled to a streak camera (Hamamatsu C10910). In the low-temperature measurements the sample was kept inside a cryostat (Janis ST-500). Images of the laser spot in the plane of the sample were detected with a visible camera (Thorlabs DCC1545M).
The calibration procedure to obtain the absolute intensity of the PL signal was based on the determination of quantum efficiency of the spectrometer and streak camera detection system, i.e., by measuring the signal generated by laser pulses of known intensity under the very same operating conditions and streak camera settings used for the PL. The ultrafast pulsed laser source (Coherent Libra + TOPAS) was set at the wavelength range of the PL emission (530 nm for MAPB, 760 nm for MAPI and mixed perovskite) and was first measured with a power meter - photodiode system (PD300R-UV by Ophir Photonics). The laser pulses were then attenuated with calibrated neutral optical densities filters (the actual OD value for each filter when illuminated by

femtosecond laser pulses was measured) and sent into to the streak camera, keeping both horizontal and vertical slits wide open, so that all the incoming power was collected. Comparing the spectrally and time integrated counts per frame with the injected number of photons per pulse we could determine the quantum efficiency in the spectral region of the PL emission, i.e., $QE = 2.8 \cdot 10^{-3}\ counts\ /photon$ at 530nm and $QE = 3.3 \cdot 10^{-4}\ counts\ /photon$ at 760nm. To independently check the wavelength dependence of the calibration, the relative response was tested in the spectral region of interest using a radiometric calibrated lamp (Ocean Optics HL-3P-Cal) as source.
To evaluate the fraction of collected emission with respect to the Lambertian PL emitted from the surface, we fixed the solid angle of collection of the PL by placing an iris after the PL collection lens. By varying the iris aperture radius, the detected signal was verified to scale linearly with the collection solid angle.

3.5.3 Absorptance measurements

Optical absorption spectra of thin films in the UV-vis range was measured with a dual-beam spectrophotometer equipped with an integrating sphere accessory (Agilent Technologies Cary 5000 UV– vis–NIR) in order to avoid losses due to diffused transmission and reflection, collected with an hemispherical configuration.[57]

3.5.4 Integrating sphere measurements

Reflection/Transmission integrating sphere (LabSphere) with 6-inches diameter connected via an optical fiber to high resolution spectrometer (Photon Control SPM-002-ET64).

3.6 References

[1] J.-P. Correa-Baena, M. Saliba, T. Buonassisi, M. Grätzel, A. Abate, W. Tress and A. Hagfeldt, *Science* **2017**, *358*, 739–744.

[2] J. Chen and N. G. Park, *Adv. Mater.* **2019**, *31*, 1–56.

[3] N. G. Park and H. Segawa, *ACS Photonics* **2018**, *5*, 2970–2977.

[4] D. Luo, R. Su, W. Zhang, Q. Gong and R. Zhu, *Nat. Rev. Mater.* **2020**, *5*, 44–60.

[5] M. Green, E. Dunlop, J. Hohl-Ebinger, M. Yoshita, N. Kopidakis and X. Hao, *Prog. Photovoltaics Res. Appl.* **2021**, *29*, 3–15.

[6] K. A. Bush, A. F. Palmstrom, Z. J. Yu, M. Boccard, R. Cheacharoen, J. P. Mailoa, D. P. McMeekin, R. L. Z. Hoye, C. D. Bailie, T. Leijtens, I. M. Peters, M. C. Minichetti, N. Rolston, R. Prasanna, S. Sofia, D. Harwood, W. Ma, F. Moghadam, H. J. Snaith, T. Buonassisi, Z. C. Holman, S. F. Bent and M. D. McGehee, *Nat. Energy* **2017**, *2*, 1–7.

[7] J. Peng, D. Walter, Y. Ren, M. Tebyetekerwa, Y. Wu, T. Duong, Q. Lin, J. Li, T. Lu, M. A. Mahmud, O. L. C. Lem, S. Zhao, W. Liu, Y. Liu, H. Shen, L. Li, F. Kremer, H. T. Nguyen, D. Y. Choi, K. J. Weber, K. R. Catchpole and T. P. White, *Science* **2021**, *371*, 390–395.

[8] Y. C. Shen, G. O. Mueller, S. Watanabe, N. F. Gardner, A. Munkholm and M. R. Krames, *Appl. Phys. Lett.* **2007**, *91*, 144101.

[9] J. Cho, J. T. DuBose and P. V. Kamat, *J. Phys. Chem. Lett.* **2020**, *11*, 2570–2576.

[10] M. B. Johnston and L. M. Herz, *Acc. Chem. Res.* **2016**, *49*, 146-154.

[11] E. V. Peán, S. Dimitrov, C. S. De Castro and M. L. Davies, *Phys. Chem. Chem. Phys.* **2020**, *22*, 28345–28358.

[12] J. M. Richter, M. Abdi-Jalebi, A. Sadhanala, M. Tabachnyk, J. P. H. Rivett, L. M. Pazos-Outón, K. C. Gödel, M. Price, F. Deschler and R. H. Friend, *Nat. Commun.* **2016**, *7*, 13941.

[13] A. Simbula, R. Pau, Q. Wang, F. Liu, V. Sarritzu, S. Lai, M. Lodde, F. Mattana, G. Mula, A. Geddo Lehmann, I. D. Spanopoulos, M. G. Kanatzidis, D. Marongiu, F. Quochi, M.

Saba, A. Mura and G. Bongiovanni, *Adv. Opt. Mater.* **2021**, *9*, 2100295.

[14] A. Kiligaridis, P. A. Frantsuzov, A. Yangui, S. Seth, J. Li, Q. An, Y. Vaynzof and I. G. Scheblykin, *Nat. Commun.* **2021**, *12*, 3329.

[15] R. Brenes, D. Guo, A. Osherov, N. K. Noel, C. Eames, E. M. Hutter, S. K. Pathak, F. Niroui, R. H. Friend, M. S. Islam, H. J. Snaith, V. Bulovi, T. J. Savenije, S. D. Stranks, V. Bulović, T. J. Savenije and S. D. Stranks, *Joule* **2017**, *1*, 155–167.

[16] F. Staub, T. Kirchartz, K. Bittkau and U. Rau, *J. Phys. Chem. Lett.* **2017**, *8*, 5084–5090.

[17] D. Bi, W. Tress, M. I. Dar, P. Gao, J. Luo, C. Renevier, K. Schenk, A. Abate, F. Giordano, J. P. Correa Baena, J. D. Decoppet, S. M. Zakeeruddin, M. K. Nazeeruddin, M. Grätzel and A. Hagfeldt, *Sci. Adv.* **2016**, *2*, e1501170.

[18] Y. Yamada, T. Nakamura, M. Endo, A. Wakamiya and Y. Kanemitsu, *J. Am. Chem. Soc.* **2014**, *136*, 11610–11613.

[19] R. L. Milot, G. E. Eperon, H. J. Snaith, M. B. Johnston and L. M. Herz, *Adv. Funct. Mater.* **2015**, *25*, 6218–6227.

[20] A. R. Srimath Kandada, S. Neutzner, V. D'Innocenzo, F. Tassone, M. Gandini, Q. A. Akkerman, M. Prato, L. Manna, A. Petrozza and G. Lanzani, *J. Am. Chem. Soc.* **2016**, *138*, 13604–13611.

[21] M. Saba, M. Cadelano, D. Marongiu, F. Chen, V. Sarritzu, N. Sestu, C. Figus, M. Aresti, R. Piras, A. Geddo Lehmann, C. Cannas, A. Musinu, F. Quochi, A. Mura and G. Bongiovanni, *Nat. Commun.* **2014**, *5*, 5049.

[22] W. Rehman, R. L. Milot, G. E. Eperon, C. Wehrenfennig, J. L. Boland, H. J. Snaith, M. B. Johnston and L. M. Herz, *Adv. Mater.* **2015**, *27*, 7938–7944.

[23] C. Wehrenfennig, G. E. Eperon, M. B. Johnston, H. J. Snaith and L. M. Herz, *Adv. Mater.* **2014**, *26*, 1584–1589.

[24] V. D. Innocenzo, A. Ram, S. Kandada, M. De Bastiani, M. Gandini and A. Petrozza, *J. Am. Chem. Soc.* **2014**, *136*, 17730–17733.

[25] C. La-o-vorakiat, T. Salim, J. Kadro, M.-T. Khuc, R. Haselsberger, L. Cheng, H. Xia, G. G. Gurzadyan, H. Su, Y. M. Lam, R. A. Marcus, M.-E. Michel-Beyerle and E. E. M. Chia, *Nat. Commun.* **2015**, *6*, 7903.

[26] N. Sestu, M. Cadelano, V. Sarritzu, F. Chen, D. Marongiu, R. Piras, M. Mainas, F. Quochi, M. Saba, A. Mura and G. Bongiovanni, *J. Phys. Chem. Lett.* **2015**, *6*, 4566–4572.

[27] C. L. Davies, M. R. Filip, J. B. Patel, T. W. Crothers, C. Verdi, A. D. Wright, R. L. Milot, F. Giustino, M. B. Johnston and L. M. Herz, *Nat. Commun.* **2018**, *9*, 293.

[28] V. D'Innocenzo, G. Grancini, M. J. P. Alcocer, A. R. S. Kandada, S. D. Stranks, M. M. Lee, G. Lanzani, H. J. Snaith and A. Petrozza, *Nat. Commun.* **2014**, *5*, 3586.

[29] S. Sun, T. Salim, N. Mathews, M. Duchamp, C. Boothroyd, G. Xing, T. C. Sum and Y. M. Lam, *Energy Environ. Sci.* **2014**, *7*, 399–407.

[30] M. Habibi, F. Zabihi, M. R. Ahmadian-Yazdi and M. Eslamian, *Renew. Sustain. Energy Rev.* **2016**, *62*, 1012–1031.

[31] C. Tablero Crespo, *Sol. Energy Mater. Sol. Cells* **2019**, *195*, 269–273.

[32] G. Xing, N. Mathews, S. S. Lim, Y. M. Lam, S. Mhaisalkar and T. C. Sum, *Science* **2013**, *342*, 344–347.

[33] L. M. Herz, *ACS Energy Lett.* **2017**, *2*, 1539–1548.

[34] T. W. Crothers, R. L. Milot, J. B. Patel, E. S. Parrott, J. Schlipf, P. Müller-Buschbaum, M. B. Johnston and L. M. Herz, *Nano - Lett.* **2017**, *17*, 5782–5789.

[35] D. Meggiolaro, F. Ambrosio, E. Mosconi, A. Mahata and F. De Angelis, *Adv. Energy Mater.* **2019**, *10*, 1902748.

[36] M. J. Schilcher, P. J. Robinson, D. J. Abramovitch, L. Z. Tan, A. M. Rappe, D. R. Reichman and D. A. Egger, *ACS Energy Lett.* **2021**, *6*, 2162–2173.

[37] D. Ghosh, E. Welch, A. J. Neukirch, A. Zakhidov and S. Tretiak, *J. Phys. Chem. Lett.* **2020**, *11*, 3271–3286.

[38] M. Puppin, S. Polishchuk, N. Colonna, A. Crepaldi, D. N. Dirin, O. Nazarenko, R. De Gennaro, G. Gatti, S. Roth, T. Barillot, L. Poletto, R. P. Xian, L. Rettig, M. Wolf, R. Ernstorfer, M. V. Kovalenko, N. Marzari, M. Grioni and M. Chergui, *Phys. Rev. Lett.* **2020**, *124*, 206402.

[39] X. Y. Zhu and V. Podzorov, *J. Phys. Chem. Lett.* **2015**, *6*, 4758–4761.

[40] F. Ambrosio, J. Wiktor, F. De Angelis and A. Pasquarello, *Energy Environ. Sci.* **2018**, *11*, 101–105.

[41] A. Filippetti, C. Caddeo, P. Delugas and A. Mattoni, *J. Phys. Chem. C* **2016**, *120*, 28472–28479.

[42] S. G. Motti, M. Gandini, A. J. Barker, J. M. Ball, A. R. Srimath Kandada and A. Petrozza, *ACS Energy Lett.* **2016**, *1*, 726–730.

[43] D. W. Dequilettes, S. Koch, S. Burke, R. K. Paranji, A. J. Shropshire, M. E. Ziffer and D. S. Ginger, *ACS Energy Lett.* **2016**, *1*, 438–444.

[44] L. Huang, Z. Ge, X. Zhang and Y. Zhu, *J. Mater. Chem. A* **2021**, *9*, 4379–4414.

[45] J. S. W. Godding, A. J. Ramadan, Y. H. Lin, K. Schutt, H. J. Snaith and B. Wenger, *Joule* **2019**, *3*, 2716–2731.

[46] H. H. Fang, S. Adjokatse, H. Wei, J. Yang, G. R. Blake, J. Huang, J. Even and M. A. Loi, *Sci. Adv.* **2016**, *2*, 1–10.

[47] P. T. Landsberg, Recombination in Semiconductors, *Cambridge University Press* **2003**.

[48] P. Wurfel, *J. Phys. C Solid State Phys.* **1982**, *15*, 3967–3985.

[49] W. Van Roosbroeck and W. Shockley, *Phys. Rev.* **1954**, *94*, 1558–1560.

[50] T. Tiedje, E. Yablonovitch, G. D. Cody and B. G. Brookd, **2017** IEEE Trans. electron devices, 1984, ED-31, 711–716.

[51] U. Rau, Phys. Rev. B - Condens. Matter Mater. Phys., **2007**, *76*, 1–8.

[52] V. Sarritzu, N. Sestu, D. Marongiu, X. Chang, S. Masi, A. Rizzo, S. Colella, F. Quochi, M. Saba, A. Mura and G. Bongiovanni, *Sci. Rep.* **2017**, *7*, 44629.

[53] H. Tsai, R. Asadpour, J. C. Blancon, C. C. Stoumpos, O. Durand, J. W. Strzalka, B. Chen, R. Verduzco, P. M. Ajayan, S. Tretiak, J. Even, M. A. Alam, M. G. Kanatzidis, W. Nie and A. D. Mohite, *Science* **2018**, *360*, 67–70.

[54] B. Guzelturk, T. Winkler, T. W. J. Van de Goor, M. D. Smith, S. A. Bourelle, S. Feldmann, M. Trigo, S. W. Teitelbaum, H. G. Steinrück, G. A. de la Pena, R. Alonso-Mori, D. Zhu, T. Sato, H. I. Karunadasa, M. F. Toney, F. Deschler and A. M. Lindenberg, *Nat. Mater.* **2021**, *20*, 618–623.

[55] O. Cannelli, N. Colonna, M. Puppin, T. C. Rossi, D. Kinschel, L. M. D. Leroy, J. Löffler, J. M. Budarz, A. M. March, G. Doumy, A. Al Haddad, M. F. Tu, Y. Kumagai, D. Walko, G. Smolentsev,

F. Krieg, S. C. Boehme, M. V. Kovalenko, M. Chergui and G. F. Mancini, *J. Am. Chem. Soc.* **2021**, *143*, 9048–9059.

[56] T. Komesu, X. Huang, T. R. Paudel, Y. B. Losovyj, X. Zhang, E. F. Schwier, Y. Kojima, M. Zheng, H. Iwasawa, K. Shimada, M. I. Saidaminov, D. Shi, A. L. Abdelhady, O. M. Bakr, S. Dong, E. Y. Tsymbal and P. A. Dowben, *J. Phys. Chem. C* **2016**, *120*, 21710–21715.

[57] D. Marongiu, S. Lai, V. Sarritzu, E. Pinna, G. Mula, M. Laura Mercuri, M. Saba, F. Quochi, A. Mura, G. Bongiovanni, *ACS Appl. Mater. Interfaces* **2019**, *11*, 10021–10027.

Appendix B: Additional data to Chapter 3

B1: Light emitted from a thin film: the effect of vertical excitation inhomogeneity due to the finite light penetration depth

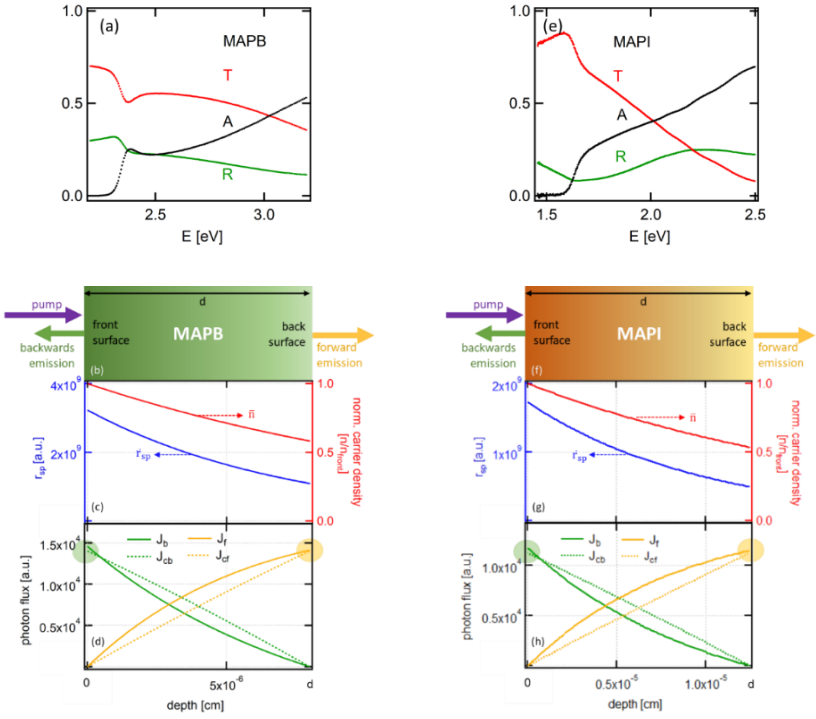

Figure B.1 Optical properties and scheme of the distribution of carrier density at different depths in the sample of MAPB (left) and MAPI (right)

We specifically consider two hybrid perovskite thin films: a MAPB film with thickness d=80 nm, excited by photons with energy $\hbar\omega_{ex} = 2.9$eV, emission occurs at the lower photon energy $\hbar\omega_{em} = 2.3$eV; a MAPI film with thickness d=125 nm, excited at energy $\hbar\omega_{ex} = 2.0$eV and with emission peaked at $\hbar\omega_{em} = 1.6$eV. The following considerations are referred both to MAPB, considering left graphs Fig. B.1 (a-d), and to MAPI, considering right graphs Fig. B.1(e-h).
The absorptance (A), reflectance (R) and transmittance (T) spectra are shown in Fig. B.1 (a,e). The absorption coefficient is then calculated as:

$$\alpha(\hbar\omega) = \frac{1}{d}\ln\frac{1-R(\hbar\omega)}{T(\hbar\omega)} \quad (B1.1)$$

The film absorptance at depth z (z<d), namely the fraction of the exciting light absorbed by the film at penetration depth z, is:

$$AA_{ex}(z) = [1-R(\hbar\omega_{ex})][1-e^{-\alpha(\hbar\omega_{ex})z}] \quad (B1.2)$$

The electron-hole pair density at z reads:

$$n(z) = \frac{dAA_{ex}(z)}{dz} \quad (B1.3)$$

Fig. B.1 (b,f) shows a sketch of the transversal section of the film with nuanced color: the darkest color at excited (front) surface stands for a higher carrier density with respect to that at the back surface. The vertical profile of the carrier density neglecting spatial diffusion (normalized to the value at the front surface n_{front}) is shown as a red curve in Fig. B.1 (c,g), a realistic approximation for pulsed excitation at t=0. The spatial profile of the spontaneous photon emission rate per unit of film volume, $r_{\mathrm{int}}(z)$, proportional to $n(z)^2$, is shown with the blue curve in Fig. B.1 (c,g). Despite the small thickness of the film, the light emission intensity at the front surface, $r_{\mathrm{int}}(0)$, is three times higher than the one close to the back surface $r_{\mathrm{int}}(d)$. The mean PL intensity, proportional to the square of the mean carrier concentration $\bar{n} = \frac{AA_{ex}(d)}{d}$, is the half of the value at the front surface $r_{\mathrm{int}}(0)$. Yet, we can show that the light emitted from the front or back surfaces, assuming a constant carrier density $\bar{n}$, is virtually equal to that emitted considering the effective spatial carrier profile. To estimate the photon flux through the front or back film surfaces, we need to sum up the light emitted at any point of the film and the absorption process photons undergo before being transmitted externally, according to the rate equation:

$$\frac{dJ(z)}{dz} = \delta r_{int}(z) - \alpha(\hbar\omega_{em})J(z) \quad (B1.4)$$

where $\delta r_{\mathrm{int}}(z)$ is the spontaneous photon emission rate per unit volume within a small solid angle around the direction z.
Fig. B.1 (d,h) shows the solutions of this differential equation for photons propagating in the forward (J_f) and backward (J_b) directions, while $J_{c,f}$ and $J_{c,b}$ correspond to the approximated case obtained with

constant carrier profile $\bar{n}$. The photon flux J_b and $J_{c,b}$ at the front surface (highlighted with green circle) and J_f and $J_{c,f}$ at the back surfaces (yellow circle) differ of just a few per cent, demonstrating that assuming a constant carrier density $\bar{n}$ is quite a reasonable approximation both for MAPI and MAPB thin films.

B2: Time resolution of PL measurements

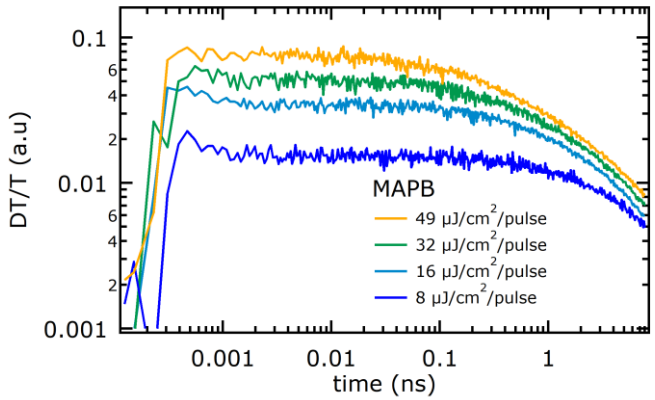

Figure B.2 Differential transmission measurement on MAPB thin film measured with femtosecond ultrafast transient absorption pump and probe technique, at different fluences in the same range of the TRPL measurements.

In order to exclude the presence of ultrafast features in the decay profile at t=0, that would be not detectable with the streak camera due to the time resolution (around 50ps), also differential transmission measurements were performed on the same samples, under the same pulsed optical excitation used to stimulate the photoluminescence. The DT/T signal was recorded with a differential transmission spectrometer (Helios from Ultrafast Systems), which measured individual probe and reference spectra with custom CMOS spectrometers, with a spectral resolution of 1nm and a time resolution up to 100fs, limited by the temporal length of the excitation pulses. In fig. B.2 we report result for MAPB (without photohealing) as a representative case: the decay profiles of the bleaching signal are clearly showing that there is no evidence of any sharp feature at t=0, i.e., when carriers are injected into the material, analogously to what already observed in the same kind of materials.[1,2]

B3: Evaluation of the internal and external light emission rates

The rate of light emitted perpendicularly to the front film surface per unit of film volume and solid angle is given by the Planck-Kirchhoff law, generalized by Würfel [3] to take into account the semiconductor electronic properties and optical excitations:

$$\delta r_{ext} = \frac{PL}{d} = e^{\frac{\mu}{kT}}\left[\frac{1}{4\pi^3\hbar^3c_0^2 d}\int_0^\infty a\,(\hbar\omega)^2 e^{\frac{-\hbar\omega}{kT}}\right] = \frac{B_{ext}}{2\pi}n^2 \qquad (B3.1)$$

PL is the external radiance emitted perpendicularly to the film surface, d the film thickness, a the absorptance and μ the chemical potential of electron-hole pairs. The right equation holds for a Lambertian emission. The factor of 2π accounts for the Lambertian emission angle from the front and back surfaces, each contributing with a factor π. Neglecting multiple reflections and in the limit of thin films, one can approximate $a \approx (1-R)(\alpha d)$, where R is the film reflectivity.
Light emission rate inside the semiconductor per unit of volume and solid angle reads:

$$\delta r_{int} = e^{\frac{\mu}{kT}}\left[\frac{1}{4\pi^3\hbar^3c_0^2}\int_0^\infty \tilde{n}^2\alpha(\hbar\omega)^2 e^{\frac{-\hbar\omega}{kT}}\right] = \frac{B_{int}}{4\pi}n^2 \quad (B3.2)$$

where $\tilde{n}$ is the film index of refraction. From which, one obtains:

$$B_{\text{int}} = \frac{4\pi\delta r_{int}}{n^2} = \frac{4\pi\int_0^\infty \tilde{n}^2\alpha(\hbar\omega)(\hbar\omega)^2 e^{\frac{-\hbar\omega}{kT}}}{n^2\,\frac{1}{d}\int_0^\infty a(\hbar\omega)(\hbar\omega)^2 e^{\frac{-\hbar\omega}{kT}}}\frac{PL}{d} \cong \frac{4\pi\,\tilde{n}^2}{(1-R)}\frac{PL}{d\,n^2} \quad (B3.3)$$

$$\frac{B_{int}}{B_{ext}} = 2\frac{\delta r_{int}}{\delta r_{ext}} = \frac{d\int_0^\infty \tilde{n}(\hbar\omega)^2\alpha(\hbar\omega)(\hbar\omega)^2 e^{\frac{-\hbar\omega}{kT}}}{\int_0^\infty a(\hbar\omega)(\hbar\omega)^2 e^{\frac{-\hbar\omega}{kT}}} \cong 2\frac{\tilde{n}(\hbar\omega_{PL})^2}{[1-R(\hbar\omega_{PL})]} \qquad (B3.4)$$

Where $\hbar\omega_{PL}$is the photon energy at the PL peak; $\tilde{n}(\hbar\omega_{PL}) = 2.25$ and 2.41 for bromide and iodide perovskite films, respectively.[4] We get $\frac{B_{int}}{B_{ext}} = 16.3$ (MAPB) and 15.9 (MAPI).
Our perovskite films are deposited on a glass substrate and overcoated with a PMMA layer. As shown in S5, PL is still provided by equation (S3.1), in which a and R are the absorptance and the reflectivity of the

whole structure, respectively. Differences between back and front reflectivity are neglected.

B4: Results of low-temperature measurements of B_{ext}

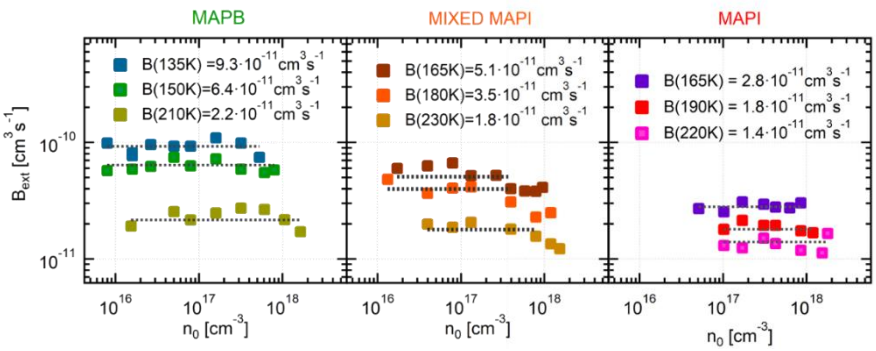

Figure B.4 Bext values obtained from absolute PL radiance measurements at low temperatures for the three different compounds, analogously to what reported in Fig.3.1 (b) in the main text. The B obtained from the fit are reported as red squares in Fig. 3.2 (d-f) and Table 3.1 in the main text.

B5: Results of low-temperature measurements of k_1, k_2 and k_3

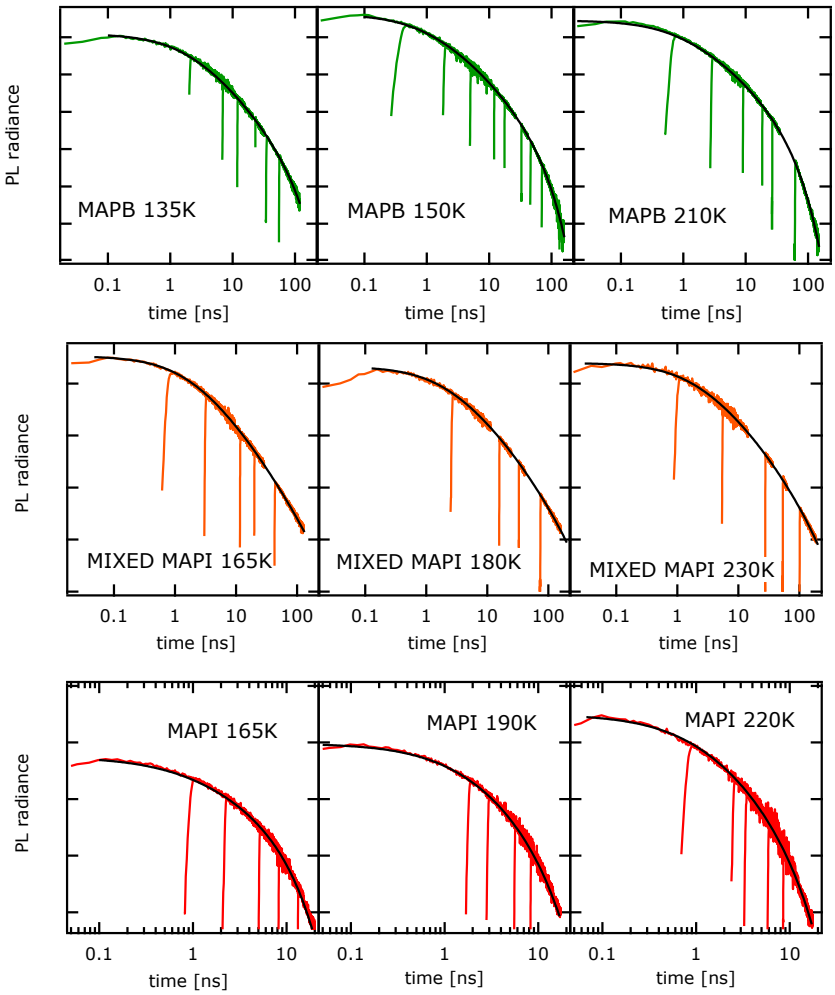

Figure B.5 Markovian plots with fits with rate equation as in Fig. 3.2(a-c) in the main text, at different low temperature values. k_1, k_2 and k_3 coefficients obtained from the global fits (black lines) with rate equation were reported as green, blue and black squares respectively in Fig. 3.2(d-f) in the main text.

B6: PLQY measurements with the integrating sphere and Lambertian emission

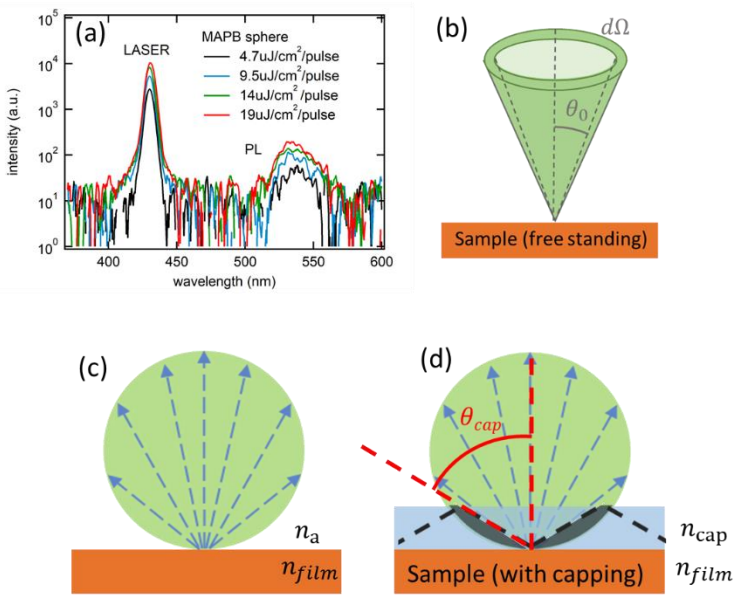

Figure B.6 (a) Measurements of PLQY performed on MAPB sample with the integrating sphere setup (Fig. 3.3b in the main text) under the same pulsed excitation as in the absolute radiance measurements. Each black square in Fig. 3.3a in the main text is the result of one of the above reported PLQY measurements. (b) Representation of emission from a free-standing film over a solid angle $d\Omega = 2\pi sin\theta_0 d\theta$ *and (c) the Lambertian emission resulting from the integral of* $d\Omega$ *over all the possible angles of emission from the front surface. (d) represents the case of a sample with capping, instead of free-standing one, where the portion of light emitted at solid angles with from a film with* $\theta > \theta_{cap}$ *is totally internal reflected at the capping-air interface. The length of the blue arrows in the Lambertian emission pattern is proportional to the photon emission rate, which is higher at small* θ_{cap} *and is not affected by the presence of the capping layer.*

In Fig. B.6(b), θ_0 represents the detection angle of the PL set-up. θ_0 being small, the effective Lambertian solid angle $\Delta\Omega_L$ is almost equal to the detection solid angle $\Delta\Omega_0$:

$$\Delta\Omega_0 = 2\pi \int_0^{\theta_0} sin\,\theta d\theta = 2\pi(1 - cos\theta_0) \approx \pi\theta_0^2 \quad (B6.1)$$

$$\Delta\Omega_L = 2\pi \int_0^{\theta_0} sin\,\theta \cos\theta\, d\theta = \pi\, sin^2\,\theta_0 \approx \pi\theta_0^2 \quad (B6.2)$$

The whole Lambertian solid angle from the front surface of a free-standing film (represented by the green lobe in Fig. B.6(c)) is equal to π. If we consider the emission from both the front and back surfaces, Ω_L=2 π.

In the presence of a capping dielectric layer (the glass substrate or the PMMA in our samples), a fraction of the light emitted from the surface will be totally internal reflected at the capping layer/air interface, as represented in Fig. B.6(c) with the grey coloured portion of the Lambertian lobe. The total internal reflection condition at the capping layer/air interface reads:

$$\sin\theta_{\text{cap}} = \frac{1}{n_{\text{cap}}} \quad (B6.3)$$

Only light emitted at angles $\theta < \theta_{\text{cap}}$ can exit from the surface of the capping layer (Fig. B.6(d)), within a solid angle $\Omega_{\text{cap,L}} = \pi\, sin^2\,\theta_{\text{cap}} = \pi/\, n_{\text{cap}}^2$ For the film architecture, perovskite/capping-layer/air, the expression of PL, after correction for the effective light speed in the dielectric layer, reads

$$PL \propto \Omega_{\text{cap,L}}/c^2 = \Omega_{\text{cap,L}} n_{\text{cap}}^2/c_0^2 = \pi/c_0^2 \quad (B6.4)$$

which is the same expression of PL for a free-standing film without any capping layer (Fig. B.6(c))., ensuring us that the radiance obtained from the absolute measurement is the same if we consider a free-standing film or one with capping.

For a fair comparison between the calibrated TRPL measurement and the one with the integrating sphere, we might consider that not all the light emitted by the perovskite layer into the capping-layer is transmitted externally through the capping-layer/air interface: in fact, this happens only to a fraction $1/n_{\text{cap}}^2$. The remaining fraction of light undergoes total internal reflection and is reflected back towards the film (see Fig. B.6(d)). In the case of very thin films with high internal PLQY, remission processes can largely compensate for absorption. The back-reflected light can therefore propagate along the plane of the capping layer and come out from its edges. Since this in-plane guided light is not contributing to the Lambertian emission from the front and back surfaces, for a fair comparison with the results of absolute radiance measurements, it had to be excluded from the measurement

in the integrating sphere: this was achieved by blackening the edge of the glass, resulting in a very good agreement between the two techniques. We also observed that, after blackening the edges, the PLQY measured inside the sphere diminished by a factor of ≈ 2, confirming that the overall extraction efficiency from a film on glass can exceed the free-standing one by a factor between 1 and n_{cap}^2~2.25, as also represented with the yellow areas in Fig. 3.2(d-f) in the main text.
Considering that in the integrated-sphere measurement the collected PL comes from the whole excitation spot, not only from the central-homogenously excited region as in the TRPL measurement, the injected carrier density had to be rescaled by a correction factor of ~ 2, estimated as the ratio between the peak power (at the centre of the spot) and the power averaged over the whole spot area.

B7: Experimental and theoretical absorption coefficient a and PL spectra for MAPI

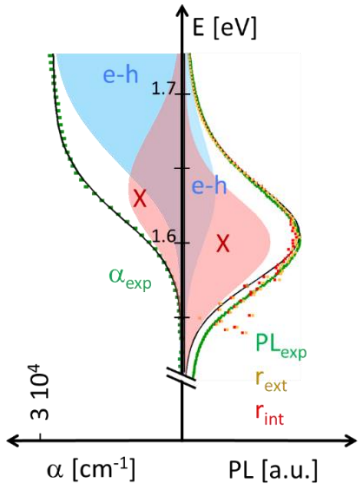

Figure B.7 Analogous of Fig. 3.4 in the main text, for MAPI film. Left side: theoretical absorption coefficient (continuous black curve) resulting from the contributions of exciton (pink) and valence-to conduction band transitions (light blue) according to Elliott equation (see also B8) , compared with experimental absorption coefficient spectrum (green dots). Right side: experimental PL spectrum (PL_{exp},continuous green curve) compared with the external r_{ext} (yellow dots) and internal r_{int} (red dots) luminescence estimated through the reciprocity relations from absorptance and absorption spectra,

respectively, black line is the PL obtained from theoretical absorption coefficient through reciprocity relations.

B8: Fits to the absorption coefficient by using the Elliott's law for excitonic band-edge absorption

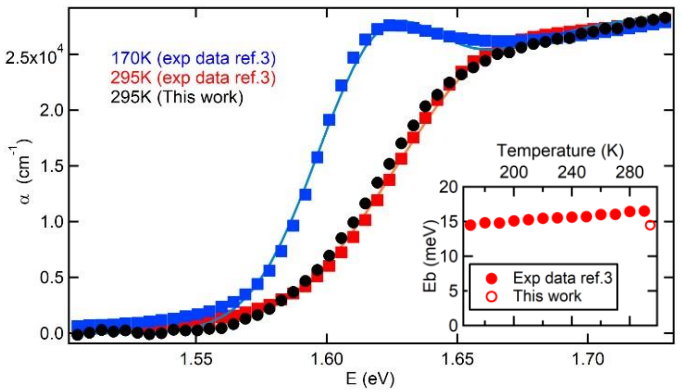

Figure B.8 Absorption coefficient spectra for MAPI at 295K for our samples, compared with data reported in Ref. [5] *for thin films of the same material at 295K (red) and 170K (blue): squares are experimental data, lines are best fits with Elliott function. Exciton binding energy as a function of temperature is reported in the inset, filled circles are experimental data from reference* [5]*, empty circle from the film measured in this work.*

We modelled the absorption coefficient above the optical absorption edge in the framework of the Elliott's theory of Wannier excitons, [6] as done also in Reference [7] :

$$\alpha(\hbar\omega) = C\,\frac{\mu_{cv}^2}{\hbar\omega}\left[\sum_n \frac{4\pi\sqrt{E_b^3}}{n^3}\,\delta\left(\hbar\omega - E_n^b\right) + \frac{2\pi\sqrt{E_b}\,\theta\left(\hbar\omega - E_g\right)}{1 - e^{-2\pi\sqrt{\frac{E_b}{\hbar\omega - E_g}}}}\right] \qquad (B8.1)$$

where μ_{cv} is the transition dipole moment; $\hbar\omega$ the photon energy, E_b the exciton binding energy and C is a constant. The first term in equation (B8.1) describes transitions to exciton states with energy $E_n^b = E_g - \frac{E_b}{n^2}$.

Transitions to continuum states with energies above the bandgap E_g are accounted for by the second term; $\delta(x)$ and $\theta(x)$ are the Dirac-delta and the unit step functions, respectively.
In order to avoid the introduction of nonlinear terms to account for non-parabolic dispersion of the conduction and valence bands, fits were restricted to 100 meV above the band-gap.[8] A gaussian line-broadening was assumed.
At room temperature, transition linewidths of MAPI are such that the excitonic peak is largely smeared out. To reduce the uncertainty in the evaluation of the exciton and band-gap energies, we performed a global fit to the MAPI absorption spectra in the tetragonal phase at different temperatures, down to T=170 K, as reported in Fig. B.8 . Absorption spectra vs temperature were taken from Reference [5]. We considered $C\mu_{cv}^2$ in equation (B7.1) as temperature independent in the tetragonal phase and took it as a global fit parameter. The estimated values of E_b vs T were found to be weakly dependent on temperature, in agreement with recent ab-initio theoretical calculations,[9] and with optical f-sum rule.[5]

B9: Evaluation of the radiative bimolecular recombination constant from the reciprocity law

The starting point for the evaluation of the radiative bimolecular recombination constant from the absorption/emission reciprocity is the equation:

$$B_{\text{int,rl}} = \frac{\int_0^\infty r_{\text{sp,int}} d(\hbar\omega)}{n_{\text{th}}^2} \qquad (B9.1)$$

The thermal population, n_{th}, should in principle accounts for both the majority population of electron-hole pairs (n_{eh}) and excitons (n_x). The equilibrium condition between these two species is provided by the Saha's law:

$$\frac{n_{eh}^2}{n_x} = \left(\frac{\mu_x k_B T}{2\pi\hbar^2}\right)^{\frac{3}{2}} e^{-\frac{E_B}{k_B T}} = n_{eq} \quad (B9.2)$$

where μ_X is the effective reduced mass of excitons. We took $\mu_X = 0.11\, m_0$ and $0.13\, m_0$ for MAPI and MAPB,[10] respectively, leading to $n_{eq} \sim 1 \div 2 \times 10^{16}$ cm^{-3} for both perovskites. Chemical equilibrium

implies that electron-hole pairs are the majority population up to $n_0 < n_{eq}$. As n_{th} is orders of magnitude lower than n_{eq}, we can safely approximate n_{th} by the free carrier population alone, which is given by the mass action law. n_{th}^2 can thus be calculated as:

$$n_{th}^2 \cong 4(2\pi m_e kT/h^2)^{3/2}(2\pi m_h kT/h^2)^{3/2} e^{-E_{\mathrm{g}}/kT} \quad (B9.3)$$

The electron and hole effective masses of MAPI were taken from reference [8] $m_e = 0.22\, m_0$ and $m_h = 0.23\, m_0$. The hole effective mass $m_h = 0.245\, m_0$ of MAPB was instead taken from reference [11]. The electron effective mass was then estimated from the knowledge of μ_X: $m_e = 0.277\, m_0$.

As the expression of n_{th} does not account for line broadening of the carrier electronic levels, $\int_0^\infty r_{\mathrm{sp,int}} d(\hbar\omega)$ was also estimated at the same level of approximation from equation 5 in the main text and (B8.1) for the unbroadened absorption coefficient. It is worth noting that inclusion of line broadening in the calculation of the numerator and denominator of eq. S9.1 leads to the same results, within the experimental uncertainty. As a matter of fact, line broadening leads to an increased value of $\int_0^\infty r_{\mathrm{sp,int}} d(\hbar\omega)$, which is however compensated by the higher value of n_{th}^2 when this latter is numerically calculated by also including line broadening.

B10: Polaron model description

The interaction strength between charge carriers and the surrounding polar optical phonon cloud is typically quantified by the adimensional Fröhlich coupling constant[12]:

$$\alpha = \frac{e^2}{4\pi\epsilon_0 \hbar c}\sqrt{\frac{m_{e,h}c^2}{2\hbar\omega_{LO}}}\left(\frac{1}{\varepsilon_\infty} - \frac{1}{\varepsilon_0}\right) \quad (B10.1)$$

Here ε_0 and ε_∞ are static and high-frequency dielectric constants, respectively, and ω_{LO} the dominant longitudinal optical phonon frequency in the temperature range of interest; in fact, for polar semiconductors, diffusive transport at room T is typically dominated by carrier scattering with polar optical phonons. For $\alpha << 1$ (*weak-coupling* regime), as in the case of covalent semiconductors, polarons do not form, and carriers move through the crystal as single particles

with effective mass $m_{e,h}$; for $\alpha \sim 1$ (*large-polaron* regime) carriers move while dragging a structural deformation extended for many lattice parameters around the carrier; from transport point of view, carriers can still be described as free particles, but with an enhanced (polaronic) effective mass. For strongly ionic materials, α can be much larger than unity; in this limit the electronic ground-state follows adiabatically the lattice deformation, and carriers become self-trapped within a radius of just a few lattice parameters (*small-polaron* regime). Using values appropriate for MAPI at room T (ε_0 = 60,[13] ε_∞ = 5,[14–17] $\hbar\omega_{LO}$ = 10 meV,[18,19] $m_{e,h} = 0.22\, m_0$) we obtain α = 3.02, which classifies MAPI as a material in the medium-large polaron regime. Our value is slightly larger than the α = 2.40-2.60 obtained by Frost,[19] mainly as a consequence of the use of calculated ε_0 = 24, which is much smaller than our adopted experimental ε_0. On the other hand, electron-phonon coupling calculations based on many-body perturbation theory obtain a much smaller α = 1.4.[20]

The Fröhlich Hamiltonian[12] describes, from a quantum mechanical viewpoint, the interaction of carriers with polar optical phonons; while this Hamiltonian cannot be solved exactly, a very accurate approximation, valid at any coupling strength, was obtained by Feynman, based on the path integral formulation.[21] The Feynman model can be solved exactly by variational approach [22–24], and accurate perturbative solutions can be found in both small- and strong-coupling limits, respectively. For the α values of interest ($0 < \alpha < 5$), the polaron self-energy is well reproduced by the expression:[25]

$$\frac{\varepsilon_P}{\hbar\omega_{LO}} = -\alpha - 0.0159\alpha^2 \quad (B10.2)$$

and the corresponding polaron mass enhancement by:

$$\frac{m_P}{m_{e,h}} = 1 + \frac{\alpha}{6} + 0.0236\alpha^2 \quad (B10.3)$$

For MAPI we obtain $\varepsilon_P = -32\, meV$, and $m_P = 0.34\, m_0$ (equal for electrons and holes, having assumed same electron and hole effective masses); these values, in good agreement with those reported in Ref. [19], can be exploited to evaluate the changes in the intrinsic carrier concentration due to the polaronic behaviour, and the corresponding $n_{th}^2/n_{p^+p^-}^2$ ratio, as described in the main test; to the aim, we calculate the intrinsic carrier concentration as:

$$n = \int_{E_{CBB}}^{\infty} d\varepsilon\, D(\varepsilon) f(\varepsilon - \varepsilon_F)$$
$$= \int_{-\infty}^{E_{VBT}} d\varepsilon\, D(\varepsilon)[1 - f(\varepsilon - \varepsilon_F)] \qquad (B10.4)$$

where $D(\varepsilon)$ is the 3D density of states in the effective-mass approximation, and $f(\varepsilon - \varepsilon_F)$ the Fermi-Dirac distribution; the polaron enhancement is then simply evaluated by shifting the band extrema according to the polaron self-energies, and using the polaron mass in the density of states. From Equation B10.4 at room T we obtain n_{th} $\sim 0.61 \times 10^5$ cm^{-3}, n_p $\sim 4.69 \times 10^5$ cm^{-3}, $\frac{n_{th}^2}{n_{p^+p^-}^2} = 1.71 \times 10^{-2}$

Appendix B: References

[1] A. Simbula, R. Pau, Q. Wang, F. Liu, V. Sarritzu, S. Lai, M. Lodde, F. Mattana, G. Mula, A. Geddo Lehmann, I. D. Spanopoulos, M. G. Kanatzidis, D. Marongiu, F. Quochi, M. Saba, A. Mura and G. Bongiovanni, *Adv. Opt. Mater.* **2021**, 2100295.

[2] C. Wehrenfennig, M. Liu, H. J. Snaith, M. B. Johnston and L. M. Herz, *Energy Environ. Sci.* **2014**, *7*, 2269–2275.

[3] P. Wurfel, *J. Phys. C Solid State Phys.* **1982**, *15*, 3967–3985.

[4] A. M. A. Leguy, P. Azarhoosh, M. I. Alonso, M. Campoy-Quiles, O. J. Weber, J. Yao, D. Bryant, M. T. Weller, J. Nelson, A. Walsh, M. Van Schilfgaarde and P. R. F. Barnes, *Nanoscale* **2016**, *8*, 6317–6327.

[5] N. Sestu, M. Cadelano, V. Sarritzu, F. Chen, D. Marongiu, R. Piras, M. Mainas, F. Quochi, M. Saba, A. Mura and G. Bongiovanni, *J. Phys. Chem. Lett.* **2015**, *6*, 4566–4572.

[6] R. J. Elliott, *Phys. Rev.* **1957**, *108*, 1384–1389.

[7] M. Saba, M. Cadelano, D. Marongiu, F. Chen, V. Sarritzu, N. Sestu, C. Figus, M. Aresti, R. Piras, A. Geddo Lehmann, C. Cannas, A. Musinu, F. Quochi, A. Mura and G. Bongiovanni, *Nat. Commun.* **2014**, *5*, 5049.

[8] C. L. Davies, M. R. Filip, J. B. Patel, T. W. Crothers, C. Verdi, A. D. Wright, R. L. Milot, F. Giustino, M. B. Johnston and L. M. Herz, *Nat. Commun.* **2018**, *9*, 293.

[9] P. Umari, E. Mosconi and F. De Angelis, *J. Phys. Chem. Lett.* **2018**, *9*, 620–627.

[10] K. Galkowski, A. Mitioglu, A. Miyata, P. Plochocka, O. Portugall, G. E. Eperon, J. T. W. Wang, T. Stergiopoulos, S. D. Stranks, H. J. Snaith and R. J. Nicholas, *Energy Environ. Sci.* **2016**, *9*, 962–970.

[11] T. Komesu, X. Huang, T. R. Paudel, Y. B. Losovyj, X. Zhang, E. F. Schwier, Y. Kojima, M. Zheng, H. Iwasawa, K. Shimada, M. I. Saidaminov, D. Shi, A. L. Abdelhady, O. M. Bakr, S. Dong, E.

Y. Tsymbal and P. A. Dowben, *J. Phys. Chem. C* **2016**, *120*, 21710–21715.

[12] H. Fröhlich, *Adv. Phys.* **1954**, *3*, 325–361.

[13] N. Onoda-Yamamuro, O. Yamamuro, Takasuke Matuso and H. Suga, *J. Phys. Chem. Solids* **1992**, *53*, 277–281.

[14] E. J. Juarez-Perez, R. S. Sanchez, L. Badia, G. Garcia-Belmonte, Y. S. Kang, I. Mora-Sero and J. Bisquert, *J. Phys. Chem. Lett.* **2014**, *5*, 2390–2394.

[15] F. Brivio, A. B. Walker and A. Walsh, *APL Mater.* **2013**, *1*, 042111.

[16] P. Umari, E. Mosconi and F. De Angelis, *Sci. Rep.* **2014**, *4*, 4467.

[17] A. Filippetti and A. Mattoni, *Phys. Rev. B - Condens. Matter Mater. Phys.* **2014**, *89*, 125203.

[18] M. A. Pérez-Osorio, R. L. Milot, M. R. Filip, J. B. Patel, L. M. Herz, M. B. Johnston and F. Giustino, *J. Phys. Chem. C* **2015**, *119*, 25703–25718.

[19] J. M. Frost, *Phys. Rev. B* **2017**, *96*, 195202.

[20] M. Schlipf, S. Poncé and F. Giustino, *Phys. Rev. Lett.* **2018**, *121*, 086402.

[21] R. P. Feynman, *Phys. Rev.* **1955**, *97*, 660–665.

[22] J. T. Devreese and A. S. Alexandrov, *Reports Prog. Phys.* **2009**, *72*, 066501.

[23] G. De Filippis, V. Cataudella, A. S. Mishchenko, C. A. Perroni and J. T. Devreese, *Phys. Rev. Lett.* **2006**, *96*, 136405.

[24] K. Miyata, T. L. Atallah and X. Y. Zhu, *Sci. Adv.* **2017**, *3*, e1701469.

[25] J. Röseler, *Phys. Status Solidi* **1968**, *25*, 311–316.

Chapter 4

Understanding photocatalytic doping of organic semiconductors

Recently, a promising sub-class of 2D perovskites, namely organic semiconductor-incorporated perovskites (OSiPs), has emerged. These next-generation hybrid materials can enhance the unique properties of 2D perovskites, that have made them so extensively studied in the last years. OSiPs represent a thrilling platform in which we can combine the excellent charge-transport properties of metal-halide perovskites with the rich chemical diversity and the possibility of tuning the optoelectronic properties that characterize the organic semiconductors[1–3].

In this framework, chemical doping is a key approach to manipulate charge carrier concentration and transport in organic semiconductors[4–6]*, ultimately enhancing their device performance*[7–10]*. However, conventional doping strategies often rely on energy-intensive vacuum*[11,12]*/high-temperature processing*[13] *conditions and highly reactive (strong) dopants*[14–16]*, which are consumed during the doping process. Achieving efficient doping with weak dopants under mild conditions remains a significant challenge.*

This chapter reports the optical spectroscopy characterization performed to understand the underlying photo-physics in a novel photocatalytic doping mechanism for organic semiconductors, utilizing air as a weak oxidant (p-dopant) and operating at room temperature. This approach is general and can be applied to various organic semiconductors and photocatalysts, yielding electrical conductivities that exceed 3000 S cm^{-1}.

The photocatalytic doping method studied here offers significant potential for advancing organic semiconductor doping and developing next-generation organic electronic devices.

Applying both time-resolved photoluminescence and transient absorption spectroscopy we were able to understand the steps of the charge transfer mechanism involved in this photodoping process opening to its application to other systems. We believe that this new doping mechanism will stimulate renewed attention on organic semiconductors but also on organic semiconductor-incorporated perovskites as new system for optoelectronic devices.

This chapter is extracted from the publication:
*W. Jin, C,Y. Yang, **R. Pau**, Q. Wang, E.K. Tekelenburg, H.Y. Wu, Z.Wu, F. Pitzalis, T. Liu, Q. He, Q. Li, R. Kroon, M.J. Heeney, H Y. Woo, A. Mura, M. Fahlman, M.A. Loi, S. Fabiano; Photocatalytic doping of organic semiconductors, Submitted manuscript.*

Contribution to the work: optical characterization of the samples (steady-state photoluminescence, time-resolved photoluminescence, transient absorption spectroscopy) and data analysis.

4.1 Introduction

Chemical doping is pivotal in optimizing the performance of various organic semiconductor-based devices, including light-emitting diodes[17], photovoltaics[18,19], field-effect transistors[20], thermoelectrics[21,22], and electrochemical devices[23,24]. Numerous doping methods have been developed to achieve effective chemical doping, such as direct electron transfer doping[25,26], stimulus-activated indirect doping[27–30], in-situ doping during polymerization[31,32], ground-state charge transfer[33–35], transition metal-catalyzed doping[36], and post-processing techniques involving secondary doping or ion exchange[37,38]. However, all these strategies rely on strong oxidizing/reducing agents (dopants) to alter the redox state of organic semiconductors. This often necessitates the use of large amounts of strong dopants, which are consumed during the doping process and result in undesirable chemical residues within the doped semiconductor films[39]. Moreover, these doping methods require harsh processing conditions to activate the dopants, such as vacuum evaporation[12,21] or high-temperature annealing[13,22]. Therefore, developing a mild doping strategy utilizing weak dopants is crucial to enhance compatibility with semiconductor devices.

Photocatalysis is a widely employed technique in organic synthesis due to its exceptional selectivity and efficiency in facilitating redox-based reactions[40–43]. Weak oxidants, such as oxygen in air[44,45], or weak reductants, like triethylamine or diisopropylethylamine[46,47], can effectively oxidize or reduce aromatic compounds through photoactivation or photoinduced electron transfer. Thus, intriguing questions are whether weak dopants can be photocatalytically activated to controllably and stably oxidize (p-dope)/reduce (n-dope) the π-electron system of organic semiconductors and whether this can have technological implications. Here, we explore the photocatalytic doping process in a quaternary system comprising a weak dopant, an acridinium-based photocatalyst (PC), an organic salt, and various conjugated p-type polymers to validate the general concept. We show that neither the weak dopant nor the PC in the ground state can extract electrons from the organic semiconductors (Fig. 4.1a-b). However, when excited by blue light, the PC can oxidize the organic semiconductor and subsequently be regenerated by the weak dopant (Fig. 4.1c-d). Acridinium-based PCs are used because of their commercial availability, air stability, and strong oxidizing/reducing character in their excited/radical reduced state[46,48,49]. We chose different acridinium derivatives (Acr-Me, Mes-Acr-Me, Mes-Acr-Ph) to

carry out the photocatalytic doping. Salts, such as LiTFSI, are used as the counterions to stabilize charges on the doped conjugated polymer backbones[38]. Weak oxidants (p-dopants) like oxygen (air) and disulfide[50] (DPDS) are utilized to regenerate the PCs.

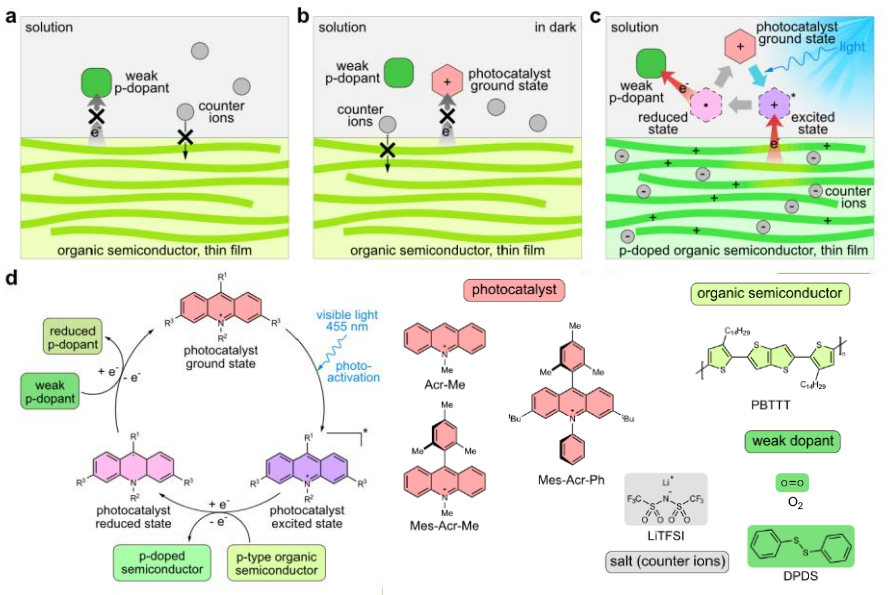

*Figure 4.1 Photocatalytic p-doping concept. a-c, Schematics of the photocatalytic p-doping process: weak p-dopants cannot oxidize the organic semiconductor (**a**); photocatalysts in the ground state cannot oxidize the organic semiconductor (**b**); photocatalysts in the excited state can oxidize the organic semiconductor and can be regenerated by the weak p-dopants (**c**). This photocatalytic doping process also occurs in thin films so that the organic semiconductor's molecular packing is preserved after doping. **d**, Proposed catalytic cycle of the photocatalytic p-doping and chemical structures of the photocatalysts, weak dopants, salt (counter ions), and organic semiconductor.*

4.2 Results and discussion

4.2.1 Photocatalytic oxidation (p-doping) of PBTTT

The photocatalytic p-doping methodology is straightforward and efficient, as demonstrated in Fig. 4.2 for the case-study oxidation of PBTTT by the photocatalyst Acr-Me. Acr-Me (0.01 M) was dissolved in

a mixture of n-butyl acetate and acetonitrile, together with the salt LiTFSI (0.1 M). This solvent mixture was chosen for its orthogonality to PBTTT and good solubility of Acr-Me and LiTFSI. PBTTT thin films were immersed in the Acr-Me:LiTFSI solution and irradiated with a 455 nm blue light ($t_{irradiation}$ up to 12 min) to photoactivate Acr-Me to its excited state (Acr-Me*, Ref.[44]) in the presence of oxygen (air), which acts as the weak p-dopant. The Acr-Me:LiTFSI solution was then recovered, and the p-doped PBTTT films were washed and dried as described in Fig. 4.2a. The UV-Vis-NIR absorption spectra of PBTTT films show that oxygen cannot dope PBTTT in the absence of Acr-Me or with Acr-Me in the dark (Fig. 4.2b), but a strong polaronic absorption extending in the NIR region was observed upon blue light irradiation. The electrical conductivity of PBTTT dramatically increases from 10^{-5} S cm^{-1} to over 700 S cm^{-1} after 10 min of light irradiation. In contrast, no significant changes in electrical conductivity are observed either without Acr-Me or with Acr-Me in the dark (Fig. 4.2c). Notably, the observed conductivity values are typical for molecularly p-doped PBTTT[38].

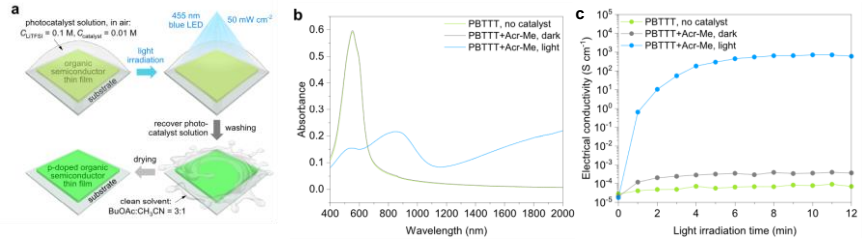

Figure 4.2 Photocatalytic p-doping of PBTTT. ***a****, Schematic of the photocatalytic p-doping method: the organic semiconductor film is immersed in the PC solution, also containing the TFSI- counterions, and irradiated with light in the presence of oxygen, which acts as the weak p-dopant. The PC solution is recovered, and the organic semiconductor film is washed with clean solvent and dried in nitrogen.* ***b****, Absorption spectra of undoped and doped PBTTT thin films. Photocatalytic doping only happens in the presence of both PC and light* ***c****, Electrical conductivity of undoped and photodoped PBTTT thin films, demonstrating photocatalytic doping can happen only when both photocatalyst and light are present.*

4.2.2 Mechanism and generality of the photocatalytic p-doping process

To understand the charge transfer mechanism involved in the photocatalytic p-doping process of the system (Figure 4.1), transient absorption spectroscopy (TAS) and photoluminescence (PL) spectroscopy experiments were performed.

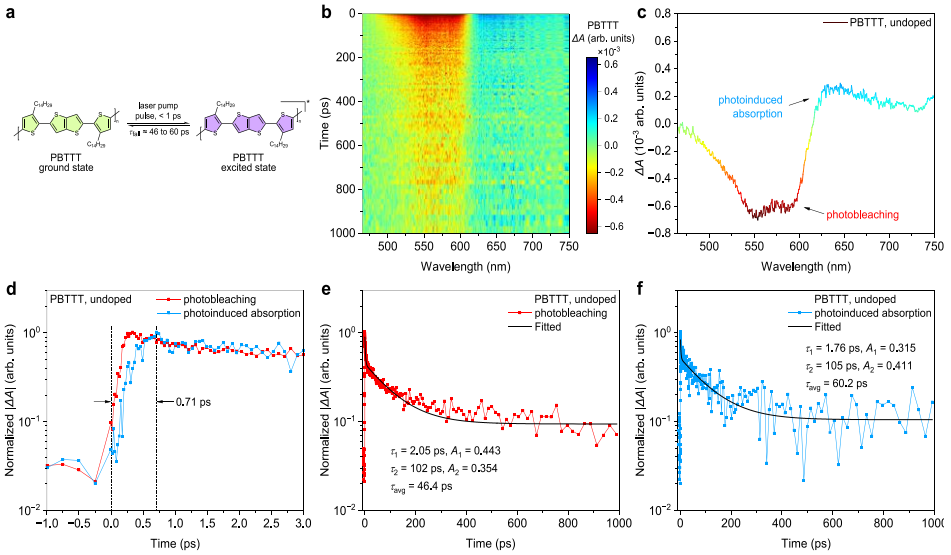

Figure 4.3 Transient absorption spectra (TAS) of undoped PBTTT. ***a,*** *Schematic diagram of the ground-to-excited state transition of undoped PBTTT under 390 nm laser pump pulse.* ***b,*** *False color representation of the transient absorption spectra of undoped PBTTT thin film as a function of delay time and detection wavelength.* ***c****, Transient absorption spectra of undoped PBTTT thin film showing the photobleaching (peak center 638 nm) and photoinduced absorption (peak center 553-574 nm).* ***d-f,*** *Time-dependent photobleaching and photoinduced absorption of the undoped PBTTT thin film, showing immediate raising (< 1 ps, limited by instrumental time resolution,* ***d****), followed by a decay dynamic with short excited life time of 46-60 ps (****e-f****).*

Undoped organic semiconductor PBTTT thin films reveal the presence of photobleaching peaks in the range of 550-575 nm, along with a photoinduced absorption peak at 638 nm (Fig. 4.3). By monitoring the decay of these features associated with excited state absorption/bleaching (Fig. 4.3e, f), we observed a relatively short excited state lifetime of 46-60 ps for the undoped PBTTT. Upon

photocatalytic doping with Acr-Me, PBTTT thin films exhibited a different behaviour, with the TA spectrograph showing a high energy photobleaching feature in the range of 465-544 nm and a photoinduced absorption region peaked at 647 nm (Fig. 4.4b-c). The extracted excited state lifetimes, as showed in Fig. 4.4e-f, are significantly shorter than the one of the undoped case, with values of 19-24 ps.

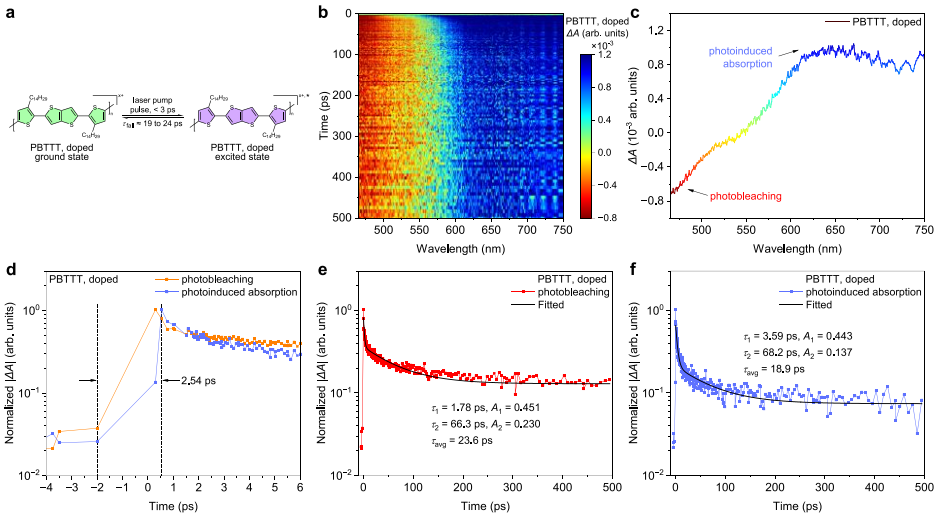

Figure 4.4 TAS of doped PBTTT. ***a,*** *Schematic diagram of the ground-to-excited state transition of photocatalytically doped PBTTT by Acr-Me, under 390 nm laser pump pulse.* ***b,*** *False colour representation of the transient absorption spectra of doped PBTTT thin film as a function of delay time and detection wavelength.* ***c****, Transient absorption spectra of doped PBTTT thin film showing the photobleaching (465-544 nm) and photoinduced absorption (peak centre 647 nm).* ***d-f,*** *Time-dependent photobleaching and photoinduced absorption of doped PBTTT thin film, showing immediate raising (< 3 ps, limited by instrumental time resolution,* ***d****), followed by a decay dynamic with short excited lifetime of 19-24 ps (****e-f****).*

In Fig. 4.5 the results of the transient absorption measurements on the photocatalyst Acr-Me are presented. The TAS spectra (Fig. 4.5b-c) exhibit a sharp photobleaching feature at 546 nm and a photoinduced absorption peak centred at 686 nm. In contrast with the PBTTT samples, Acr-Me exhibited a considerably longer excited state lifetime of 6-9 ns, which is 100 times longer than that of PBTTT (Fig. 4.5e-f). This substantial difference in excited state lifetimes is also reflected in their photoluminescence lifetimes (Figs. C.1-C.3), where Acr-Me shows a much longer PL lifetime (18 ns) when compared to the one of PBTTT

(0.9 ns). Note that all PCs show systematically longer PL lifetimes than the organic semiconductors (Fig C.4). These results imply that the photoinduced electron transfer (PET) process is likely to be dominated by the PC's excited state, with PET predominately occurring from the ground state of the organic semiconductor to the excited state of the PC.

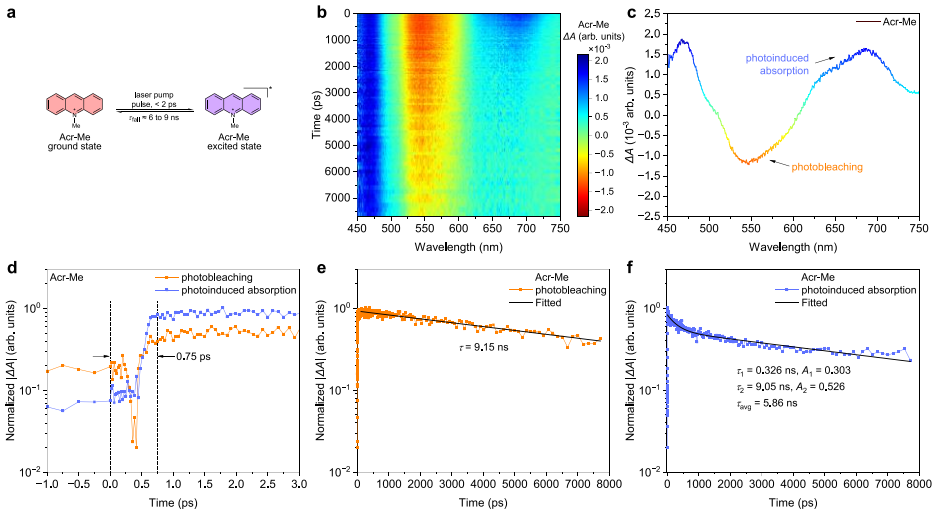

Figure 4.5 TAS of Acr-Me. ***a,*** *Schematic diagram of the ground-to-excited state transition of Acr-Me under 390 nm laser pump pulse.* ***b,*** *False color representation of the transient absorption spectra of Acr-Me solution (0.01 M, with 0.1 M of LiTFSI, in BuOAc:CH_3CN = 3:1) as a function of delay time and detection wavelength.* ***c****, Transient absorption spectra of Acr-Me showing the significant photobleaching (peak center 546 nm) and photoinduced absorption (peak center 686 nm).* ***d-f,*** *Time-dependent photobleaching and photoinduced absorption of Acr-Me, showing immediate raising (< 1 ps, limited by instrumental time resolution,* ***d****), followed by a decay dynamic with long excited lifetime of 6-9 ns (****e-f****). The excited lifetime of photocatalyst Acr-Me is around 100 times longer than that of semiconductor PBTTT thin film.*

To further support the notion that PET solely involves the excitation of PCs, we used the optically transparent triethylamine[47] (Et_3N) for an *in-situ* study of the PET process (Fig. 4.6 and C.8). Mes-Acr-Me and Mes-Acr-Ph were selected as representative PCs due to their excellent stability in the presence of basic Et_3N (Fig. C.5). PET between Mes-Acr-Me* (or Mes-Acr-Ph*) and Et_3N induces the formation of Mes-Acr-Me (or Mes-Acr-Ph) reduced state[46,49] as revealed by the absorption

spectra shown in Figs. C.5-C.6. Notably, this photo-reduced state matches the single-electron-transfer reduced state induced by the strong reducing agent tetrakis(dimethylamino)ethylene (TDAE, Fig. C.6). Subsequently, Mes-Acr-Me (or Mes-Acr-Ph) can be regenerated through oxidation with oxygen in air or the weak oxidant DPDS[50] (Figs. 4.7 and C.5).

Moreover, *in-situ* TAS spectra acquired during the PET reduction/oxidation-regeneration process reveal that Mes-Acr-Me initially forms an intramolecular-charge-transfer[45,51] (ICT) excited state under light irradiation (Fig. 4.6a-b and Figs. C.7-C.8).

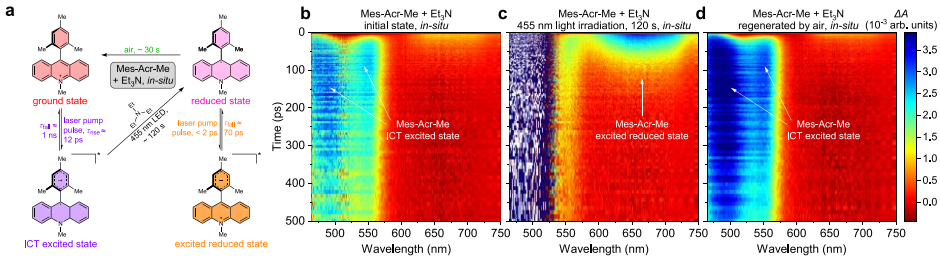

Figure 4.6 Mechanism and generality of photocatalytic p-doping. ***a,*** *Schematic diagram of the transition of the ground state, excited state, reduced state, and excited reduced state of photocatalyst Mes-Acr-Me. The transitions depend on the laser pump pulse exciting or reacting with optically transparent n-dopant (triethylamine) under 455 nm light irradiation or regenerating in air. b-d, False color plot of the in-situ transient absorption spectra (TAS) of PC (Mes-Acr-Me) + 10 equivalent weak n-dopant (triethylamine) solution, as the function of detector wavelength and delay time: initial state in nitrogen atmosphere* ***(b),*** *after 455 nm light irradiation for 120 s in nitrogen* ***(c),*** *and PC regenerated in air* ***(d)****. Two strong photoinduced absorption peaks (477 nm and 551 nm, b and d) indicate the excited state of Mes-Acr-Me. The significant photoinduced absorption peak at 658 nm (panel c) indicates the excited reduced state of Mes-Acr-Me.*

As depicted in Fig. 4.6b, the initial state of Mes-Acr-Me is dominated by the photoinduced absorption peak at 551 nm. Subsequently, Mes-Acr-Me transitions to the reduced state in the presence of Et_3N. As the 455 nm light irradiation time grows, a significant second photoinduced absorption band at lower energies (658 nm) appears, indicating the formation of an excited reduced state of Mes-Acr-Me under laser pump pulse (Fig. 4.6c). Upon oxidation in air, Mes-Acr-Me is fully regenerated to its initial state (Fig. 4.6d and Fig. C.8). This result strongly supports the notion that the PET process solely requires the

excitation of PCs and that PCs can be fully regenerated in air, thereby closing the catalytic cycle shown in Fig. 4.1d. The consistency of the regeneration is further confirmed by the comparable decay times for the high energy photoinduced absorption band measured at the initial state and after the regeneration (Figure C.8l-n).

In-situ photoluminescence studies demonstrate the reduction and regeneration of Mes-Acr-Me and Mes-Acr-Ph (Fig. 4.7). In Fig. 4.7a-d are showed the absorption spectra and the solutions pictures of the two photocatalysts when in the initial state, after 120 s of 455 nm light irradiation, and after regeneration in air, respectively. In both cases the data show the change in absorption of the system upon light irradiation, while no change is observed in dark, even with the presence of the triethylamine. Figures 4.7b-e show the quenching in intensity of the PL peaks, located at 591 and 535 nm respectively, as the irradiation time grows from 0 s (initial state) to 120 s and how the initial intensity is then fully regenerated with the exposure to air.

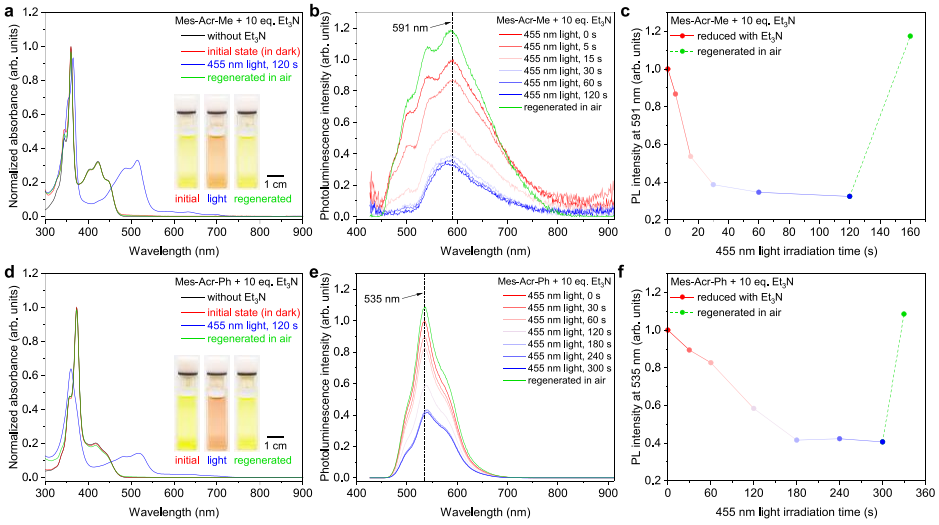

Figure 4.7 Photocatalyst reduction and regeneration. ***a,*** *Absorption spectra of Mes-Acr-Me/Et_3N solution, in initial state (in dark), irradiated under 455 nm light, and regenerated in air. Inset: photographs of Mes-Acr-Me/Et_3N solution in the above three state. Absorption spectra of pure Mes-Acr-Me is also shown for comparison, demonstrates that Et_3N cannot reduce Mes-Acr-Me without light.* ***b****, In-situ photoluminescence spectra of Mes-Acr-Me/Et_3N solution, in initial state, irradiated under 455 nm light, and regenerated in air.* ***c****, Photoluminescence intensity at 591 nm of the above Mes-Acr-Me/Et_3N solution.* ***d,*** *Absorption spectra of Mes-Acr-Ph/Et_3N solution, in initial state (in dark), irradiated under 455 nm light, and regenerated in air. Inset: photographs of Mes-Acr-Ph/Et_3N solution in the above three state.*

Absorption spectra of pure Mes-Acr-Ph is also shown for comparison, demonstrates that Et_3N cannot reduce Mes-Acr-Ph without light. ***e****, In-situ photoluminescence spectra of Mes-Acr-Ph/Et_3N solution, in initial state, irradiated under 455 nm light, and regenerated in air.* ***c****, Photoluminescence intensity at 535 nm of the above Mes-Acr-Ph/Et_3N solution. The photo catalysts Mes-Acr-Me and Mes-Acr-Ph show excellent photoreduction and oxidation regeneration abilities, with optically transparent weak n-dopant triethylamine and air. This further proves that the photo-redox of photocatalysts does not require the participation of organic semiconductors, further suggesting that photocatalysis is dominated by the excited state of the photocatalysts.*

Measuring the luminescence intensity variation of the photocatalyst excited state in the presence of a quencher is a crucial stage in the study of any photoredox reaction that involves photoinduced electron transfer or energy transfer. Also known as Sterm-Volmer analysis, this emission quenching study measures the rate of quenching of a photocatalyst as a function of its concentration.
The decrease in luminescence intensity at a certain quencher concentration [Q] is described by the Stern-Volmer relationship as follows[52]:

$$\frac{I_0}{I} = 1 + k_q \tau_0 [Q] \quad (1)$$

where I and I_0 are the luminescence intensities with and without the presence of the quencher, respectively, $\tau 0$ is the excited state lifetime and k_q is the quencher constant.
If the photoluminescence lifetime is known, then the bimolecular rate k_q can be determined from the steady state measurements in a simple optical spectroscopy setup.
To determine the quencher constant, a combined steady-state and time-resolved photoluminescence experiment has been carried out.
As depicted in Fig. 4.8, we checked the absorption spectra of pure organic semiconductor PBTTT and the pure photocatalyst Mes-Acr-Ph in a common solvent, 1,2-Dichlorobenzene (ODCB) and we compared to the absorption spectra of the mixed solution of the two. The overlap between the pure spectra (PBTTT and Mes-Acr-Ph) and the spectra of the mixed two showed a consistent superposition (Fig. 4.8b).

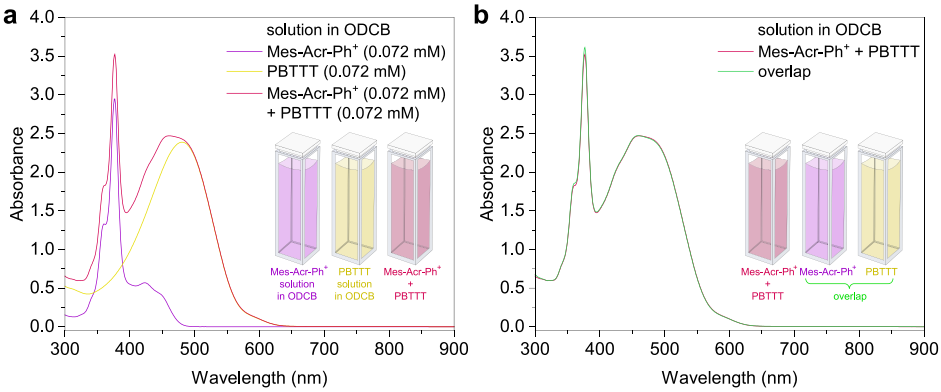

Figure 4.8 Stern-Volmer experiment. ***a,*** *Absorption spectra of pure Mes-Acr-Ph (0,072 mM) and PBTTT solutions (0,072 mM) in 1,2-Dichlorobenzene (ODCB) and of the mixed solution of Mes-Acr-Ph + PBTTT. Inset: schematic representations of the experimental samples.* ***b,*** *Absorbance spectra of the mixed solution of Mes-Acr-Ph + PBTTT and overlap of the two respective single spectra showing the superposition between the two cases. Inset: schematic representations of the experimental samples taken into consideration.*

As first we considered the Mes-Acr-Ph system in which PBTTT is considered the quencher. The photoluminescence spectra of pure Mes-Acr-Ph and pure PBTTT in ODCB are presented in Fig. 4.9a, in which the main features are located at 495 nm and 582 nm, respectively.

In Fig. 4.9c the photoluminescence spectra of the photocatalyst at different concentrations of PBTTT are presented.
As the concentration of the organic semiconductor in the solution grows, the peak attributable to Mes-Acr-Ph, located at 495 nm, decreases in intensity, while the PBTTT peak, located at 582 nm, increases.
At the maximum concentration of 1 eq of PBTTT the quenching of the 495 nm peak of Mes-Acr-Ph is equal to 47% of its initial intensity (at concentration 0 eq PBTTT).
Using the photoluminescence lifetime extrapolated as in Fig. 4.9b, using Eq.1 we plotted the ratio I_0/I at the different concentrations of PBTTT used in the analysis as shown in Fig. 4.9d, where the results of the linear fitting are presented with a final value for the quencher constant of $k_q = (4.87 \pm 0.06) 10^{11}$ L mol^{-1} s^{-1}.

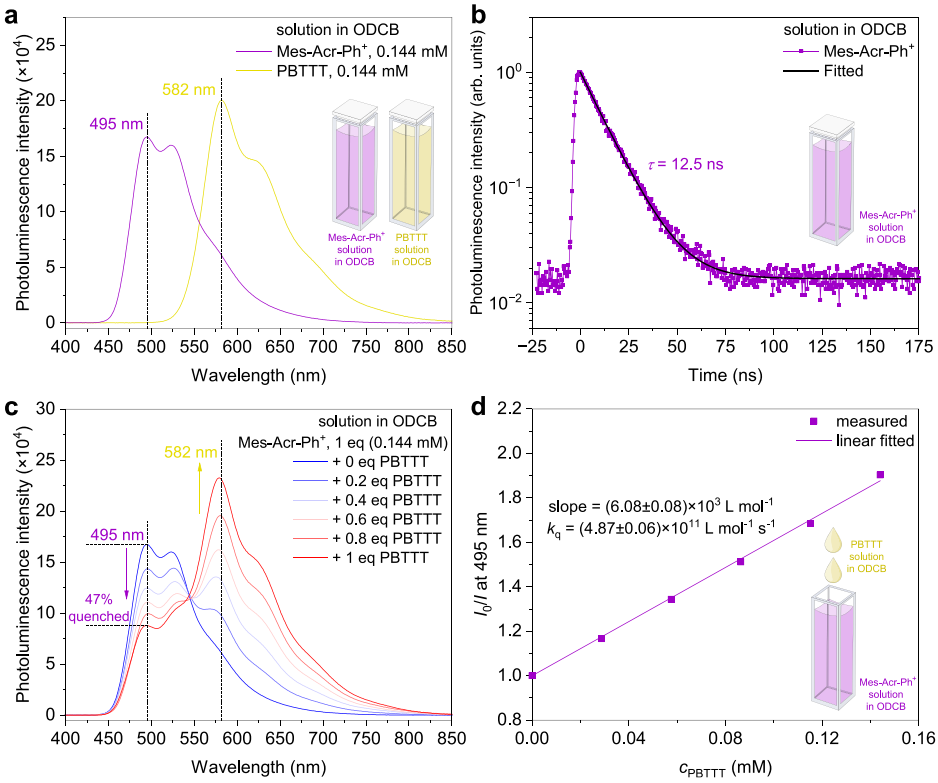

Figure 4.9 Stern-Volmer analysis with PBTTT as the quencher. ***a,*** *Photoluminescence spectra of pure Mes-Acr-Ph (0,144 mM) and PBTTT solutions (0,144 mM) in 1,2-Dichlorobenzene (ODCB). Inset: schematic representations of the experimental samples.* ***b,*** *Time-resolved photoluminescence decay of pure Mes-Acr-Ph solution in ODCb. Inset: schematic representations of the experimental sample.* ***c****, Photoluminescence spectra of Mes-Acr-Ph solutions at different PBTTT concentrations, showing the intensity quenching at 495 nm up to 47% at 1 eq concentration of PBTTT.* ***d,*** *I/I0 vs PBTTT concentration plot and linear fitting with extrapolated slope and quencher constant. Inset: schematic representations of the experiment.*

In the second part of the Stern-Volmer analysis, for consistency, we inverted the roles of the organic semiconductor and of the photocatalyst, namely now Mes-Acr-Ph is considered the quencher.
In Fig. 4.10a the photoluminescence spectra of the PBTTT at different concentrations of the photocatalyst are presented. Also in this case, when the quencher is inserted in the system, we can observe the combination of the respective photoluminescence features of the two pure materials.

As the concentration of Mes-Acr-Ph in the solution increases, the peak attributable to PBTTT, located at 582 nm, decreases in intensity.
At the maximum concentration of 1 eq of the photocatalyst, the quenching of the PBTTT peak is equal to 3.9% of its initial intensity (at concentration 0 eq Mes-Acr-Ph).
Using the photoluminescence lifetime extrapolated as in Fig. 4.10c and Eq.1 we plotted the ratio I_0/I at the different concentrations of Mes-Acr-Ph used in the analysis, as shown in Fig. 4.10d, where the results of the linear fitting are presented with a final value for the quencher constant of $k_q = (4.89 \pm 0.05)\ 10^{11}$ L mol^{-1} s^{-1}.

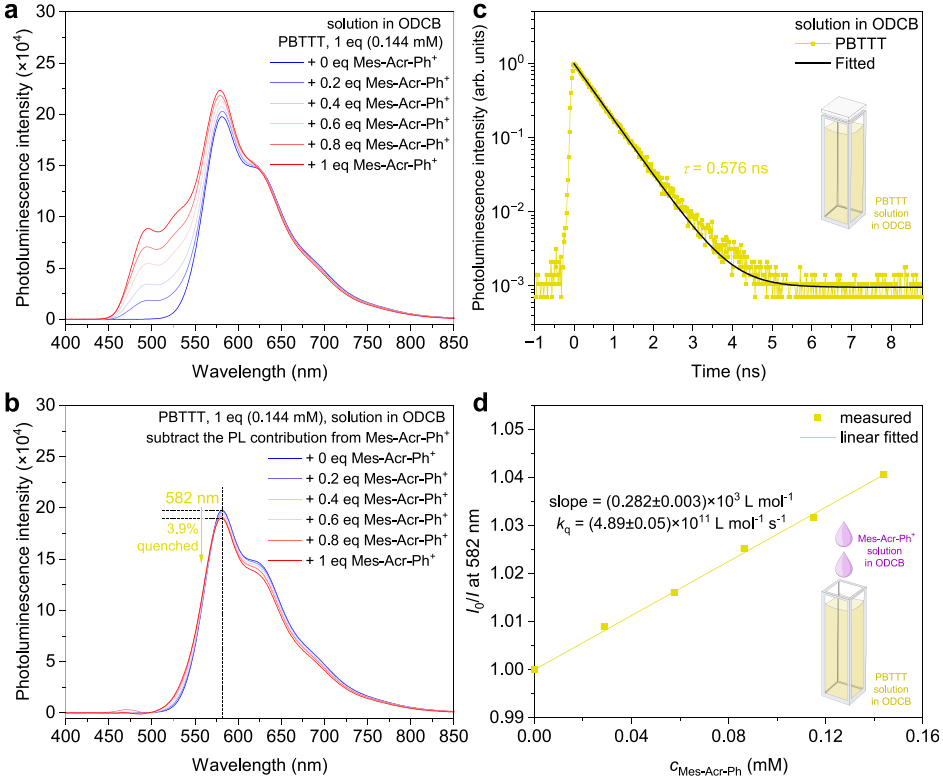

Figure 4.10 Stern-Volmer analysis with Mes-Acr-Ph as the quencher. ***a,*** *Photoluminescence spectra of PBTTT solutions at different Mes-Acr-Ph concentrations.* ***b,*** *Time-resolved photoluminescence decay of pure PBTTT solution in ODCB. Inset: schematic representations of the experimental sample.* ***c****, Photoluminescence spectra of PBTT solutions at different Mes-Acr-Ph concentrations, with the subtracted pL contribution from Mes-Acr-Ph. The graph shows the intensity quenching at 582 nm up to 3.9% at 1 eq concentration of Mes-Acr-Ph.****d,*** *I/I0 vs PBTTT concentration plot and linear fitting with extrapolated slope and quencher constant. Inset: schematic representations of the experiment.*

As result of the Stern-Volmer analysis, the two values obtained for the quencher constant k_q, considering respectively the PBTTT or the Mes-Acr-Ph as the quencher, are comparable inside the experimental error.

4.3 Conclusions

In summary, we investigated the mechanism of photocatalytic doping for organic semiconductors. Interesting, the doping level can be easily controlled by adjusting the light irradiation dose. Compared to conventional doping methods that rely on highly reactive dopants, which are consumed during the doping process, photocatalytic doping employs recyclable and air-stable PCs and consumes only TSFI-based salt and weak dopants, such as oxygen (air). This general method can be applied to a wide range of organic semiconductors. By optical investigation we enlighten how the PET process is possibly dominated by the excited state of the photocatalyst, which shows systematic longer excited state lifetimes. This photoinduced electron transfer is mainly occurring from the ground state of the organic semiconductor to the excited state of the photocatalyst.
Moreover, in-situ PL and TAS measurements on the photocatalyst Mes-Acr-Me, reveal that under light irradiation, an initial intramolecular-charge-transfer excited state is formed. Finally, a full picture on the regeneration in air of the photocatalysts, within its catalytic cycle, was demonstrated. The characterization of the photodoping system was further carried out by Stern-Volmer analysis, with the experimental calculation of the photoluminescence quencher constants being $kq = (4.87 \pm 0.06) 10^{11}$ L mol^{-1} s^{-1} and (4.89 ± 0.05) 10^{11} L mol^{-1} s^{-1} for PBTTT and Mes-Acr-Ph, respectively.

4.4 Experimental Section

4.4.1 Photoluminescence spectroscopy

The samples were excited at 3.1 eV (400 nm) using the second harmonic of a mode-locked Ti:sapphire laser (Mira 900, coherent) at a repetition rate of 76 MHz. The excitation beam was spatially limited by an iris and focused with a lens of 150 mm focal length. The fluence was adjusted using neutral density filters to 76 nJ cm^{-2}. The excitation fluence per pulse was estimated assuming the diameter of the focused beam dfocus is equal to $1.27 \times flens M^2/D$, where flens is the focal length, M the quality factor (assumed to be 1), and D the incident diameter of the excitation beam. The spectra were taken in reflection geometry. The photoluminescence was collected using an achromatic doublet, where 425 nm and 435 nm long pass filters were used to block the scattered laser light. Steady-state spectra were recorded with a Hamamatsu EM-CCD camera that was spectrally calibrated with a spectrograph equipped with a 50 l/mm grating. Time-resolved traces were taken with a Hamamatsu streak camera working in single sweep mode. A pulse picker was used to vary the repetition rate of the exciting pulses. The absolute photoluminescence quantum yields (PLQYs) were measured using a Horiba Scientific Jobin Yvon spectrometer equipped with a Quanta-φ Integrating Sphere.

4.4.2 Transient absorption spectroscopy

The differential transmission was measured by exciting the samples with an ultrafast laser source (100-fs laser pulses at 390 nm) obtained from a Ti:sapphire regenerative amplifier (Coherent Libra) with a repetition rate of 1 kHz and an optical parametric amplifier (Topas 800, Light Conversion). The pump pulses had a fluency of the order of 100 μJ cm^{-2} adjusted in order to have the best signal-to-noise ratio while avoiding sample degradation. DT/T measurements were performed by probing the samples with fs supercontinuum white pulses (with a spectral range from 400 to 800 nm) at different time delays with respect to the excitation (pump) pulses, in a pump-probe configuration in which a transmitted beam and a reference beam are acquired with two CMOS grating spectrometers with 1 nm of spectral resolution (Ultrafast Systems Helios). The overall temporal resolution was always of the same order of magnitude of the excitation pulses (120 fs, FWHM).

4.5 References

[1] J. Sun, K. Wang, K. Ma, J. Y. Park, Z. Y. Lin, B. M. Savoie, L. Dou, *J. Am. Chem. Soc.* **2023**, *145*, 20694.

[2] J. Y. Park, R. Song, J. Liang, L. Jin, K. Wang, S. Li, E. Shi, Y. Gao, M. Zeller, S. J. Teat, P. Guo, L. Huang, Y. S. Zhao, V. Blum, L. Dou, *Nat. Chem.* **2023**, *15*, 1745-1753.

[3] W. Shao, S. Yang, K. Wang, L. Dou, *J. Phys. Chem. Lett.* **2023**, *14*, 2034.

[4] A. D. Scaccabarozzi, A. Basu, F. Aniés, J. Liu, O. Zapata-Arteaga, R. Warren, Y. Firdaus, M. I. Nugraha, Y. Lin, M. Campoy-Quiles, N. Koch, C. Müller, L. Tsetseris, M. Heeney, T. D. Anthopoulos, *Chem. Rev.* **2022**, *122*, 4420.

[5] I. E. Jacobs, A. J. Moulé, *Adv. Mater.* **2017**, *29*, 1703063.

[6] B. Lüssem, M. Riede, K. Leo, *Physica Status Solidi* **2013**, *210*, *9-43*.

[7] Z. Liang, H. H. Choi, X. Luo, T. Liu, A. Abtahi, U. S. Ramasamy, J. A. Hitron, K. N. Baustert, J. L. Hempel, A. M. Boehm, A. Ansary, D. R. Strachan, J. Mei, C. Risko, V. Podzorov, K. R. Graham, *Nat. Mater.* **2021**, *20*, 518.

[8] C. G. Tang, M. C. Y. Ang, K. K. Choo, V. Keerthi, J. K. Tan, M. N. Syafiqah, T. Kugler, J. H. Burroughes, R. Q. Png, L. L. Chua, P. K. H. Ho, *Nature* **2016**, *539*, 536.

[9] B. Lüssem, C. M. Keum, D. Kasemann, B. Naab, Z. Bao, K. Leo, *Chem. Rev.* **2016**, *116*, 13714.

[10] C. Cea, G. D. Spyropoulos, P. Jastrzebska-Perfect, J. J. Ferrero, J. N. Gelinas, D. Khodagholy, *Nat. Mater.* **2020**, *19*, 679.

[11] C. Gaul, S. Hutsch, M. Schwarze, K. S. Schellhammer, F. Bussolotti, S. Kera, G. Cuniberti, K. Leo, F. Ortmann, *Nat. Mater.* **2018**, *17*, 439.

[12] M. Schwarze, C. Gaul, R. Scholz, F. Bussolotti, A. Hofacker, K. S. Schellhammer, B. Nell, B. D. Naab, Z. Bao, D. Spoltore, K.

Vandewal, J. Widmer, S. Kera, N. Ueno, F. Ortmann, K. Leo, *Nat. Mater.* **2019**, *18*, 242.

[13] C. Y. Yang, Y. F. Ding, D. Huang, J. Wang, Z. F. Yao, C. X. Huang, Y. Lu, H. I. Un, F. D. Zhuang, J. H. Dou, C. an Di, D. Zhu, J. Y. Wang, T. Lei, J. Pei, *Nat. Commun.* **2020**, *11*, 3292.

[14] B. Yurash, D. X. Cao, V. V. Brus, D. Leifert, M. Wang, A. Dixon, M. Seifrid, A. E. Mansour, D. Lungwitz, T. Liu, P. J. Santiago, K. R. Graham, N. Koch, G. C. Bazan, T. Q. Nguyen, *Nat. Mater.* **2019**, *18*, 1327.

[15] V. A. Kolesov, C. Fuentes-Hernandez, W. F. Chou, N. Aizawa, F. A. Larrain, M. Wang, A. Perrotta, S. Choi, S. Graham, G. C. Bazan, T. Q. Nguyen, S. R. Marder, B. Kippelen, *Nat. Mater.* **2017**, *16*, 474.

[16] S. Wang, H. Sun, U. Ail, M. Vagin, P. O. Å. Persson, J. W. Andreasen, W. Thiel, M. Berggren, X. Crispin, D. Fazzi, S. Fabiano, *Adv. Mater.* **2016**, *28*, 10764.

[17] C. G. Tang, M. N. Syafiqah, Q. M. Koh, C. Zhao, J. Zaini, Q. J. Seah, M. J. Cass, M. J. Humphries, I. Grizzi, J. H. Burroughes, R. Q. Png, L. L. Chua, P. K. H. Ho, *Nature* **2019**, *573*, 519.

[18] T. Zhang, F. Wang, H. B. Kim, I. W. Choi, C. Wang, E. Cho, R. Konefal, Y. Puttisong, K. Terado, L. Kobera, M. Chen, M. Yang, S. Bai, B. Yang, J. Suo, S. C. Yang, X. Liu, F. Fu, H. Yoshida, W. M. Chen, J. Brus, V. Coropceanu, A. Hagfeldt, J. L. Brédas, M. Fahlman, D. S. Kim, Z. Hu, F. Gao, *Science* **2022**, *377*, 495.

[19] N. Sakai, R. Warren, F. Zhang, S. Nayak, J. Liu, S. V. Kesava, Y. H. Lin, H. S. Biswal, X. Lin, C. Grovenor, T. Malinauskas, A. Basu, T. D. Anthopoulos, V. Getautis, A. Kahn, M. Riede, P. K. Nayak, H. J. Snaith, *Nat. Mater.* **2021**, *20*, 1248.

[20] T. Sawada, A. Yamamura, M. Sasaki, K. Takahira, T. Okamoto, S. Watanabe, J. Takeya, *Nat. Commun.* **2020**, *11*, 4839.

[21] J. Liu, B. van der Zee, R. Alessandri, S. Sami, J. Dong, M. I. Nugraha, A. J. Barker, S. Rousseva, L. Qiu, X. Qiu, N. Klasen, R. C. Chiechi, D. Baran, M. Caironi, T. D. Anthopoulos, G. Portale, R. W. A. Havenith, S. J. Marrink, J. C. Hummelen, L. J. A. Koster, *Nat. Commun.* **2020**, *11*, 5694.

[22] X. Yan, M. Xiong, X. Y. Deng, K. K. Liu, J. T. Li, X. Q. Wang, S. Zhang, N. Prine, Z. Zhang, W. Huang, Y. Wang, J. Y. Wang, X. Gu, S. K. So, J. Zhu, T. Lei, *Nat. Commun.* **2021**, *12*, 5723.

[23] A. F. Paterson, A. Savva, S. Wustoni, L. Tsetseris, B. D. Paulsen, H. Faber, A. H. Emwas, X. Chen, G. Nikiforidis, T. C. Hidalgo, M. Moser, I. P. Maria, J. Rivnay, I. McCulloch, T. D. Anthopoulos, S. Inal, *Nat. Commun.* **2020**, *11*, 3004.

[24] S. T. M. Tan, G. Lee, I. Denti, G. LeCroy, K. Rozylowicz, A. Marks, S. Griggs, I. McCulloch, A. Giovannitti, A. Salleo, *Adv. Mater.* **2022**, *34*, 20202359.

[25] K. Kang, S. Watanabe, K. Broch, A. Sepe, A. Brown, I. Nasrallah, M. Nikolka, Z. Fei, M. Heeney, D. Matsumoto, K. Marumoto, H. Tanaka, S. I. Kuroda, H. Sirringhaus, *Nat. Mater.* **2016**, *15*, 896.

[26] D. Kiefer, R. Kroon, A. I. Hofmann, H. Sun, X. Liu, A. Giovannitti, D. Stegerer, A. Cano, J. Hynynen, L. Yu, Y. Zhang, D. Nai, T. F. Harrelson, M. Sommer, A. J. Moulé, M. Kemerink, S. R. Marder, I. McCulloch, M. Fahlman, S. Fabiano, C. Müller, *Nat. Mater.* **2019**, *18*, 149.

[27] X. Lin, B. Wegner, K. M. Lee, M. A. Fusella, F. Zhang, K. Moudgil, B. P. Rand, S. Barlow, S. R. Marder, N. Koch, A. Kahn, *Nat. Mater.* **2017**, *16*, 1209.

[28] P. Wei, J. H. Oh, G. Dong, Z. Bao, *J. Am. Chem. Soc.* **2010**, *132*, 8852.

[29] C. Y. Yang, M. A. Stoeckel, T. P. Ruoko, H. Y. Wu, X. Liu, N. B. Kolhe, Z. Wu, Y. Puttisong, C. Musumeci, M. Massetti, H. Sun, K. Xu, D. Tu, W. M. Chen, H. Y. Woo, M. Fahlman, S. A. Jenekhe, M. Berggren, S. Fabiano, *Nat. Commun.* **2021**, *12*, 2354.

[30] P. Wei, T. Menke, B. D. Naab, K. Leo, M. Riede, Z. Bao, *J. Am. Chem. Soc.* **2012**, *134*, 3999.

[31] H. Tang, Y. Liang, C. Liu, Z. Hu, Y. Deng, H. Guo, Z. Yu, A. Song, H. Zhao, D. Zhao, Y. Zhang, X. Guo, J. Pei, Y. Ma, Y. Cao, F. Huang, *Nature* **2022**, *611*, 271.

[32] H. Yano, K. Kudo, K. Marumo, H. Okuzaki, *Sci. Adv.* **2019**, *5*, eaav9492.

[33] K. Xu, H. Sun, T. P. Ruoko, G. Wang, R. Kroon, N. B. Kolhe, Y. Puttisong, X. Liu, D. Fazzi, K. Shibata, C. Y. Yang, N. Sun, G. Persson, A. B. Yankovich, E. Olsson, H. Yoshida, W. M. Chen, M. Fahlman, M. Kemerink, S. A. Jenekhe, C. Müller, M. Berggren, S. Fabiano, *Nat. Mater.* **2020**, *19*, 738.

[34] I. E. Jacobs, C. Cendra, T. F. Harrelson, Z. I. Bedolla Valdez, R. Faller, A. Salleo, A. J. Moulé, *Mater. Horizons* **2018**, *5*, 655.

[35] H. Alves, A. S. Molinari, H. Xie, A. F. Morpurgo, *Nat. Mater.* **2008**, *7*, 574.

[36] H. Guo, C. Y. Yang, X. Zhang, A. Motta, K. Feng, Y. Xia, Y. Shi, Z. Wu, K. Yang, J. Chen, Q. Liao, Y. Tang, H. Sun, H. Y. Woo, S. Fabiano, A. Facchetti, X. Guo, *Nature* **2021**, *599*, 67.

[37] G. H. Kim, L. Shao, K. Zhang, K. P. Pipe, *Nat. Mater.* **2013**, *12*, 719.

[38] Y. Yamashita, J. Tsurumi, M. Ohno, R. Fujimoto, S. Kumagai, T. Kurosawa, T. Okamoto, J. Takeya, S. Watanabe, *Nature* **2019**, *572*, 634.

[39] S. Jhulki, H. I. Un, Y. F. Ding, C. Risko, S. K. Mohapatra, J. Pei, S. Barlow, S. R. Marder, *Chem* **2021**, *7*, 1050.

[40] W. Chen, Z. Huang, N. E. S. Tay, B. Giglio, M. Wang, H. Wang, Z. Wu, D. A. Nicewicz, Z. Li, *Science* **2019**, *364*, 1170.

[41] K. Kwon, R. T. Simons, M. Nandakumar, J. L. Roizen, *Chem. Rev.* **2022**, *122*, 2353.

[42] D. A. Corbin, G. M. Miyake, *Chem. Rev.* **2022**, *122*, 1830.

[43] N. A. Romero, D. A. Nicewicz, *Chem. Rev.* **2016**, *116*, 10075.

[44] N. A. Romero, K. A. Margrey, N. E. Tay, D. A. Nicewicz, *Science* **2015**, *349*, 1326.

[45] K. Ohkubo, K. Mizushima, R. Iwataa, S. Fukuzumi, *Chem. Sci.* **2011**, *2*, 715.

[46] I. A. MacKenzie, L. Wang, N. P. R. Onuska, O. F. Williams, K. Begam, A. M. Moran, B. D. Dunietz, D. A. Nicewicz, *Nature* **2020**, *580*, 76.

[47] I. Ghosh, T. Ghosh, J. I. Bardagi, B. König, *Science* **2014**, *346*, 725.

[48] N. A. Romero, D. A. Nicewicz, *J. Am. Chem. Soc.* **2014**, *136*, 17024.

[49] A. C. Benniston, A. Harriman, P. Li, J. P. Rostron, H. J. Van Ramesdonk, M. M. Groeneveld, H. Zhang, J. W. Verhoeven, *J. Am. Chem. Soc.* **2005**, *127*, 16054.

[50] D. J. Wilger, J. M. M. Grandjean, T. R. Lammert, D. A. Nicewicz, *Nat. Chem.* **2014**, *6*, 720.

[51] M. Hoshino, H. Uekusa, A. Tomita, S. Y. Koshihara, T. Sato, S. Nozawa, S. I. Adachi, K. Ohkubo, H. Kotani, S. Fukuzumi, *J. Am. Chem. Soc.* **2012**, *134*, 4569.

[52] M. H. Gehlen, *J. Photochem. Photobiol. C Photochem. Rev.* **2020**, *42*, 100338.

Appendix C: Additional data to Chapter 4

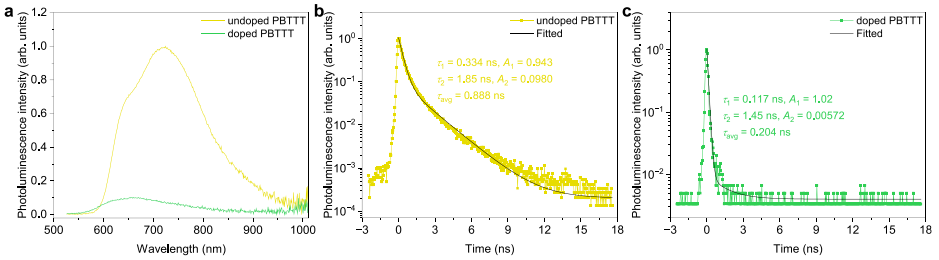

Figure C.1 Photoluminescence spectra of PBTTT. ***a****, Photoluminescence spectra of undoped and doped (photocatalyzed by Acr-Me) PBTTT thin films.* ***b-c****, Time-resolved photoluminescence spectra of undoped (****b****) and doped (****c****) PBTTT, showing short fluorescence lifetime of 0.9 ns and 0.2 ns (for undoped and doped PBTTT, limited by instrumental time resolution). The excitation wavelength is 400 nm.*

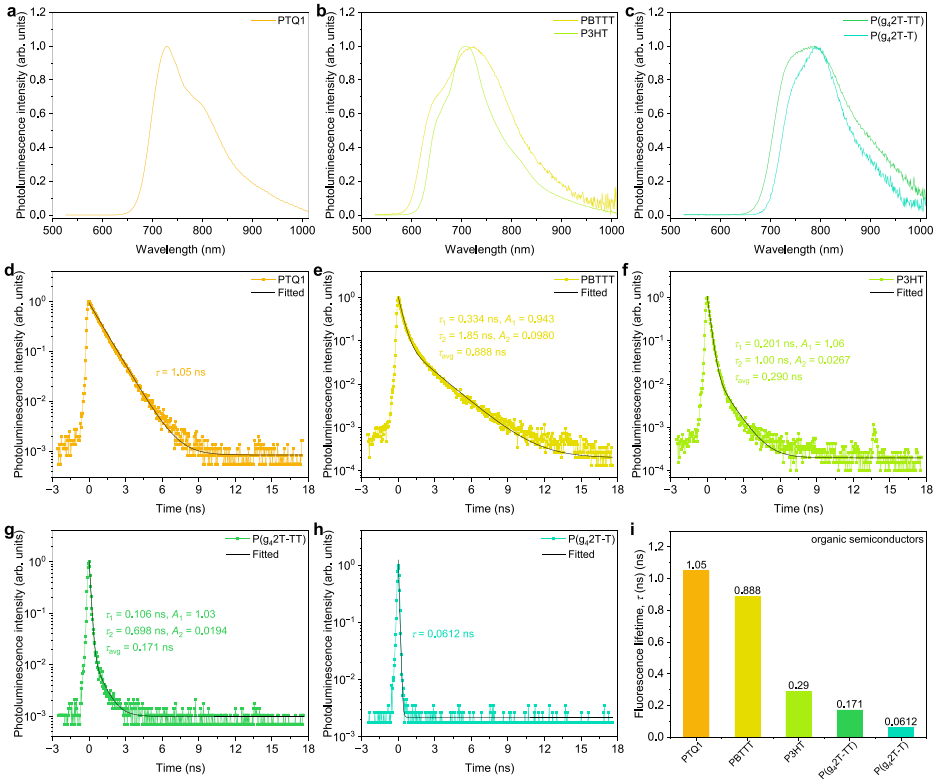

Figure C.2 Photoluminescence spectra of organic semiconductors. ***a-c,*** *Photoluminescence spectra of undoped PTQ1 (a), PBTTT and P3HT (b),*

*and P(g$_4$2T-TT) and P(g$_4$2T-TT) **(c)** thin films. d-f, Time-resolved photoluminescence spectra of PTQ1 **(d)**, PBTTT **(e)**, P3HT **(f)**, P(g$_4$2T-TT) (g), and P(g$_4$2T-T) **(h)** thin films. **i,** Fluorescence lifetime of the above organic semiconductors. The fluorescence lifetime of P(g$_4$2T-TT) and P(g$_4$2T-T) are limited by instrumental time resolution. The excitation wavelength is 400 nm.*

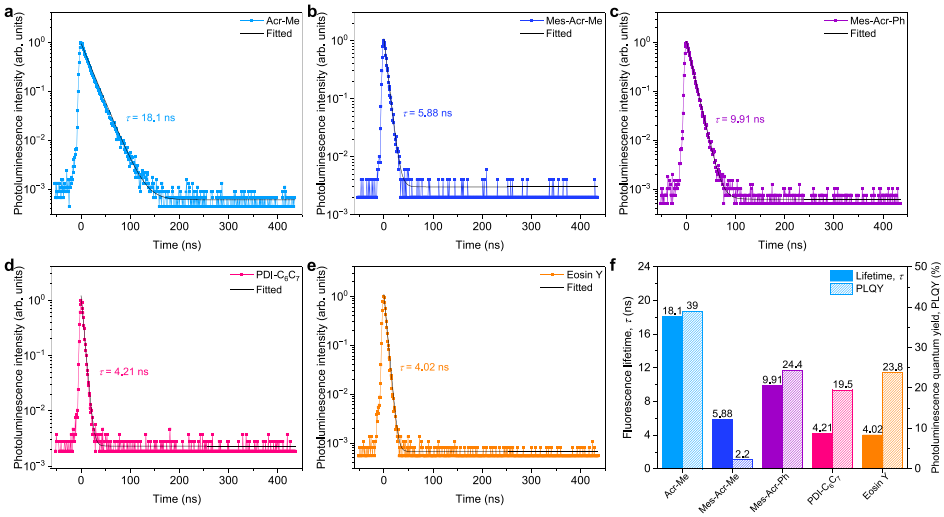

*Figure C.3 Fluorescence lifetime. **a-e,** Time-resolved photoluminescence spectra of Acr-Me (**a**), Mes-Acr-Me (**b**), Mes-Acr-Ph (**c**), PDI-C$_6$C$_7$ (**d**), and Eosin Y (**e**) in solution (BuOAc:CH$_3$CN = 3:1) with LiTFSI (0.1 mol L^{-1}). **f,** Fluorescence lifetime and photoluminescence quantum yield (PLQY)of the above photocatalysts. The excitation wavelength is 400 nm.*

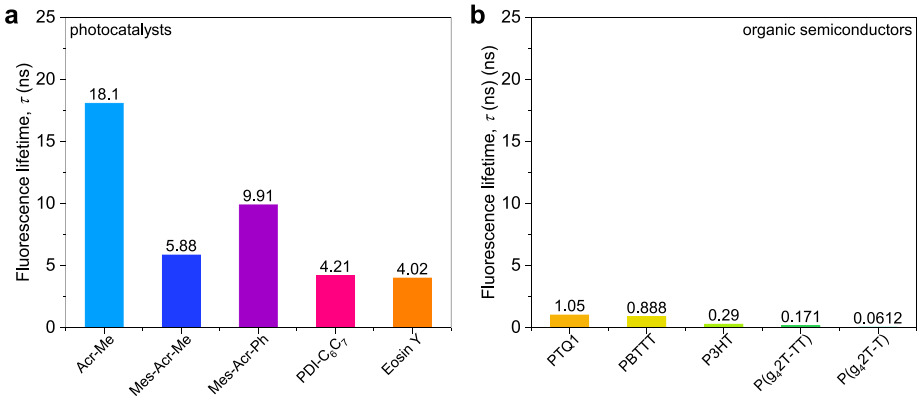

*Figure C.4 Fluorescence lifetime. **a-b**, Fluorescence lifetime of photocatalysts (**a**) and organic semiconductors (**b**). The excitation wavelength is 400 nm.*

Fluorescence lifetimes of photocatalysts are much longer than that of organic semiconductors.

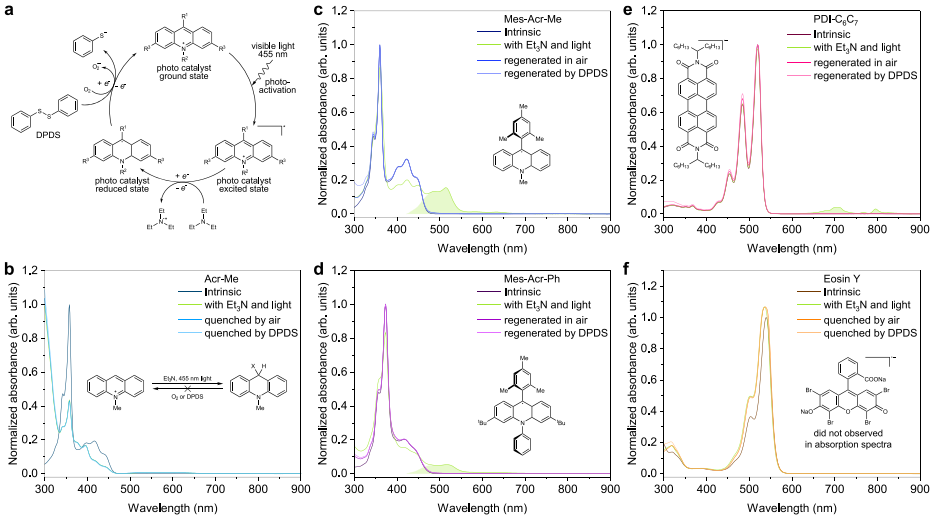

Figure C.5 Photocatalyst reduction and regeneration. ***a,*** *Schematic diagram for photocatalyst reduction by optically transparent triethylamine (2 equivalent) and oxidation regeneration by oxygen or DPDS.* ***b-f,*** *Absorption spectra of the intrinsic photocatalysts, treated with 455 nm light/triethylamine, and quenched (regenerated) by air or DPDS for Acr-Me (**b**), Mes-Acr-Me (**c**), Mes-Acr-Ph (**d**), PDI-C6C7 (**e**), and Eosin Y (**f**). Acr-Me might form irreversible addition products with triethylamine due to the absence of steric protecting group. Reduction form of Eosin Y was not observed in absorption spectra. The slightly changes might cause by soulvent environmental changes. Mes-Acr-Me, Mes-Acr-Ph and PDI-C6C7 show clear reduced states with triethylamine and oxidative regeneration ability.*

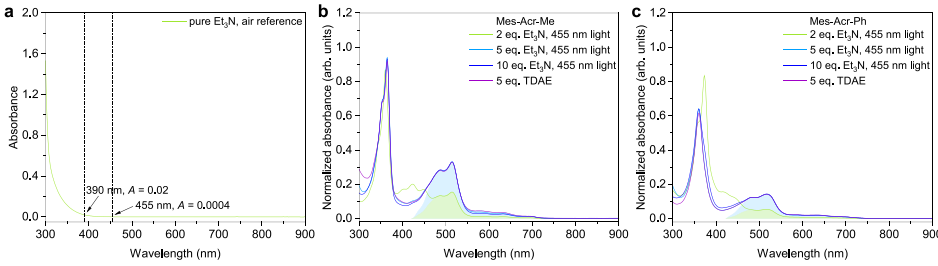

Figure C.6 Photocatalyst reduction. ***a,*** *Absorption spectra of triethylamine, showing its optical transparency at 455 nm or 390 nm.* ***b-c****, Absorption spectra of reduced state Mes-Acr-Me (**b**) and Mes-Acr-Ph (**c**), photoreduced by 2-10 equivalent of triethylamine or reduced by strong reductant tetrakis(dimethylamino)ethylene (TDAE). 5-10 equivalent of triethylamine*

can fully convert Mes-Acr-Me or Mes-Acr-Ph to their reduced states through photoreduction.

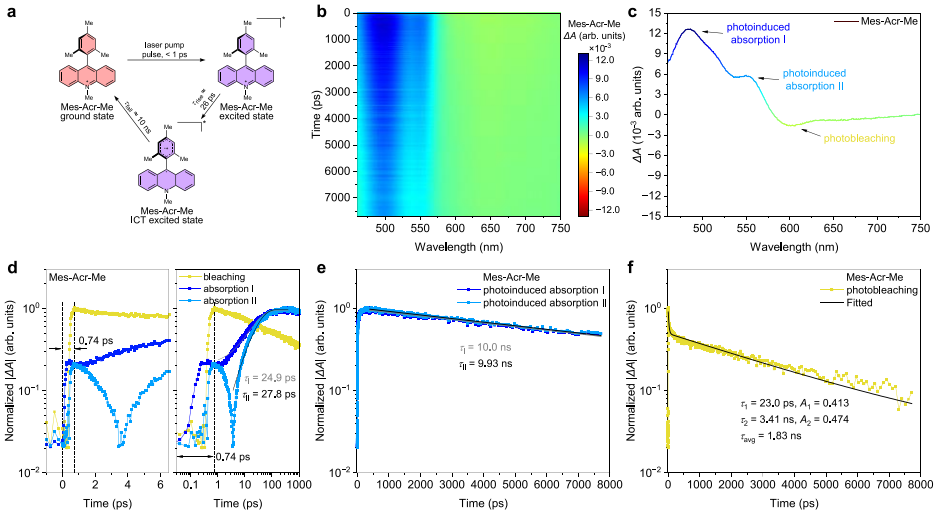

Figure C.7 TAS of Mes-Acr-Me reduction. ***a,*** *Schematic diagram of the transition of ground state, excited state, and intramolecular charge-transfer (ICT) excited state of Mes-Acr-Me, under 390 nm laser pump pulse.* ***b,*** *False color representation of the transient absorption spectra of Mes-Acr-Me solution (0.01 M, with 0.1 M of LiTFSI, in BuOAc:CH_3CN = 3:1) as a function of delay time and detector wavelength.* ***c****, Transient absorption spectra of Acr-Me showing the photobleaching (peak center 601 nm) and two significant photoinduced absorption peaks (I, 484 nm; II, 549 nm).* ***d.*** *Time-dependent photobleaching and photoinduced absorption of Mes-Acr-Me, showing immediate raising (< 1 ps, limited by instrumental time resolution,) for photobleaching, and immediate raising, slow falling, and slower again raising (raising time ~ 26 ps), indicating the ICT excited state formation.* ***e,*** *Time-dependent photoinduced absorption of Mes-Acr-Me, showing long excited life time of 10 ns.* ***f****, Time-dependent photobleaching of Mes-Acr-Me, showing photobleaching time constant of 1.8 ns.*

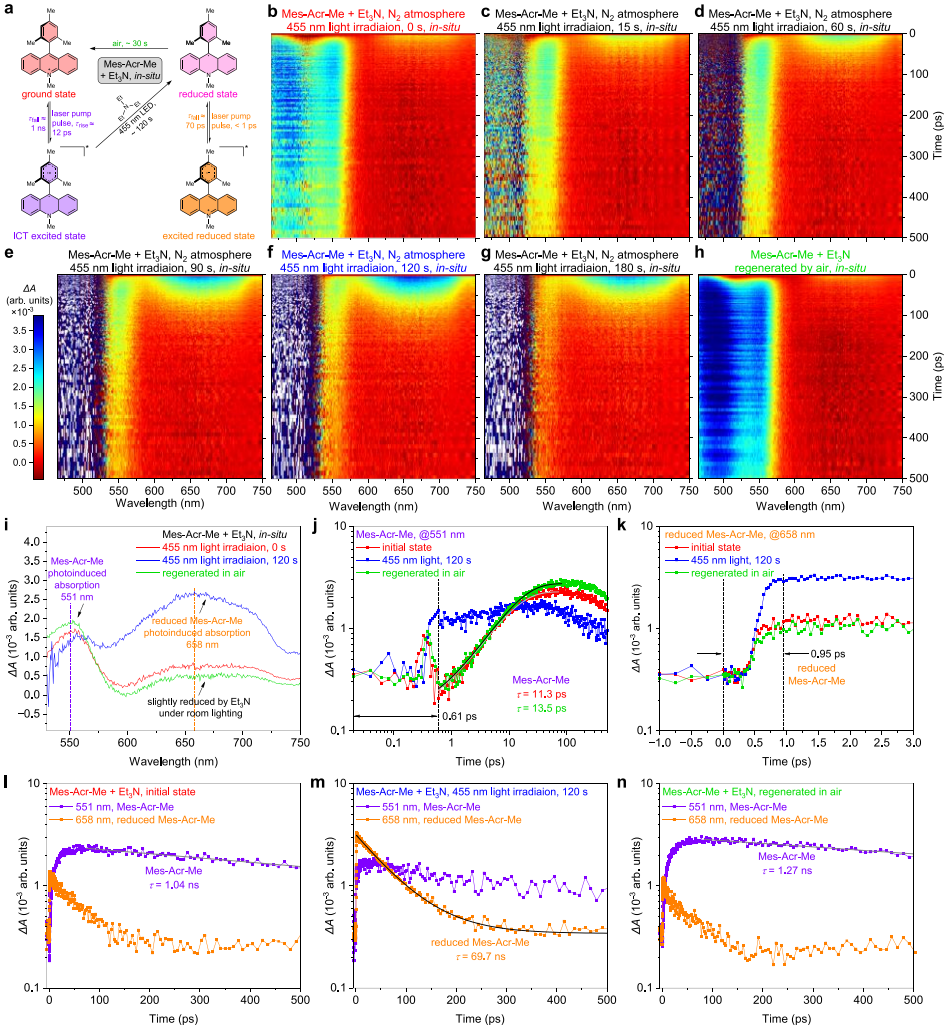

Figure C.8 In-situ TAS of Mes-Acr-Me/Et_3N. ***a,*** *Schematic diagram of the transition of ground state, excited state, reduced state and excited reduced state of Mes-Acr-Me.* ***b-h****, False color representation of the in-situ transient absorption spectra of Mes-Acr-Me solution (0.01 M, with 0.1 M of Et_3N, 0.1 M of LiTFSI, in BuOAc:CH_3CN = 3:1) as a function of delay time and detector wavelength, with different 455 nm light irradiation time: initial state 0 s (**b**), 15 s (**c**), 60 s (**d**), 90 s (**e**), 120 s (**f**), 180 s (**g**), and regenerated in air (**h**). The transient absorption spectra show two strong photoinduced absorption peaks (477 nm, 551 nm) in the initial and regenerated Mes-Acr-Me, presenting the ICT excited state of Mes-Acr-Me. A clear new photoinduced absorption peak at 658 nm, presenting the excited state of reduced Mes-Acr-Me. The transient absorption spectra almost completed recovered to the initial state after expose in air, suggesting the regeneration of Mes-Acr-Me by air oxidation.* ***i****, In-situ transient absorption spectra of the*

Mes-Acr-Me/Et_3N solution in initial state, after 455 nm light irradiation time of 120 s, and regenerated in air. The transient absorption spectra present the formation of reduced state and excited reduced state of Mes-Acr-Me, and regeneration of Mes-Acr-Me by air oxidation. ***j-k.*** *Time-dependent photoinduced absorption, showing similar features in initial and regenerated states of Mes-Acr-Me/Et_3N solution, indicating the same ICT excited state formation of Mes-Acr-Me (See Fig. 4.7).* ***l-n****, Time-dependent photoinduced absorption of Mes-Acr-Me/Et_3N solution after 455 nm light irradiation time of 0 s (**l**) and 120 s (**m**), and regenerated in air (**n**), demonstrating the excited life time of Mes-Acr-Me is ~1 ns (in the presence of 10 equivalent of Et_3N), and excited life time of reduced Mes-Acr-Me is 70 ps.*

Chapter 5

Solution-processed CuI as hole transport layer for improved efficiency and stability of Sn-Pb perovskite solar cells

Mixed tin-lead (Sn-Pb) perovskites are considered the next big thing in perovskite photovoltaics because of their optimal band gap both for single junction and for tandem devices. Generally this devices are fabricated in the p-i-n structure using PEDOT:PSS as the hole transport layer (HTL), which is far to be an ideal hole transport layer for the ionic metal halide perovskites.

This chapter presents the application of solution-processed, undoped copper iodide (CuI) to replace PEDOT:PSS in the device architecture. By using $EACl_{0.015}Cs_{0.25}FA_{0.75}Sn_{0.5}Pb_{0.5}I_3$ *as the active layer we obtained a remarkable short circuit current of 32,85 mA/cm² for a record power conversion efficiency of 20.1%, while control devices using PEDOT:PSS as HTL an efficiency of 19,03% with a* J_{sc} *of 30.59 mA/cm⁻² was obtained. In addition, the implemented CuI layer improved the device stability when stored in* N_2 *and under thermal stress conditions.*

This chapter is based on the publication:
***R. Pau**, M. Pitaro, L. Di Mario, Q. Feng, M. Saba and M.A.Loi, Manuscript in preparation.*

5.1 Introduction

Over recent years, the remarkable advancement in power conversion efficiency of metal halide perovskites (MHP) in single junction solar cells has been accompanied by a growing apprehension regarding their environmental impact[1]. This concern primarily arises from the significant presence of water-soluble lead in the active material. To confront this challenge, tin (Sn)-based and mixed tin-lead (Sn-Pb) perovskites are sturdily emerging as promising substitutes for the extensively researched lead (Pb)-based perovskites, and furthermore, due to their smaller bandgap, they have a possible application in all-perovskite tandem devices with an efficiency expected to overcome 30%[2].

However, this thriving solution presents new obstacles to surmount, such as the introduction of intrinsic Sn-defects and the Sn(II) oxidation to Sn(IV), both of which contribute to the ongoing challenge of achieving competitive photovoltaic performances, that still remain considerably inferior to those exhibited by Pb-based perovskites.

The alloying of Sn-based perovskite with Pb is considered as a strategy to overcome partially the difficulties of working with pure Sn, still decreasing the amount of Pb atoms in the active material of 50%. It is reported that the addition of Pb up till 50% stabilizes the perovskite limiting the oxidation of Sn atoms[3,4].

The best Sn-Pb based devices are currently fabricated in the p-i-n planar configuration with PEDOT:PSS (poly(3,4-ethylenedioxythiophene) polystyrene sulfonate) as the most widely used hole transport layer[5]. However, the acidic and hygroscopic nature of this polymer is known to potentially limit the power conversion efficiency (PCE) and reduces the overall device stability over time[6][7].

The choice of the hole transport layer (HTL) is of paramount importance to achieve high performance solar cells, as it determines the charge transport and extraction, energetic alignment, and eventual interface recombination. Also the stability of the solar cell can be strongly influenced by the morphology and the mechanical and chemical properties of these materials[8]. Moreover, foreseeing the commercialization of a perovskite solar cell architectures, the abundance and the cost of a material chosen as HTL have to be accounted for.

In highly efficient p-i-n perovskite solar cells, transparent HTLs allow sunlight to pass through them with minimal light absorption, therefore maximizing the amount of light that reaches the active layer and

impacting directly the overall energy conversion efficiency of the device. This property can additionally facilitate the integration of multiple layers in tandem structures, stacked to harvest different portions of the solar spectrum.
At the current state-of-the-art, there is a limited number of materials that are suitable to replace PEDOT:PSS in Sn-Pb perovskite solar cells. In 2018, Shao et al. [9] demonstrated promising results by employing a pH neutral anionic conjugated polymer with alkylsulfonate side group, PCP-Na, showing improved reproducibility and efficiency compared to PEDOT:PSS.
Another organic material that gathered attention as HTL is poly-[bis(4-phenyl) (2,4,6-trimethylphenyl)amine] (PTAA)[10],but this interest was recently strongly reduced due to the poor reproducibility of devices and its high cost.
In the last years, a new class of promising HTL was introduced in the field, this are self-assembled monolayers (SAMs) based on a carbazole core, that show minimal parasitic absorption and low charge recombination when compared to PEDOT:PSS, but still showing problems due to their hydrophobicity determining issues in scalability and reproducibility of the deposition of perovskite active layers[11][12].
Among inorganic materials, nickel oxide (NiO_x) has been used as HTL in Sn-Pb based devices. While it is characterized by high mobility, low cost and high transparency, issues with the device stability and reproducibility were reported[13,14].
Here we account the introduction of copper iodide (CuI) as HTL in Pb/Sn perovskite devices. Copper iodide (CuI), show high conductivity (>200 S cm^{-1}), a wide bandgap (E_g = 3.1 eV) and optical transparency across the visible spectra[15,16].
Furthermore, considering the earth-abundant and environment friendly composition, CuI is considered a low-cost material suitable for scalable transparent electronics. CuI has been reported as transparent conductor in 1907[17,18], and after that, thin films of this material have been fabricated with a wide range of techniques, such as vapor iodization[17], sputtering[15], pulsed laser deposition[19], liquid iodination[20] and solution depositions[21–23]. Furthermore, various doping approaches have been reported in order to enhance the electrical properties of CuI[15,20,24].

Solution processing is a well-established simple, reliable and low-cost method to introduce CuI as HTL in solar cells. A few early reports showed applications of CuI HTL in Pb-based perovskite solar cells, resulting in higher efficiency and improved device stability[25,26].

Nevertheless, CuI was never investigated in Sn-based and mixed Sn-Pb systems. Here we present the application of an undoped CuI as hole transport layer deposited from solution for the fabrication of methylammonium (MA)-free half Sn-half Pb perovskite solar cells. Champion device using CuI as HTL reached 20.1% of power conversion efficiency (PCE) with a remarkable short-circuit current (J_{sc}) of 32,85 mA/cm^{-2}, while the champion reference device using PEDOT:PSS exhibited a PCE of 19,03% with a J_{sc} of 30.59 mA/cm^{-2}. Along with this improvement, we report an enhanced device stability when stored in N_2 and under thermal stress conditions.

5.2 Results and discussion

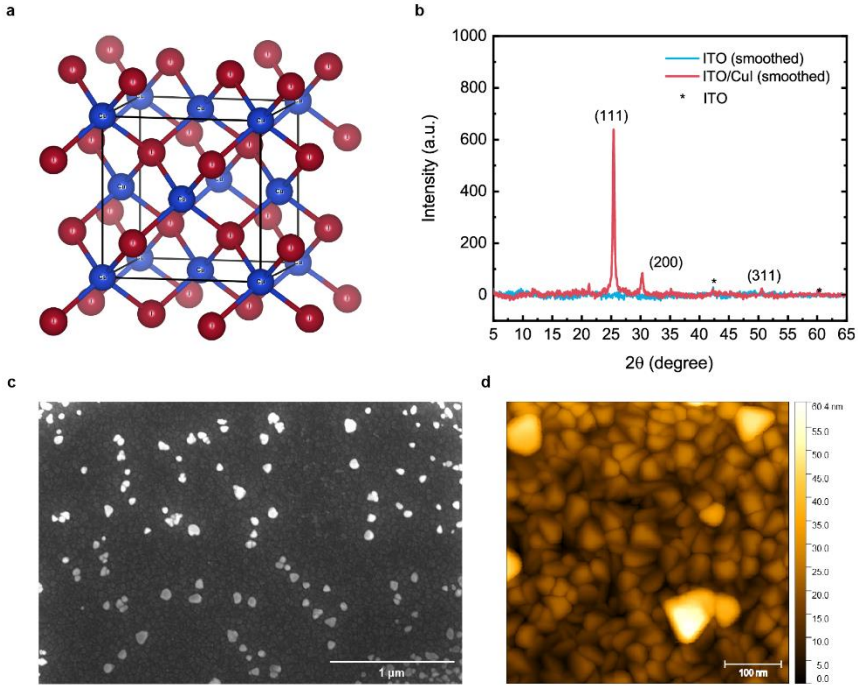

Figure 5.1 (a) Schematic representation of the crystal structure of CuI. Cu and I atoms are represented in blue and red, respectively. (b) X-ray diffraction (XRD) pattern of CuI deposited on ITO patterned glass substrates (red) and of the reference ITO patterned glass substrate (blue). (c) SEM image of CuI film. (d) AFM image of CuI film.

Figure 5.1a displays the crystal structure of the copper(I) iodide (CuI) that is the object of this work.
Figure 5.1b shows a spin-coated CuI thin film X-ray diffraction (XRD) pattern. The most intense diffraction peak, located at 2θ=25.4°, suggests the growth of the material in the typical γ-phase, alongside the (111)-orientation[15,27].
The corresponding scanning electron microscope (SEM) and atomic force microscope (AFM) images in figures 5.1c and 5.1d, respectively, show the morphology of the solution-processed CuI film. The thin films appear as polycrystalline with grain size in the order of 30 nm, with a surface texture of small islands of material. According to the AFM data, CuI film surface has a root-mean-square (RMS) roughness of of <9 nm.

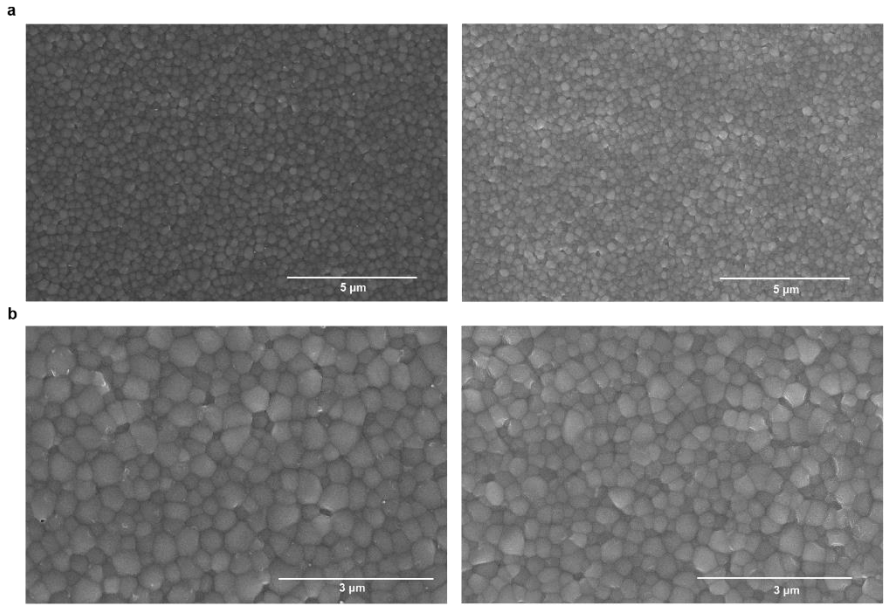

Figure 5.2 SEM images of $EACl_{0.015}Cs_{0.25}FA_{0.75}Sn_{0.5}Pb_{0.5}I_3$ perovskite films deposited on top of PEDOT:PSS (left) and CuI (right) at 5 microns (a) and 3 microns (b) magnifications.

The growth of the perovskite layer on top of CuI was studied through SEM imaging. The morphological results are reported in figure 5.2, in comparison with the one of the perovskite growth on PEDOT:PSS. Slightly bigger perovskite grains, with an average of around 400 nm are observed when the active layer is deposited on PEDOT:PSS while the grains are of about 300 nm on top of CuI. However, the perovskite formed on top of PEDOT:PSS, as was reported earlier[9,28], presents a

higher number of pinholes located near the grain boundaries with respect to the perovskite on top of CuI. Such growth defects have been suggested to be the cause of undesired non-radiative recombination through the device (vide infra).
Steady-state and time-resolved photoluminescence (PL) measurements were performed to further investigate the physical properties of the perovskite layer on top of the two HTLs (Figure D.2-3). Comparing the two spectra, we can observe a slight redshift of the CuI/perovskite film with respect to the PEDOT:PSS/perovskite one, which indicates a lower doping level of the first. The higher PL intensity observed in steady-state PL and the longer decay time observed in time-resolved PL, for the sample deposited on CuI are further proof of a less-defective interface with the perovskite. It is important to notice that measurements were performed from the side of the substrate, meaning that considering the very high absorption coefficient of the perovskite the 400 nm excitation is absorbed in less than 100 nm at the interface with the HTL. Therefore, the PL and time resolved PL measurements do not only probe the quality of the perovskite but also an eventual charge transfer to the HTL or the interaction with defects at that interface.
Solar cells with p-i-n architecture as schematically represented in figure 5.3a and using as active layer $EACl_{0.015}Cs_{0.25}FA_{0.75}Sn_{0.5}Pb_{0.5}I_3$ were fabricated.

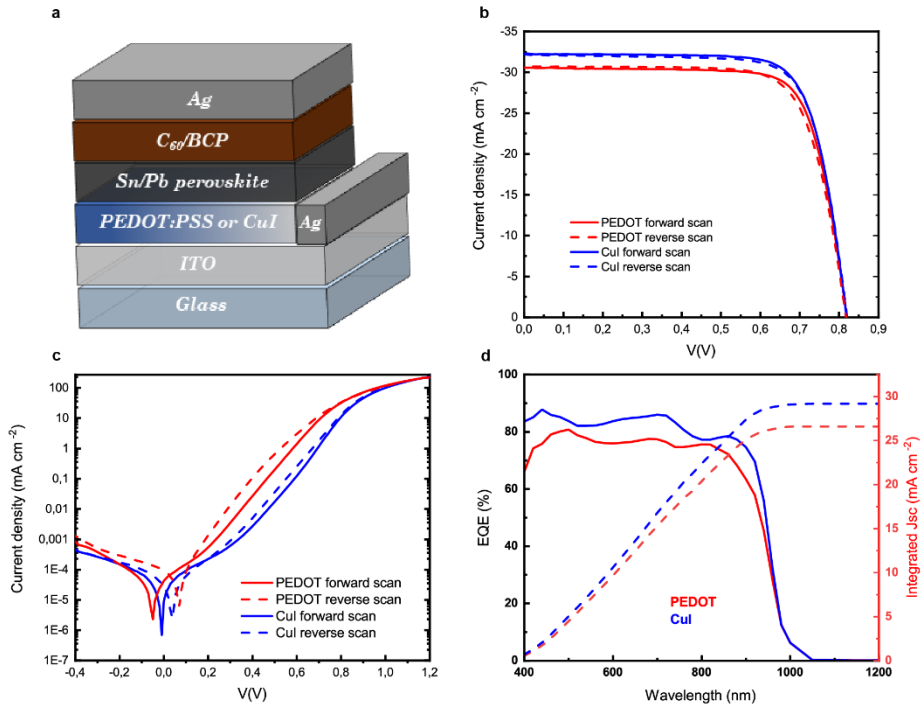

Figure 5.3 (a) Device structure of the fabricated p-i-n perovskite solar cell, (b) current density-voltage (J-V) and (c) dark J-V curves of perovskite solar cells fabricated by using PEDOT:PSS (red) and CuI (blue) as HTLs. (d) External quantum efficiency (EQE) as a function of the wavelength and integrated current of the two different structures used.

Figures 5.3b shows the JV characteristics under AM1.5 illumination conditions for the champion devices in the two cases under study. The champion reference device, using PEDOT:PSS as HTL exhibits a power conversion efficiency (PCE) of 19,03%, with a short-circuit current (J_{sc}) of 30.59 mA/cm^{-2}, an open-circuit voltage (V_{oc}) of 0,82 V and a fill factor (FF) of 0.76. While devices using copper iodide as HTL, show a significant improvement in power conversion efficiency, with the device reaching a PCE of 20,10%, with a Jsc of 32,85 mA/cm^{-2}, a Voc of 0,81 V and a FF of 0,75. The remarkable efficiency improvement is determined by the higher current achieved with slightly lower open circuit voltage and FF.

To further investigate this improvement, we analyzed the JV characteristics in dark conditions for the two device architectures. The device fabricated on CuI presents a lower dark current density, that can be linked with a lower leakage due to the reduced density of

pinholes in the active material. In addition, the CuI sample presents a lower hysteresis between the forward and the reverse scan, also in agreement with the above-mentioned higher quality of the active layer and lower number of trap states. The external quantum efficiency (EQE) measurements in Fig. 5.3d confirm the current increase in the sample using CuI as HTL with respect to the one using PEDOT:PSS.

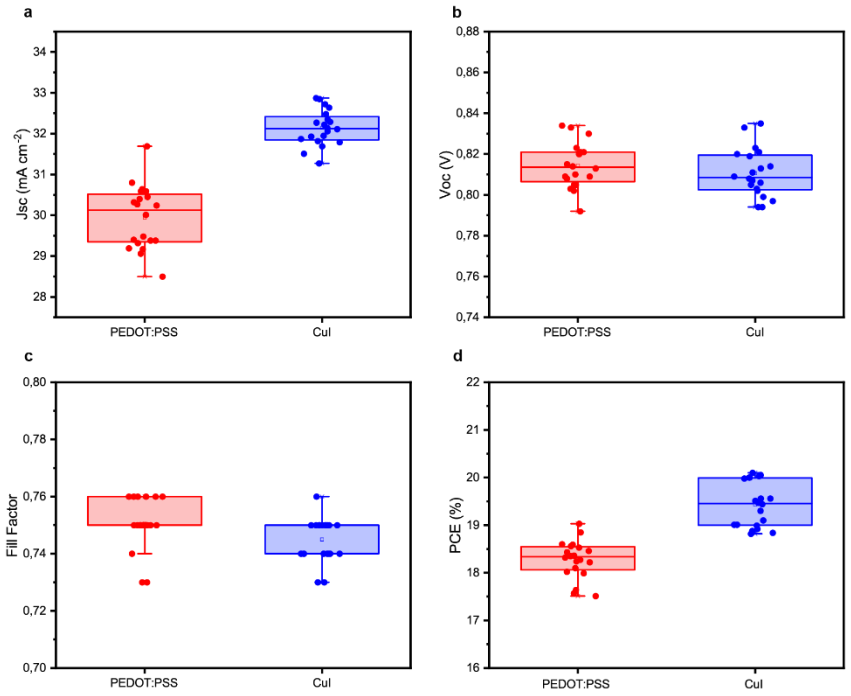

Figure 5.4 Distribution of the photovoltaic parameters derived from the JV scans for the PEDOT:PSS (red) and CuI (blue) devices (the statistical overview is given on 20 samples fabricated for every condition): (a) Jsc, (b) Voc, (c) FF and (d) PCE.

The statistical distribution of photovoltaic parameters over 20 devices per type, presented in figure 5.4, shows the good reproducibility of the perovskite solar cells under investigation and corroborates the trend exhibited by the two champion devices. The calculated average PCE of devices fabricated on PEDOT:PSS is 18.3±0.4% while for the one fabricated on CuI it is 19.4±0.5%. The drastic improvement in short-circuit current, which goes from 29.9±0.8 mA/cm^{-2} for the reference device to 32.1±0.4 mA/cm^{-2} for devices using CuI as HTL clearly is the main responsible for the higher PCE obtained using copper iodide.

Within the batch, the average Voc for the reference devices and for the one using CuI are equal to (0.814±0.010) V and (0.811±0.012) V, respectively, with a minor difference that lies inside the statistical error and therefore is not considered significative (figure 5.4b). A similar trend is observed for the FF, where we have a slight drop, from 0.751±0.009 to 0,750±0.008 from the reference device to the one fabricated on CuI (figure 5.4c), respectively. Difference that also in this case does not appear statistically relevant.

The charge recombination was further investigated with impedance spectroscopy under open-circuit and dark conditions (Fig. D.4a). PEDOT: PSS-based devices presented two semicircles fitted by two RC components, as shown in Fig. D.5. The low-frequency arch describes recombination at the PEDOT:PSS/perovskite interface and the presence of moving ions. The larger high-frequency semicircle is related to the recombination that occurs in the perovskite bulk[29]. Specifically, the high-frequency semicircle for both CuI and PEDOT: PSS-based solar cells has been fitted with two RC elements: the first RC element (CPE_1-R_2) describes recombination in the perovskite layer, while the second RC element (C_3-R_3) is related to the surface charge accumulation at the HTL/perovskite or ETL/perovskite interfaces[30,31]. Interestingly, CuI-based devices exhibit only the high-frequency arch indicating a widely reduced ionic motion.
Mott–Schottky analysis (Figure D.4b) reveals a decrease in background charge-carrier density from 8.52×10^{15} cm^{-3} for PEDOT:PSS to 6.83×10^{15} cm^{-3} for CuI-based solar cells. The background charge-carrier density is mainly caused by self p-doping due to Sn^{2+} oxidation, which generates Sn vacancies. The reduced background charge-carrier density could be one of the reasons for the increased J_{SC}[32].

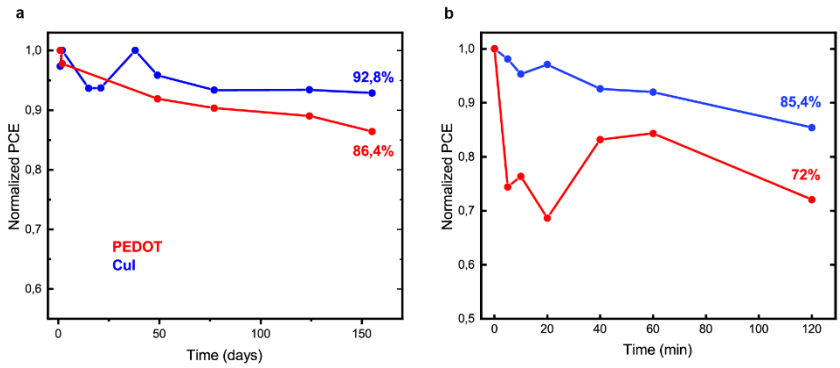

Figure 5.5 (a) Shelf-life stability data for unencapsulated devices using PEDOT:PSS (red) and CuI (blue) as HTL, devices where stored in N_2 atmosphere and dark conditions. The maximum efficiencies in the plot are 17,69 and 20,03% for the reference device and the one on CuI, respectively. (b) High temperature stability (85°C in N_2 atmosphere) PCE data for the unencapsulated reference device (red) and the one using CuI HTL (blue).

In the choice of the HTL in perovskite solar cells, alongside performances, the device stability plays a key role; taking into consideration the critical issues related to PEDOT:PSS described previously, it appears of fundamental importance to test the stability of devices using CuI as HTL. Therefore, we investigated the stability of the two different solar cells, looking at their storage lifetime and their stability under high-temperature stress.

As reported in figure 5.5a we tracked the shelf-life stability in N_2 conditions for the two devices. The one using CuI as HTL retained 92.8% of its efficiency after 155 days of testing, while the device using PEDOT:PSS as HTL exhibits an higher decay slope reaching after the same number of days 86,4% of the initial power conversion efficiency .

In figure 5.5b is reported the high temperature stress test executed on the devices at 85°C in an N_2-filled glovebox. Also this experiment shows a better stability for the CuI HTL, that maintained 85.4% of its initial PCE after 120 minutes versus the 72% displayed by the reference device.

5.3 Conclusions

In this work we compared the use of PEDOT:PSS with a solution-processed CuI as hole-transport in Sn/Pb perovskite solar cell using $EACl_{0.015}Cs_{0.25}FA_{0.75}Sn_{0.5}Pb_{0.5}I_3$ as the active layer. By using copper iodide we obtained a remarkable short circuit current of 32,85 mA/cm^2 and a power conversion efficiency of 20.1% for the champion device, without the implementation of any CuI doping or anti-reflective coating layer in the device architecture. Moreover, an overall more stable structure is obtained, as proved via shelf-lifetime and thermal stability investigation. In detail, of the CuI HTL devices retain 92.8% of their initial efficiency after 155 days of storage in a N_2-filled glovebox.
In conclusion, we believe that in the future by using a CuI of higher conducibility obtained for example by dry deposition methods or by doping, even higher efficiencies could be obtained with Pb/Sn based perovskites.

5.4 Experimental Section

5.4.1 Materials

Custom patterned ITO substrates (30x30 mm^2) were directly purchased. Poly(3,4-ethylenedioxythiophene) polystyrene sulfonate (PEDOT:PSS) in a water dispersion (Clevios VP Al 4083) was purchased from Heraeus. Formamidinium iodide (FAI, >98%), Ethylamine Hydrochloride (>98%) and bathocuproine (BCP, >99%) were bought from TCI EUROPE N. V. Tin(II) iodide (SnI_2, 99.99%), tin(II) fluoride (SnF_2, 99%), cesium iodide (CsI, 99.999%), dimethylformamide (DMF,99.8%), anisole (anhydrous, 99.7%), Copper (I) iodide (CuI, 99.995%), 2,2,2-Trifluoroethanol (TFE, >99%), Sodium fluoride (NaF, >99%) and buckminsterfullerene (C60, 99.9%) were supplied from Sigma Aldrich. Lead(II) iodide (PbI_2, 99.999%), Di-n-propyl sulfide (>98%) and dimethyl sulfoxide (DMSO, 99.8+%) were acquired from Alfa Aesar/Thermo Scientific. Ag, (99.99%) was purchased from Umicore.

5.4.2 Device fabrication

The ITO patterned glasses were cleaned using soapy water and then sonicated in water, acetone and 2-propanol. After oven-drying at 140°C for 30 min, the substrates were treated with UV-Ozone for 30 min and after that, ready for the HTL deposition.
The CuI solution was prepared with a concentration of 10 mg/mL in propyl sulfide. CuI was deposited on ITO in N_2-filled glovebox, with a spin coating process at 3000 rpm for 30 s and annealed at 100°C for 3 min. Commercial PEDOT:PSS dispersion was spin-coated at 3000 rpm for 60 s and annealed at 140°C for 20 min in air.
The perovskite precursor solution with concentration 1.4M was prepared by dissolving EACl (0.021 mmol), SnI_2 (0.7 mmol), FAI (1.05 mmol), CsI (0.35 mmol), SnI_2 (0.7 mmol), PbI_2 (0.7 mmol) and SnF_2 (0.07 mmol) in 800 ml of DMF and 200 ml of DMSO (4:1 ratio). The solution was left under stirring for 3 hours (room temperature) and then filtered using 0.2 mm pore size PTFE membrane filters. Next, the perovskite solution was spin coated on ITO/HTLs substrates at 4000 rpm for 70 s in a N_2-filled glovebox with O_2 and H_2O concentrations of <0.1 ppm. Anisole (250 ml) was used as the antisolvent and dropped 25 s after the start of the spin coating program. The perovskite films were annealed at 120 °C for 10 min, immediately at the end of the spin coating deposition. The obtained $EACl_{0.015}Cs_{0.25}FA_{0.75}Sn_{0.5}Pb_{0.5}I_3$ films were passivated with sodium fluoride (NaF) via spin-coating at 2000 rpm for 30 s and annealed on a hotplate at 85°C for 5 min.
After that, the samples were moved to a vacuum chamber where 60 nm of C60 and 6 nm of BCP were thermally evaporated at pressures in the order of 10^7 mbar. Finally, 100 nm of Ag were evaporated on top of BCP layer as the metal contact.

5.4.3 Film and device characterization

X-ray diffraction (XRD) patterns were acquired on CuI films without encapsulation in air using a Bruker D8 Advance X-ray diffractometer with a Cu Ka source (l = 1.54 Å) and a Lynxeye detector. Scanning electron microscopy (SEM) imaging was performed using a Nova NanoSEM 650 with an acceleration voltage of 5 kV. Atomic force microscopy (AFM) of the CuI morphology was performed using a Bruker Multimode 8 microscope with ScanAsyst air probes (resonant frequency 70 kHz and spring constant 0.4 N m^{-1}). The AFM images were recorded using a scan rate of 0.912 Hz with a resolution of 1024 samples per line.

Steady-state and time-resolved photoluminescence (PL) measurements were performed in reflection geometry, exciting the samples from the back side of the ITO/HTL/perovskite film (glass ITO side). An excitation wavelength of 400 nm was obtained as second harmonic of a mode-locked Ti:sapphire laser (Coherent Mira 900). The laser repetition rate of 76 MHz was reduced through an optical pulse picker to extend the time range in the time-resolved measurements. Steady-state spectra were acquired using a Hamamatsu spectral calibrated EM-CCD camera. Time-resolved PL traces were taken with a Hamamatsu streak camera working in a single-sweep mode. The samples were mounted in a sealed sample holder and kept in N_2 atmosphere during the measurements.
The absorption spectrum of the ITO/HTL films was acquired using a Shimatzu UV-vis-NIR spectrophotometer (UV 3600).

The J–V characteristics of the solar cells were measured in a nitrogen-filled glovebox (O_2< 0.1 ppm and H_2O < 0.1 ppm) under standard test condition (295K, AM1.5G solar illumination) using a Keithley 2400 source meter and a Steuernagel Solar constant 1200 metal halide lamp. The system was calibrated using a Si reference cell. A shadow mask (0.04 cm^2) was used to exclude contributions outside the device area. A home-built setup was used for measuring the external quantum efficiency (EQE) of the solar cells, in which a set of filter wheels allowed measurements in the spectral range of 400-1400 nm. The samples were mounted in a sealed sample holder and kept in N_2 atmosphere during the measurements.
The photocurrent was measured using a lock-in amplifier (Stanford Research Systems, Model SR830 DSP Lock-In Amplifier). To calibrate the photon flux, a set of calibrated Newport optical power detectors (Newport Model 818-SL and Model 818-IR) was used.

5.5 References

[1] J. Li, H.-L. Cao, W.-B. Jiao, Q. Wang, M. Wei, I. Cantone, J. Lü, A. Abate, *Nat. Commun.* **2020**, *11*, 310.

[2] T. Leijtens, K. A. Bush, R. Prasanna, M. D. McGehee, *Nat. Energy* **2018**, *3*, 828.

[3] T. Leijtens, R. Prasanna, A. Gold-Parker, M. F. Toney, M. D. McGehee, *ACS Energy Lett.* **2017**, *2*, 2159.

[4] J. Xi, M. A. Loi, *ACS Energy Lett.* **2021**, *6*, 1803.

[5] S. Hu, K. Otsuka, R. Murdey, T. Nakamura, M. A. Truong, T. Yamada, T. Handa, K. Matsuda, K. Nakano, A. Sato, K. Marumoto, K. Tajima, Y. Kanemitsu, A. Wakamiya, *Energy Environ. Sci.* **2022**, 2096.

[6] F. Hou, Z. Su, F. Jin, X. Yan, L. Wang, H. Zhao, J. Zhu, B. Chu, W. Li, *Nanoscale* **2015**, *7*, 9427.

[7] J. C. Yu, J. A. Hong, E. D. Jung, D. Bin Kim, S. M. Baek, S. Lee, S. Cho, S. S. Park, K. J. Choi, M. H. Song, *Sci. Rep.* **2018**, *8*, 3.

[8] V. M. Goldschmidt, *Naturwissenschaften* **1926**, *14*, 477.

[9] S. Shao, Y. Cui, H. Duim, X. Qiu, J. Dong, G. H. ten Brink, G. Portale, R. C. Chiechi, S. Zhang, J. Hou, M. A. Loi, *Adv. Mater.* **2018**, *30*, 1803703.

[10] J. Werner, T. Moot, T. A. Gossett, I. E. Gould, A. F. Palmstrom, E. J. Wolf, C. C. Boyd, M. F. A. M. Van Hest, J. M. Luther, J. J. Berry, M. D. McGehee, *ACS Energy Lett.* **2020**, *5*, 1215.

[11] M. Pitaro, J. S. Alonso, L. Di Mario, D. Garcia Romero, K. Tran, T. Zaharia, M. B. Johansson, E. M. J. Johansson, M. A. Loi, *J. Mater. Chem. A* **2023**, *11*, 11755.

[12] M. Pitaro, J. E. S. Alonso, L. Di Mario, D. G. Romero, K. Tran, J. Kardula, T. Zaharia, M. B. Johansson, E. M. J. Johansson, R. C. Chiechi, M. A. Loi, *Adv. Funct. Mater.* **2023**, *2306571*, 1.

[13] Y. Li, J. J. Ye, A. Medjahed, D. Aldakov, S. Pouget, E. Djurado, L. Xu, P. Reiss, *ACS Appl. Energy Mater.* **2023**, *6*, 1555.

[14] Q. Han, Y. Wei, R. Lin, Z. Fang, K. Xiao, X. Luo, S. Gu, J. Zhu, L. Ding, H. Tan, *Sci. Bull.* **2019**, *64*, 1399.

[15] C. Yang, M. Kneib, M. Lorenz, M. Grundmann, *Proc. Natl. Acad. Sci. U. S. A.* **2016**, *113*, 12929.

[16] A. Liu, H. Zhu, W. T. Park, S. J. Kang, Y. Xu, M. G. Kim, Y. Y. Noh, *Adv. Mater.* **2018**, *30*, 1.

[17] K. Bädeker, *Ann. Phys.* **1907**, *327*, 749.

[18] M. Grundmann, F. L. Schein, M. Lorenz, T. Böntgen, J. Lenzner, H. Von Wenckstern, *Phys. Status Solidi Appl. Mater. Sci.* **2013**, *210*, 1671.

[19] B. L. Zhu, X. Z. Zhao, *Phys. Status Solidi Appl. Mater. Sci.* **2011**, *208*, 91.

[20] K. Ahn, G. H. Kim, S. J. Kim, J. Kim, G. S. Ryu, P. Lee, B. Ryu, J. Y. Cho, Y. H. Kim, J. Kang, H. Kim, Y. Y. Noh, M. G. Kim, *Chem. Mater.* **2022**, *34*, 10517.

[21] K. Zhao, G. O. Ngongang Ndjawa, L. K. Jagadamma, A. El Labban, H. Hu, Q. Wang, R. Li, M. Abdelsamie, P. M. Beaujuge, A. Amassian, *Nano Energy* **2015**, *16*, 458.

[22] C. H. Choi, J. Y. Gorecki, Z. Fang, M. Allen, S. Li, L. Y. Lin, C. C. Cheng, C. H. Chang, *J. Mater. Chem. C* **2016**, *4*, 10309.

[23] S. Inudo, M. Miyake, T. Hirato, *Phys. Status Solidi Appl. Mater. Sci.* **2013**, *210*, 2395.

[24] A. S. Mirza, M. Pols, W. Soltanpoor, S. Tao, G. Brocks, M. Morales-Masis, *Matter* **2023**, *6*, 4306.

[25] W. Y. Chen, L. L. Deng, S. M. Dai, X. Wang, C. B. Tian, X. X. Zhan, S. Y. Xie, R. Bin Huang, L. S. Zheng, *J. Mater. Chem. A* **2015**, *3*, 19353.

[26] W. Sun, S. Ye, H. Rao, Y. Li, Z. Liu, L. Xiao, Z. Chen, Z. Bian, C. Huang, *Nanoscale* **2016**, *8*, 15954.

[27] N. Yamada, R. Ino, Y. Ninomiya, *Chem. Mater.* **2016**, *28*, 4971.

[28] M. Pitaro, J. S. Alonso, L. Di Mario, D. Garcia Romero, K. Tran, T. Zaharia, M. B. Johansson, E. M. J. Johansson, M. A. Loi, *J. Mater. Chem. A* **2023**, *11*, 11755.

[29] E. Von Hauff, D. Klotz, *J. Mater. Chem. C* **2022**, *10*, 742.

[30] I. Zarazúa, S. Sidhik, T. Lopéz-Luke, D. Esparza, E. De La Rosa, J. Reyes-Gomez, I. Mora-Seró, G. Garcia-Belmonte, *J. Phys. Chem. Lett.* **2017**, *8*, 6073.

[31] I. Zarazua, G. Han, P. P. Boix, S. Mhaisalkar, F. Fabregat-Santiago, I. Mora-Seró, J. Bisquert, G. Garcia-Belmonte, *J. Phys. Chem. Lett.* **2016**, *7*, 5105.

[32] M. A. Karim, K. Matsuishi, M. E. Kayesh, Y. He, A. Islam, *ACS Appl. Mater. Interfaces* **2023**, *15*, 45823.

Appendix D: Additional data to Chapter 5

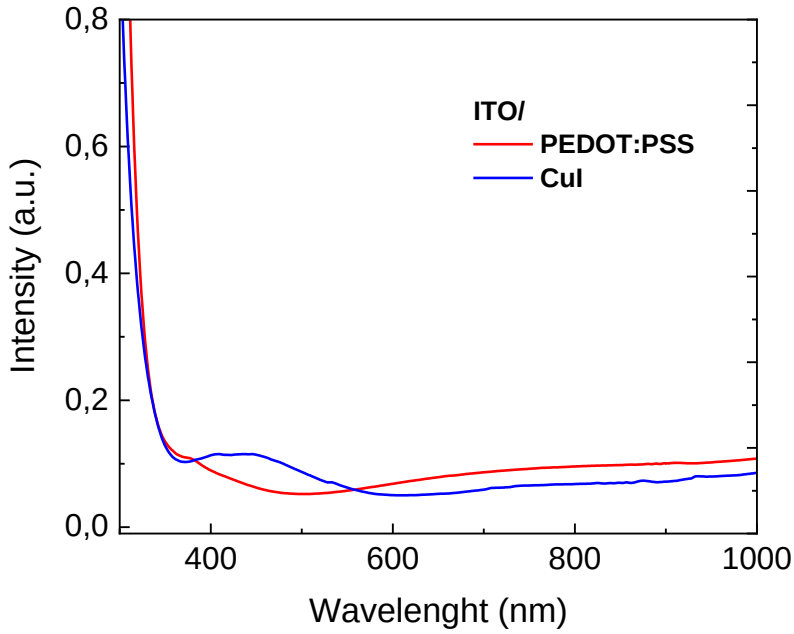

Figure D.1 Absorbance spectra of PEDOT:PSS and CuI coated on ITO substrates.

(a)

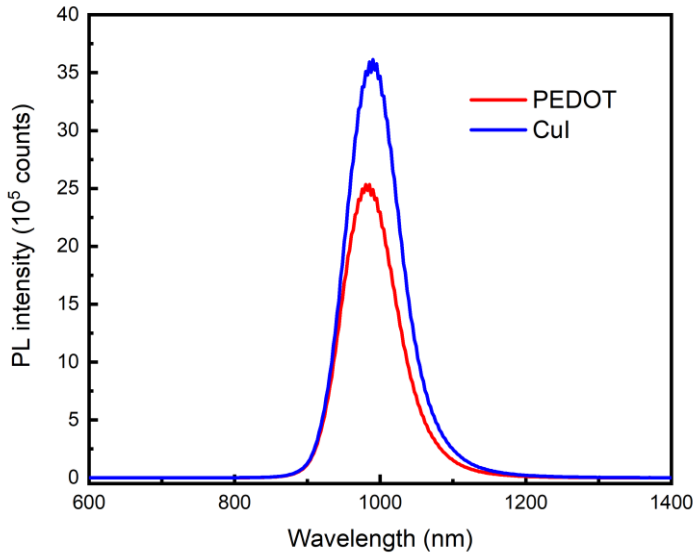

(b)

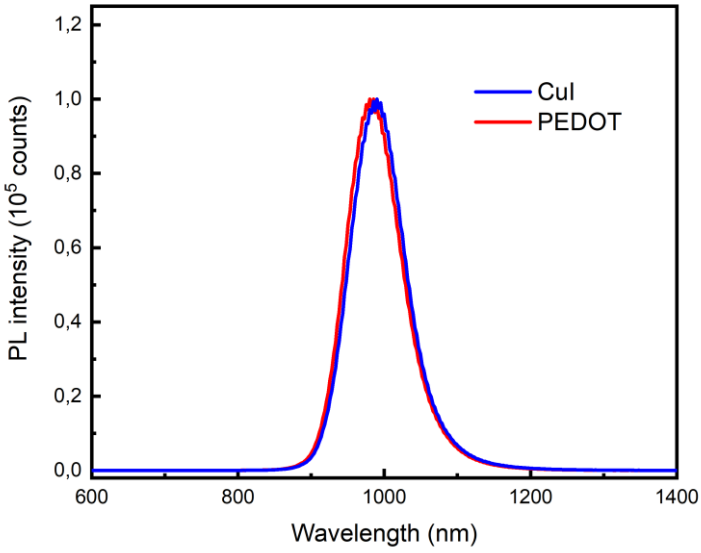

Figure D.2 Absolute (a) and normalized (b) steady-state photoluminescence of the active layer fabricated on top of CuI (blue) and PEDOT:PSS (red).

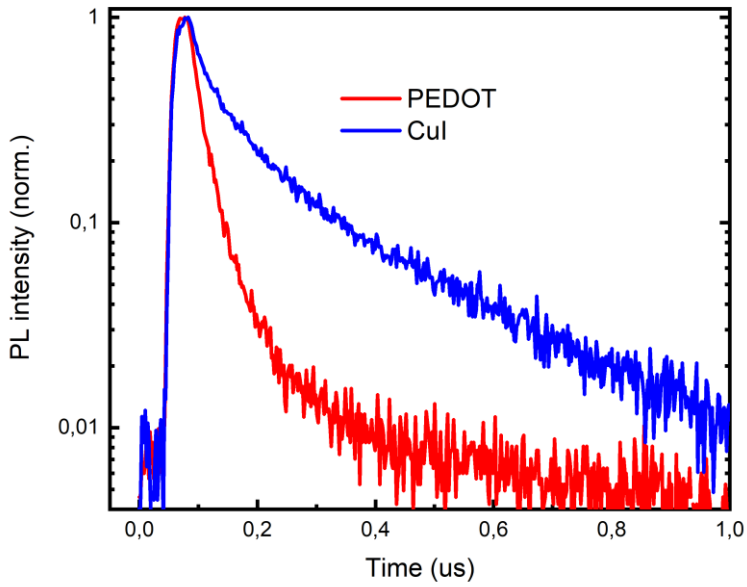

Figure D.3 Time-resolved photoluminescence of the active layer fabricated on top of CuI (blue) and PEDOT:PSS (red).

(a)

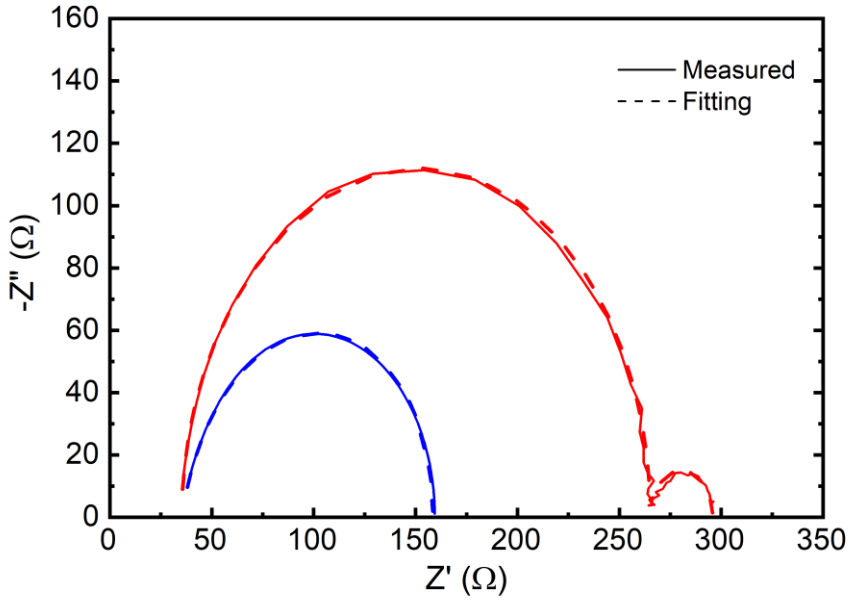

(b)

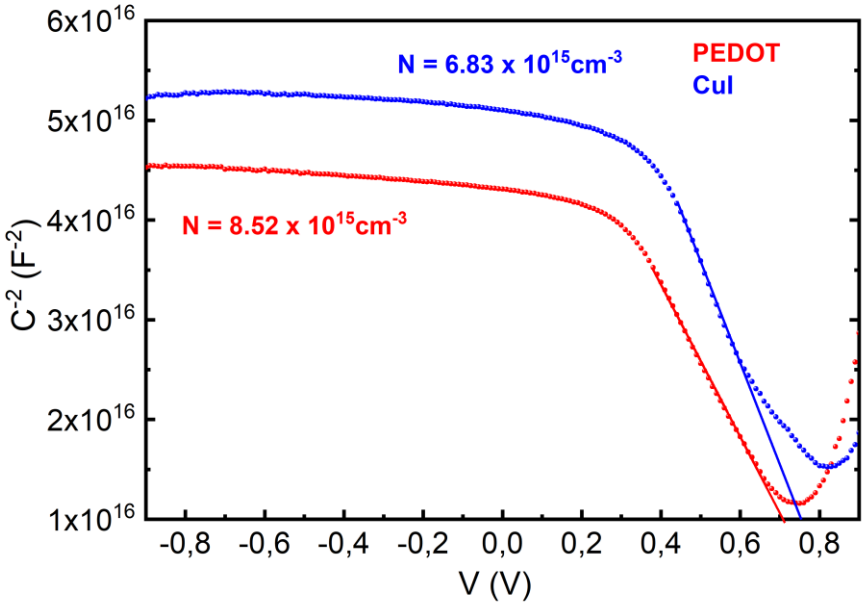

Figure D.4 (a) Impedance spectroscopy and (b) Mott-Schottky analysis for PEDOT:PSS (red curve) and CuI (blue curve) based devices.

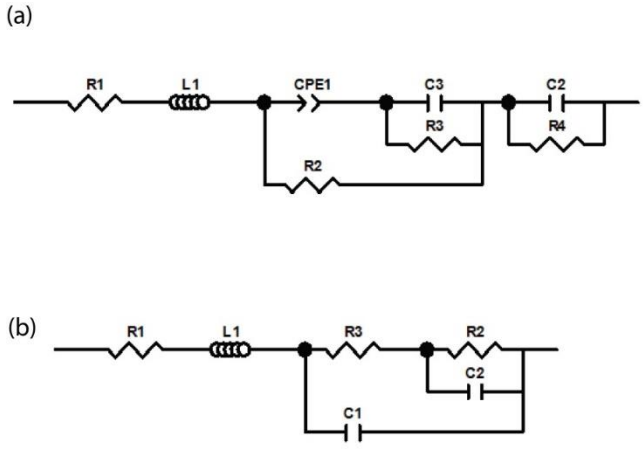

Figure D.5 Equivalent circuit used to fit the impedance spectroscopy experimental data performed on PEDOT:PSS (a) and CuI (b) devices.

Summary

In the foreseeable future, the energy demand is expected to keep growing steadily. Solar energy has the potential to significantly contribute solving this problem as a clean, copious and renewable energy source.
Although conventional solar cells have a well-established manufacturing process with relatively high power conversion efficiency, the high performance modules require an expensive fabrication that involves high temperature steps and high purity of the starting semiconductor, both contributing to the large carbon-foot-print of the technology.
Because of that, scientists have an important role in the process of innovating the energy strategy, finding new materials and new concepts for next generation devices.
In this path of research for novel semiconductors with easy processing, low costs and appealing optoelectronic properties, the discovery of hybrid metal halide perovskites gave rise to a new enthusiasm within the research field. Metal Halide perovskites possess a unique set of properties, from the high absorption coefficient, the tunable bandgap and the high mobility to long range diffusion length. Impressive performances in photovoltaic applications, light-emitting diodes, lasers and photodetectors have shown the potential of this solution processable semiconductors for future applications.
Despite these outstanding properties, as their investigation started relatively recently, a lot more effort is needed to promote perovskites from the lab-scale research to the actual commercialization. Among the major issues that need to be addressed, are the presence of lead, and their general fragility which is determine by the nature of the chemical bonds. Additionally, the power conversion efficiencies, when we speak of panels, are still far from their theoretical limit.
To further advance towards the technological application of metal halide perovskites more work is needed, spacing from the search for less environmentally-impactful materials, the chemical and device engineering to a deeper understanding of their physical properties.

This thesis focuses on the understanding of the photophysics and optoelectronic properties of organic-inorganic metal halide perovskites and their application in solar cells.

A precise investigation on the fundamental properties of metal halide perovskite is key in the process of optimization of the devices.
In **Chapter 2**, the role of excitons, free charged carriers and polarons in hybrid metal halide perovskite has been investigated by using a ultrafast tandem spectroscopy technique. This technique combines successfully time-resolved photoluminescence and differential transmission, pump-probe spectroscopy. These two techniques are complementary, providing a different set of information about optical excitations in the sample material. In this work, various hybrid perovskites were investigated, from 3D compositions wide-used in the photovoltaic and light-emitting diodes to 2D archetypes of Ruddlesden-Popper 2D layered halide perovskites. In the analysis, the PL and differential transmission transients have been quantitatively compared, with the same excitation conditions for every sample, by setup construction. The results obtained indicate the formation of large polarons, charge carriers coupled to lattice deformations, in chemical equilibrium with a minority phase of light-emitting excitons.
In **Chapter 3**, radiometric time-resolved photoluminescence measurements were performed on 3D hybrid perovskites. The thin films of $MAPbI_3$, $MAPbBr_3$ and the mixed-cation mixed-halide $MA_{1-x-y}FA_xCs_yPbI_{3-z}Br_z$ were fabricated through spin-coating deposition and, after annealing, coated with a protective poly(methyl methacrylate) (PMMA) layer. The optical characterization included absolute time-resolved photoluminescence, absorbance spectroscopy and quantum yield measured under pulsed excitation. Our results reveal that calculated radiative recombination constants are much lower than the ones estimated under the assumption of the only presence of excitons and free carriers, suggesting the existence of large polarons as the majority population of non-emitting (dark) excitations.

In **Chapter 4**, the charge transfer mechanism underlying a novel photocatalytic doping process in organic semiconductors is investigated. This doping method relies on reusable and air-stable photocatalysts with the only consumption of TSFI-based salts and the oxygen present in air. A combination of absorption spectroscopy, time-resolved photoluminescence and pump-probe transient absorption spectroscopy has been applied to the organic semiconductor and photocatalysts samples, revealing how the excited state of the

photocatalyst dominates the photoinduced electron transfer in the system. Furthermore, a set PL and TAS measurements have been performed during the reduction/oxidation cycle of the photocatalysts, indicating the presence of an initial intramolecular-charge-transfer excited state upon irradiation and the intriguing regeneration mechanism under air exposure. We consider this new doping mechanism as an opportunity to attract renewed scientific attention on organic semiconductors and also on their possible incorporation in perovskites, which can represent a new exciting system for optoelectronic devices.

The alloying of Sn-based perovskites with Pb is an interesting strategy that can halve the quantity of Pb in the active material, while overcoming some of the issues in working with pure Sn. In **Chapter 5**, we fabricated p-i-n solar cells using an active layer of composition $EACl_{0.015}Cs_{0.25}FA_{0.75}Sn_{0.5}Pb_{0.5}I_3$ and substituting to the most common hole-transport layer, PEDOT:PSS a solution-processed copper iodide layer. CuI is a transparent, highly conductive material with a widely available environment-friendly composition.
The power conversion efficiency of the top-performing device based on CuI was 20.1%, significantly higher than the 19.03% obtained by using PEDOT:PSS.
To carry out the comparison a wide set of thin film and device characterization techniques was employed. X-ray diffraction, scanning electron microscopy and atomic force microscopy were first utilized to assess the quality and the morphology of the CuI layer and the perovskite growth on top of it.
The fabricated devices, with a statistical size of 20 devices per architecture, were characterized under illumination and dark conditions, allowing the determination of the important photovoltaic parameters and their reproducibility. The device stability was monitored in N_2 storage and under thermal stress, with the former showing that the CuI device retaining 92.8% of its initial efficiency after 155 days. Further investigation on the thin films was done by steady-state and time-resolved photoluminescence that along the impedance spectroscopy on the devices showed a lower amount of traps present at the CuI/perovskite interface with respect to the PEDOT:PSS/perovskite one.

Samenvatting

De verwachting is dat de vraag naar energie de komende tijd gestaag zal blijven groeien. Zonne-energie heeft het potentieel om aanzienlijk bij te dragen aan het oplossen van dit probleem als een schone, overvloedige en hernieuwbare energiebron.
Hoewel conventionele zonnecellen een goed ontwikkeld productieproces hebben met een hoge energieomzetting efficiëntie, vereisen de hoogwaardige modules een kostbare fabricage die gepaard gaat met hoge temperaturen en een hoge zuiverheid van de uitgangshalfgeleider, die beide bijdragen aan de grote koolstofdioxide-voetafdruk van de technologie.
Wetenschappers spelen daarom een belangrijke rol in het innovatieproces binnen de energiestrategie, door nieuwe materialen en nieuwe concepten voor apparaten van de volgende generatie uit te vinden.
Op dit pad van onderzoek naar nieuwe halfgeleiders met eenvoudige verwerking, lage kosten en aantrekkelijke opto-elektronische eigenschappen gaf de ontdekking van hybride metaalhalogenide perovskieten aanleiding tot nieuw enthousiasme binnen het onderzoeksveld. Metaalhalogenide perovskieten bezitten een unieke reeks eigenschappen, van de hoge absorptiecoëfficiënt, de aanpasbare bandkloof en de hoge mobiliteit van ladingsdragers tot de lange diffusieafstand. Indrukwekkende prestaties in fotovoltaïsche toepassingen, lichtgevende diodes, lasers en fotodetectoren hebben het potentieel van deze in oplossing verwerkbare halfgeleiders voor toekomstige toepassingen aangetoond.
Ondanks deze uitstekende eigenschappen zijn er, aangezien onderzoek naar toegepaste metaalhalogenide perovskieten relatief recentelijk is begonnen, veel meer inspanningen nodig om perovskieten te promoten van laboratoriumschaal naar daadwerkelijke commercialisering. Tot de belangrijkste problemen die moeten worden aangepakt, behoren de aanwezigheid van lood en de algehele kwetsbaarheid van het materiaal, die wordt bepaald door de aard van de chemische bindingen. Bovendien is de efficiëntie van de energieomzetting, als we het hebben

over zonnepanelen met praktische afmetingen, nog ver verwijderd van hun theoretische limiet.
Om verdere vooruitgang te boeken in de richting van de technologische toepassing van metaalhalogenide perovskieten is meer werk nodig, variërend van de zoektocht naar milieuvriendelijkere materialen, de chemische en apparaattechniek tot een dieper begrip van hun fysische eigenschappen.
Dit proefschrift richt zich op het begrijpen van de fotofysica en opto-elektronische eigenschappen van organisch-anorganische metaalhalogenide perovskieten en hun toepassing in zonnecellen.

Een nauwkeurig onderzoek naar de fundamentele eigenschappen van metaalhalogenide perovskieten is essentieel in het proces van apparaatoptimalisatie.
In **Hoofdstuk 2** is de rol van excitonen, vrije ladingsdragers en polaronen in hybride metaalhalogenide perovskieten onderzocht met behulp van een ultrasnelle tandem-spectroscopietechniek. Deze techniek combineert, met succes, in de tijd opgeloste fotoluminescentie en differentiële transmissie spectroscopie. Deze twee technieken zijn complementair en bieden verschillende informatie over optische excitaties in het materiaal. In dit werk werden verschillende hybride perovskieten onderzocht, van 3D-composities die veel worden gebruikt in fotovoltaïsche cellen en lichtgevende diodes tot 2D-archetypen van Ruddlesden-Popper 2D-gelaagde halogenide perovskieten. In de analyse zijn de fotoluminescentie- en differentiële transmissietransiënten kwantitatief vergeleken, met dezelfde excitatieomstandigheden voor elk materiaal door middel van een correcte opstellingsconstructie. De verkregen resultaten duiden op de vorming van grote polaronen, dat wil zeggen, ladingsdragers gekoppeld aan vervormingen van het kristalrooster, in chemisch evenwicht met een minderheidsfase van lichtgevende excitonen.

In **Hoofdstuk 3** werden radiometrische, in de tijd opgeloste fotoluminescentiemetingen uitgevoerd op 3D hybride perovskieten.
De dunne films van $MAPbI_3$, $MAPbBr_3$ en het gemengde kation-gemengde halogenide $MA_{1-x-y}FA_xCs_yPbI_{3-z}Br_z$ werden geproduceerd door middel van spin-coating en, na verhitten, gecoat met een beschermende poly(methylmethacrylaat) (PMMA) laag. De optische karakterisering omvatte absolute, in de tijd opgeloste fotoluminescentie, absorptiespectroscopie en kwantumrendement metingen onder gepulseerde excitatie. Onze resultaten onthullen dat de berekende constanten van stralende recombinatie veel lager zijn

dan de constanten die zijn geschat onder de veronderstelling van de aanwezigheid van alleen excitonen en vrije dragers, wat duidt op het bestaan van grote polaronen als de meerderheidspopulatie van niet-emitterende (donkere) excitaties.

In **Hoofdstuk 4** wordt het ladingsoverdrachtsmechanisme onderzocht dat ten grondslag ligt aan een nieuw fotokatalytisch doteringsproces in organische halfgeleiders. Deze doteringsmethode is gebaseerd op herbruikbare en luchtstabiele fotokatalysatoren met alleen het verbruik van op TSFI-gebaseerde zouten en de aanwezige zuurstof in lucht. Een combinatie van absorptiespectroscopie, in de tijd opgeloste fotoluminescentie en in de tijd opgeloste absorptiespectroscopie is toegepast op de organische halfgeleiders en fotokatalysatoren, waardoor wordt onthuld hoe de aangeslagen toestand van de fotokatalysator de foto-geïnduceerde elektronenoverdracht in het systeem domineert. Bovendien zijn een reeks fotoluminescentie- en tijd opgeloste absorptiemetingen uitgevoerd tijdens de reductie-/oxidatiecyclus van de fotokatalysatoren, waarbij de aanwezigheid van een initiële intramoleculaire ladingsoverdracht-geëxciteerde toestand bij bestraling en het intrigerende regeneratiemechanisme onder blootstelling aan lucht werden ondervonden. We beschouwen dit nieuwe doteringsmechanisme als een kans om hernieuwde wetenschappelijke aandacht te vestigen op organische halfgeleiders en ook op hun mogelijke integratie in perovskieten, wat een nieuw, opwindend systeem voor opto-elektronische apparaten kan opleveren.

Het legeren van op tin gebaseerde perovskieten met lood is een interessante strategie die de hoeveelheid lood in het actieve materiaal kan halveren en tegelijkertijd een aantal problemen bij het werken met puur tin kan overwinnen. In **Hoofdstuk 5** hebben we p-i-n-zonnecellen gefabriceerd met een actieve laag van de compositie $EACl_{0.015}Cs_{0.25}FA_{0.75}Sn_{0.5}Pb_{0.5}I_3$ en is de meest voorkomende gatentransportlaag, PEDOT:PSS, vervangen door een in oplossing verwerkte koperjodide (CuI) laag. CuI is een transparant, goed geleidend materiaal, niet schaars en milieuvriendelijk.
De energieomzetting efficiëntie van het best presterende apparaat op basis van CuI was 20,1%, aanzienlijk hoger dan de 19,03% die werd verkregen door PEDOT:PSS te gebruiken.
Om de vergelijking tussen de verschillende gatentransportlagen uit te voeren werd een breed scala aan dunne film- en apparaat karakterisatie technieken gebruikt. Röntgendiffractie, elektronenmicroscopie en atoomkrachtmicroscopie werden eerst

gebruikt om de kwaliteit en de morfologie van de CuI-laag en de groei van de perovskiet daarbovenop te beoordelen.
De gefabriceerde apparaten, met een statistische grootte van 20 apparaten per architectuur, werden gekarakteriseerd onder verlichte en donkere omstandigheden, waardoor de bepaling van de belangrijke fotovoltaïsche parameters en hun reproduceerbaarheid mogelijk was. De stabiliteit van het apparaat werd gecontroleerd wanneer het in stikstof omgeving was opgeslagen en onder thermische stress, waarbij onder de eerstgenoemde conditie bleek dat het CuI-apparaat 92,8% van zijn oorspronkelijke efficiëntie behield na 155 dagen. De dunne films werden verder onderzocht door middel van fotoluminescentiemetingen met continue golven en door middel van in de tijd opgeloste fotoluminescentie, die samen met impedantiespectroscopie op de apparaten een lagere hoeveelheid defecten aantoonden op het CuI/perovskiet-grensvlak ten opzichte van het PEDOT:PSS/perovskiet-grensvlak.

Translated by Larissa van de Ven

Curriculum vitae

Education

2019 – 2024	Ph.D. Candidate in Physics Photophysics and Optoelectronics group Zernike Institute for Advanced Materials University of Groningen, The Netherlands Photonics and Optoelectronics group Physics Department University of Cagliari, Italy
2016 – 2019	M.Sc. Physics *(cum laude)* University of Cagliari, Italy
2012 – 2016	B.Sc. Physics University of Cagliari, Italy

Conferences

2023 NWO Physics – Dutch Research Council Conference on Physics, Veldhoven, The Netherlands. "Effect of active material composition on electroluminescence in mixed tin-lead metal halide perovskite solar cells" *Poster*.

2022 nanoGe International Conference on Hybrid and Organic Photovoltaics, Valencia, Spain, "Tin-lead-metal halide perovskite solar cells with enhanced crystallinity and efficiency by addition of fluorinated long organic cation" *Poster*.

2022 ISOPHOS International School on Hybrid and Organic Photovoltaics, Talamone, Italy. *Attendance.*

2021 IME – Innovative Materials for Energy, Online event. *Attendance.*

2021 nanoGe School on Fundamentals of Emerging Solar Cells, Online event. *Attendance.*

2020 CLEO - Conference on Lasers and Electro-Optics, Online event. *Attendance*

2020 IME – Innovative Materials for Energy, Online event. *Attendance.*

Publications

1. **R. Pau**, M. Pitaro, L. Di Mario, Q. Feng, M. Saba, M.A.Loi, *Manuscript in preparation*

2. W. Jin, C,Y. Yang, **R. Pau**, Q. Wang, E.K. Tekelenburg, H.Y. Wu, Z.Wu, F. Pitzalis, T. Liu, Q. He, Q. Li, R. Kroon, M.J. Heeney, H Y. Woo, A. Mura, M. Fahlman, M.A. Loi, S. Fabiano, "Photocatalytic doping of organic semiconductors", *Submitted*

3. A. Simbula, L. Wu; F. Pitzalis, **R. Pau**, S. Lai, F. Liu, S. Matta, D. Marongiu, F. Quochi, M. Saba, A. Mura, G. Bongiovanni, "Exciton dissociation in 2D layered metal-halide perovskites" *Nature Communications* 14, 4125, 2023

4. L. Romani, A. Speltini, R. Chiara, M. Morana, C. Coccia, C. Tedesco, V. Armenise, S. Colella, A. Milella, A. Listorti, A. Profumo, F. Ambrosio, E. Mosconi, **R. Pau**, F. Pitzalis, A. Simbula, D. Ricciarelli, M. Saba, M. Medina-Llamas, F. De Angelis, L. Malavasi, "Air- and water-stable and photocatalytically active germanium-based 2D perovskites by organic spacer engineering", *Cell Reports Physical Science* 4, 101214, 2023

5. M. Pitaro, **R. Pau**, H. Duim, M. Mertens, W. T. M. Van Gompel, G. Portale, L. Lutsen, M. A. Loi, "Tin-lead-metal halide perovskite solar cells with enhanced crystallinity and efficiency

by addition of fluorinated long organic cation", *Applied Physics Reviews* 9, 021407, 2022

6. F. Liu, A. Simbula, S. Lai, L. Wu, Q. Wang, D. Marongiu, **R. Pau**, S. Matta, F. Pitzalis, A. G. Lehmann, K. Wang, A. Filippetti, F. Quochi, M. Saba, A. Mura, G. Bongiovanni, "White light emission with unity efficiency from $Cs_2Na_{1-x}Ag_xIn_{1-y}Bi_yCl_6$ double perovskites: the role of bismuth and silver*", Journal of Materials Chemistry C,* 10, 14232-14241, 2022

7. A. Simbula, **R. Pau**, F. Liu, L. Wu, S. Lai, A. Geddo-Lehmann, A. Filippetti, M. A. Loi, D. Marongiu, F. Quochi, M. Saba, A. Mura, G. Bongiovanni, "Direct measurement of radiative decay rates in metal halide perovskites", *Energy Environmental Science*, 15, 1211-1221, 2022

8. A. Simbula, **R. Pau**, Q. Wang, F. Liu, V. Sarritzu, S. Lai, M. Lodde, F. Mattana, G. Mula, A. G. Lehmann, I. D. Spanopoulos, M. G. Kanatzidis, D. Marongiu, F. Quochi, M. Saba, A. Mura, G. Bongiovanni, "Polaron Plasma in Equilibrium with Bright Excitons in 2D and 3D Hybrid Perovskites", *Advanced Optical Materials*, 9, 2100295, 2021

9. F. Liu, D. Marongiu, **R. Pau**, V. Sarritzu, Q. Wang, S. Lai, A. G. Lehmann, F. Quochi, M. Saba, A. Mura, G. Bongiovanni, A. Mattoni, C. Caddeo, A. Bosin, A. Filippetti, "Ag/In lead-free double perovskites", *EcoMat*, 2:e12017, 2020

10. D. Marongiu, X. Chang, V. Sarritzu, N. Sestu, **R. Pau**, A. Geddo Lehmann, A. Mattoni, F. Quochi, M. Saba, A. Mura, G. Bongiovanni, "Self-Assembled Lead Halide Perovskite Nanocrystals in a Perovskite Matrix" ACS Energy Lett. 2017, 2, 4, 769–775, 2017

Acknowledgments

Embarking on the PhD journey is a very personal experience, in which I received great support, advice and encouragement from many people, academically and personally. I want to express my gratitude to the people who, in one way or another, helped me along the way.

First and foremost, I want to express my gratitude to my supervisors, Prof. Michele Saba and Prof. Maria A. Loi. It's not usual to have two main supervisors, and even less to have such dedicated and encouraging professors. Without your guidance and mentorship, this thesis would not have been possible.

Michele, at the start of my academic journey at the physics department, back in 2012, you were the professor of the experimental physics course (one of my favorites!). Thank you for the countless advices and your trust in me at every step of my academic path, as a bachelor, master and PhD student. You are always available to listen and discuss problems in the lab, in data analysis, and also in life. I truly learned so much from you.

Maria, I still remember when you proposed to me the double PhD with the University of Groningen. You warned me that it would have been a challenging path, and it was indeed. You welcomed me into a diverse, prepared, and stimulating group, that with time became a second family. Thank you so much for giving me this opportunity to grow, as a scientist and as a person. Your knowledge and your commitment to science are a true inspiration for me.

I am deeply thankful to the assessment committee members: Prof. Luciano Colombo, Prof. Maxim S. Pchenitchnikov, Prof. Guglielmo Lanzani, and Prof. Bruno Ehrler for reading and critically evaluating this thesis.

I owe a special thanks to Dr. Simbula. Angelica, you immensely supported me since you joined the group and I'm always glad to spend

time with you in the lab, trying to solve lab problems, discussing spectroscopy, but also about food and cats! Thank you so much for your help, my thesis would not have been possible without your immense work and dedication.

To my colleagues at Unica, Federico, Stefano, Selene, Silvia, Fang, Emanuele, Rui Rui and Luyan: I am very grateful for your help and all the good time spent together during my project in Cagliari. I wish you all the best for your career.

Special thanks to Prof. Daniela Marongiu, Prof. Andrea Mura, Prof. Francesco Quochi, Prof. Giovanni Bongiovanni, Dr. Valeria Demontis for all the precious support given during my time in the Fotonica group in Cagliari.

A word of thanks to the PhD school coordination, Prof. Paolo Ruggerone, Prof. Umberto D'Alesio and Prof. Attilio Vargiu, and to my year-end seminars committee, Prof. Biagio Saitta and Dr. Andrea Sanna. Additionally, I would like to acknowledge all the technical and administrative staff at Unica and at the Department of Physics.

Groningen will always be a special city for me, and this is also because of the wonderful people that I met there.
David, Jacopo and Jiale, even if my PhD journey was already 1 year old, we kind of all started together there. It's because of you guys that my beginning in Groningen and inside the group was so smooth and it was a pleasure to work along with you! I'm bringing back with me tons of memories of the time spent together! Jacopo, with a Sardinian around I was feeling at home, thanks for all the pieces of advice as a Groningen expert and for all the fun we had around! JC, I'm so grateful for the endless discussions about food culture and Chinese and Cantonese cultures, xiè xiè!

David, you are a special person and I'm so grateful that our paths crossed. Whether I was dealing with scientific doubts, lab issues or life difficulties, you've always had my back and I will never forget it.
As a colleague, an awesome friend, and also a gym bro, you made my time in Groningen a memorable experience! Thanks for accepting to be my paranymph!
Ainoa, a big shoutout to you for the wonderful cover you made for this thesis, your work exceeded my most optimistic expectations. And last

but not least, thanks to both of you for letting me take care of Moritz and Turia!

Dear Paul, even if you joined later the group, you quickly became a close friend. I thoroughly enjoyed our frequent conversations, as a critical colleague and as an honest, true friend. I was very happy to share the office with you, even if for such a short time. Thank you for all the support, for all the amazing road trips with the *demon* and for embracing my football passion! I'm delighted that you accepted to be one of my paranymphs.

Lorenzo, thank you so much for being such a great colleague and friend. You were able to see from my face how my experiments were going, and even with your busy schedule, you always had time to help me in the lab, cheer me up, or discuss how to plan the next experiment. Many thanks to you and Martha for all the amazing dinners and for letting me take care of Pardulin… Femto! All the best to you!

To my office mates, thank you so much! Dear Matteo, you've been a great daily supervisor and I'm grateful you had the patience to train me in the art of solar cell fabrication. Thanks for all the nice conversations and your constant support in and outside the lab! Karolina, I will miss our conversations in the office, regardless of the topic. You were a great office mate and an amazing colleague! Feng, we shared the office only for a short time, but I'm glad I've been your daily supervisor and I wish you all the best for your future.

To all the group members, past and present, Lijun, Larissa, Federico, Filippo, Eelco, Francesco, Suleyman, Tim, Moti, Han, Jiaxiong, Sander, Fransien, Jun, Herman, Xuwen, Unnati: thank you for your support and all the pleasant conversations and my best wishes for your careers!

Our technicians deserve huge thanks for their constant technical support. Teo and Arjen, you are the heart of the group and I will miss such an essential help in my future research! Thanks to both of you for organizing the fish Friday as well and to Teo for helping me organize the POE football games!

Thanks to the Cicci Research team: Lucio, Bas, Roberto, Alessandro, Edda and Francesco, I will not forget your warm hospitality and your support during my stay in Grosseto.

This PhD project would not have been possible without the financial support of the Italian Government through PON Ricerca e Innovazione under Ministero dell'Istruzione, dell'Università e della Ricerca, the University of Groningen, and the Faculty of Science and Engineering.

Last but not least, special thanks to my family and my friends.

Sprigghi, even if you can't read, thank you for saving me from loneliness. Thanks for waiting for me in front of my door, regardless of the weather and how late it was. Thanks for all the funny moments and your comforting presence. I already miss you.

Un grazie ai miei cari amici, con cui ho passato innumerevoli serate, di persona e online. Avete reso questi anni più facili e spero che la nostra amicizia duri ancora a lungo nel tempo.

Alla mia famiglia e al loro supporto incondizionato, nei successi e nei fallimenti di questo percorso: grazie di cuore. Ma & Pa, grazie per esserci sempre stati e per avermi dato quest'opportunità di formarmi e di percorrere questa strada, spesso tortuosa, senza mai pressioni. Grazie Fede per essere il miglior fratello che potessi avere e per il tuo contagioso ottimismo nella vita.

Infine, alla mia fonte di ispirazione, conforto e sostegno, Alessia. Non avrei avuto nulla di tutto questo senza di te e sono profondamente grato che tu sia entrata nella mia vita. In questi anni mi hai sempre incoraggiato ad essere la versione migliore di me stesso e a superare le sfide che mi sono comparse davanti. Sei riuscita a starmi vicino anche a migliaia di chilometri di distanza e sei stata la voce razionale nei momenti peggiori. Sono sicuro che il futuro ci riserva tante avventure e sfide e non vedo l'ora di affrontarle, insieme.

Grazie, Bedankt, Thank you.

Riccardo

La borsa di dottorato è stata cofinanziata con risorse del
Programma Operativo Nazionale Ricerca e Innovazione 2014-2020 (CCI 2014IT16M2OP005),
Fondo Sociale Europeo, Azione I.1 "Dottorati Innovativi con caratterizzazione Industriale"

UNIONE EUROPEA
Fondo Sociale Europeo